Experimental and Theoretical Analysis of the Cyclic Water Gas Shift Reactor

Dissertation

zur Erlangung des akademischen Grades

Doktoringenieur
(Dr. - Ing.)

von Dipl.-Ing. Christoph Hertel
geb. am 26. August 1981 in Leipzig

genehmigt durch die Fakultät für Verfahrens- und Systemtechnik
der Otto-von Guericke-Universität Magdeburg

Promotionskommission: Prof. Dr. rer. nat. habil. Helmut Weiß (Vorsitz)
Prof. Dr.-Ing. habil. Kai Sundmacher (Gutachter)
Assoc. Prof. Dr. techn. Viktor Hacker (Gutachter)
Apl. Prof. Dr.-Ing. habil. Michael Mangold (Gutachter)

Eingereicht am 13. 1. 2015
Promotionskolloquium am 30. 6. 2015

Abstract

The Cyclic Water Gas Shift Reactor (CWGSR) is a periodically operated fixed bed reactor based on the steam iron process. Carbon monoxide free hydrogen can be produced from a feed stock of syngas and steam. An oxygen storing fixed bed of iron oxide enables the CWGSR to operate as gas converter and separator at the same time.

The objectives of this work were to contribute to the development of the CWGSR through (a) the measurement and modelling of gas-solid reaction kinetics, (b) the experimental analysis of a CWGSR test plant and (c) the formulation of a reactor model that incorporates all these findings.

The reaction kinetics were measured on $400\,\mu m$ particles of stabilised iron oxide material via thermogravimetric analysis (TGA) in a $CO/CO_2/N_2$ and H_2/N_2 atmosphere of varying composition and temperature. A number of gas-solid reaction models from the literature were compared and rate expression formulated taking the thermodynamic equilibrium conditions of the investigated system into account. Two models, the Avrami Model (JMAK) and the Uniform Conversion Model (UCM), were fitted to the experimental data with similar accuracy.

A test stand was constructed for the experimental studies on the CWGSR. A reactor of 1 m length was operated at $750\,°C$ in flow reversal and forward flow mode. The concentrations of CO, CO_2 and H_2 at the reactor outlet were measured over time.

The formation and movement of two distinct reaction fronts could be observed, confirming the assumption of a previously published shortcut model of the CWGSR [46]. Predicted advantages of the flow reversal operating mode [47] could not be confirmed experimentally. This was attributed to experimental challenges like fixed bed material degradation in the final timeframe of this experimental study.

A dynamic, isothermal, 1-dimensional reactor model, based on the mass balances for the gas and solid phases was formulated. With the application of the a priori determined reaction rates, the model could be fitted to previously aquired experimental results. Two additional parameters were required to account for iron oxide material changes during the preparation of the fixed bed. The fitted model could successfully reproduce the experimental results of a complete CWGSR operating cycle.

The validated model of this work confirmed the prediction of different operating regimes by a previously published model [46]. These operating regimes of the CWGSR are characterized by substantially different performance parameters and are key to the future development of the CWGSR.

Zusammenfassung

Der Zyklische Wassergas Shift Reaktor (ZWGSR, Engl.: CWGSR) ist ein periodisch betriebener, auf dem Dampf-Eisen-Prozess basierender Festbettreaktor. Er ermöglicht die intermittierende Produktion von kohlenmonoxidfreiem Wasserstoff aus Synthesegas und Wasserdampf in einem Reaktor. Diese Kombination von Reaktion und Stofftrennung wird durch ein sauerstoffspeicherndes Festbett aus Eisenoxid ermöglicht.

Die Ziele dieser Arbeit waren (a) die Vermessung und Modellierung der Gas-Feststoff-Reaktionskinetiken, (b) die experimentelle Analyse einer ZWGSR Technikumsanlage und (c) das Aufstellen eines Reaktormodells, welches die vorhergehenden Ergebnisse abbildet.

Die Reaktionskinetiken wurden mittels thermogravimetrischer Analyse in $CO/CO_2/N_2$ und H_2/N_2 Atmosphäre vermessen und die Abhängigkeit gegenüber Gaszusammensetzug und Temperatur bestimmt. Aus der Literatur wurden die Modelle nach Avrami (JMAK) und das Uniform Conversion Model (UCM) ausgewählt und unter Berücksichtigung der chemischen Gleichgewichte des vorliegende Stoffsystem ausformuliert. Beide Modelle bilden die experimentellen Ergebnisse in guter und gleicher Qualität ab.

Ein ZWGSR-Teststand im Technikumsmaßstab wurde errichtet. Dieser ermöglichte den periodischen Gegenstrombetrieb eines 1 m Rohrreaktors bei 750 °C unter Vermessung der Abgaszusammensetzung.

Die Bildung und Wanderung zweier gleichzeitig auftretender Reaktionsfronten konnte nachgewiesen werden. Dies bestätigt ein früheres ZWGSR-Modell [46]. Vorhergesagte Vorteile des Gegenstrombetriebes [47] konnten am Versuchsstand nicht bestätigt werden. Als Grund wurden experimentelle Probleme ausgemacht.

Basierend auf Massenbilanzen der Gasphase und des Festbetts wurde eine dynamisches, isothermes, eindimensionales Reaktormodell aufgestellt. Die zuvor dediziert gemessenen Reaktionskinetiken wurde mittels zweier zusätzlicher Parameter auf das nun pelletierte Festbettmaterial angepasst. Die Messungen des Versuchsstandes konnten mit Hilfe des Modells abgebildet werden.

Das so validierte Modell konnte die in der Literatur theoretisch vorhergesagten Betriebsregime des ZWGSR [46] bestätigen. Diese sind u. a. durch deutlich unterschiedliche Leistungsparameter gekennzeichnet und ein wichtiger Baustein für die zukünftige Optimierung des Reaktors.

Contents

Contents

List of symbols

Symbol		Unit
c_p	specific heat capacity	$\mathrm{J\,mol^{-1}\,K^{-1}}$
d_{50}	average particle diameter of granular material	m
d	diameter of reaction	m
D	diffusion coefficient	$\mathrm{m^2\,s^{-1}}$
E	activation energy	$\mathrm{J\,mol^{-1}}$
F	volumetric flow rate	$\mathrm{m^3\,s^{-1}}$
k	reaction constant, frequency factor	$\mathrm{mol_j\,g_{weigh\,in}^{-1}\,s^{-1}}$
L	length of reactor	m
m	mass	g
n	molar amount	mol
r	reaction rate	$\mathrm{mol_j\,g_{weigh\,in}^{-1}\,s^{-1}}$
R	ideal gas constant	$\mathrm{J\,mol^{-1}\,K^{-1}}$
P	coordinate along the radius of a pellet	m
t	time	s
T	temperature	K
x	molar fraction	-
X	vector of optimisation parameters	
y	ratio of H_2O/H_2, or CO_2/CO, see Eq. 2.3	-
Y	carbon/hydrogen content of gas, see Eq. 2.4	-
z	coordinate along the reactor (0, L)	m
$\Delta_r g^{\ominus}$	standard Gibbs free energy of reaction	$\mathrm{J\,mol^{-1}}$
$\Delta_f h^{\ominus}$	standard enthalpy of formation	$\mathrm{J\,mol^{-1}}$
$\Delta_f s^{\ominus}$	standard entropy of formation	$\mathrm{J\,mol^{-1}\,K^{-1}}$
ε	void fraction	-
v_{ij}	stoichiometric factor of species i in reaction j	$\mathrm{mol_i\,mol_j^{-1}}$
ρ	density	$\mathrm{g\,m^{-3}}$
τ	characteristic time constant/duration	s
ω	speed of reaction zones	$\mathrm{m\,s^{-1}}$

Indices

Symbol	
disp	dispersion
equ	chemical equilibrium
Fe, t	total amount of iron atoms, see Eq. (3.3)
i	chemical species
j	reaction
O	oxygen atom
res	mean residence time
t	total
TGA	setting of the TGA apparatus
0	inital, initial mass
$\pm$	forward (oxidation/"+") and/or backwards (reduction/"–") reaction

Superscripts

Symbol	
$\ominus$	at 273.15 K, 101 315 Pa, also conditions for Normlitre [NL]
$\otimes$	at 1023.15 K, 101 315 Pa
equ	chemical equilibrium
$feed$	feed conditions
g	gas phase
m	reaction rate/driving force exponent of gas phase
n	reaction rate/driving force exponent of solid phase
R	reaction zone/front
s	solid phase

1. Introduction

Hydrogen gas plays an important part in the chemical and energy industry. It has a wide variety of applications and motivated the development of a large number of processes to produce it. The reactor concept which is the focus of this work is no exception and promises an effective way of producing clean hydrogen. As to what *clean* means, is part of in this introductory chapter.

Starting point is an overview on the application, production and purification of hydrogen. In this context, the Cyclic Water Gas Shift Reactor (CWGSR) is described.

A short excursion on the historical development of the reactor's predecessors in the early 20th century is followed by a review of the recent developments in the field. A comparison to similar reactor concepts outside the realm of hydrogen production closes this section.

A list of objectives of this present work conclude the introduction and outline the following chapters.

1.1. Hydrogen

1.1.1. Application

About half of the total world wide hydrogen (H_2) production is used in the production of ammonia via the Haber Bosch process [51, 71]. Ammonia itself is the feedstock for industrial nitrogen fertilisers and plays a significant role in the world's food production since the early 20th century. Ammonia is also the direct or indirect source of every nitrogen atom in industrially produced chemical compounds today [4]. The second largest consumer of the current hydrogen production are oil refineries [72]. Hydrogen is used for desulfurisation and cracking, helping to provide fuels for the transportation sector and feedstocks for the petrochemical sector.

The use of hydrogen as an energy carrier is not significant at the moment but expected to sharply rise in the future [38, 80, 111]. H_2 is considered a "clean" fuel, producing only H_2O

at the point of energy release (e. g. car engine) and no carbon containing pollutants (CO, CO_2, volatile organic compounds (VOC), soot, etc.). H_2 is also a versatile fuel, e. g. able to be used in internal combustion engines and electrochemical fuel cells.

The public's view of hydrogen, however, is a different one [20, 87]. It is most often associated with the transport sector and the fuel cell powered car, a focus of research and marketing but not yet production by major automobile manufacturers. Still in the public mind are also the hazards publicised by one of the first modern day disasters recorded on film, the fire accident of the airship Hindenburg in 1937. The importance of hydrogen for today's daily life via food, petrochemical products and (fossil) fuels is rarely known.

1.1.2. Production

H_2 can be produced from many different sources, being one of the most abundant elements in the earth's upper crust, specifically lithosphere and hydrosphere. For the sake of an easier later classification of the CWGSR process, H_2 production processes are divided into two categories based on their feedstocks: hydrocarbons and water.[1] As a rule, hydrocarbons bring most or all of the energy of the product H_2 into the process in form of their chemical energy and produce a mixture of H_2 and carbon oxides. Whereas processes based on water need another source of energy which will be converted into the chemical energy of H_2. In that case, there is no need to remove carbon oxides from the product gas.

This coarse classification is no indicator of the "eco-friendliness" in the sense of a sustainable use of energy or carbon neutrality towards the earth's atmosphere. Hydrocarbon feedstocks can be either from fossil (oil, gas) or renewable (biomass, biogas) sources. Likewise, the energy used for the production of H_2 from water can be from fossil (coal based power plant) or renewable sources (wind energy, photovoltaics).

The following paragraphs give a broad overview over the H_2 production and purification techniques.

Hydrocarbon Feedstocks

Steam Methane Reforming (SMR) is the predominant process for H_2 production in industry today [50, 71, 90]. Other hydrocarbons (naphta, gasoline, jet fuel, methanol, etc.) can be reformed with steam too, but show more problems with catalyst deactivation by sulphur and

---

[1]Hydrogen production from other feedstocks, like ammonia or hydrogen sulfide, are consciously left out of this discussion. Although a topic in research, they are not used for H_2 production on a significant scale.

coking [36]. Steam reforming consists generally of two main reactions: hydrocarbon splitting (Equ. 1.1) and the water gas shift reaction (Equ. 1.2).

$$C_nH_m + n\,H_2O \rightarrow n\,CO + \left(n + \frac{m}{2}\right)H_2 \qquad n = 1,\ \Delta_r h^{\ominus} = 206\,\text{kJ/mol} \tag{1.1}$$

$$CO + H_2O \rightarrow CO_2 + H_2 \qquad \Delta_r h^{\ominus} = -41.2\,\text{kJ/mol} \tag{1.2}$$

Steam reforming is very energy intensive due to the amount of superheated steam necessary. A less demanding process in terms of energy consumption and desulfurisation is Partial Oxidation (1.3) [50, 108]. This again is suitable for methane and liquid hydrocarbons. The reaction is much faster than steam reforming and it is exothermic. On the downside for H_2 production, the H_2/CO ratio is lower than with SMR.

$$C_nH_m + {}^{1\!/\!2}n\,O_2 \rightarrow n\,CO + {}^{1\!/\!2}m\,H_2 \qquad \Delta_r h^{\ominus} < 0\,\text{kJ/mol} \tag{1.3}$$

Autothermal Reforming seeks to combine the advantages of steam reforming (high H_2 yield) and partial oxidation (not endothermic, simple reactor). Heat is supplied inside the reactor through combustion. The main disadvantage is the need for an oxygen plant, as pure O_2 is most often used as an oxidant to avoid the addition of N_2 through the use of air [55].

Gasification is a versatile process to produce H_2 from any solid (hydro)carbon feedstock such as coal, biomass, municipal waste [49, 62]. The solid is brought in contact with steam or air at high temperatures which initiates a complex reaction network of pyrolysis, cracking, partial oxidation, steam reforming, water gas shift and others. To maximise heat and mass transfer, gasification plants usually employ fluidised bed reactors. Due to the gasification's intrinsic handling capabilities of solids, the coupling of this technology with CO_2 capture in chemical looping reactors is of high interest. It is also discussed in Sec. 1.2.3.

There is a wide range of other, not commercially applied ways to produce H_2 from hydrocarbons. Excellent overviews and reviews can be found in the literature (e. g. [36, 50, 71]). Two emerging technologies will be mentioned: One is Plasma Reforming [11, 75], where the energy and radicals needed for reforming is introduced by a plasma arc, typically generated by electricity. Advantages include fast start-up, little or no catalysts, sulphur tolerance, small size and low weight. Another interesting technology is Aqueous Phase Reforming [16, 17, 74]. The reforming is done in the liquid phase at high pressures and moderate to high temperatures with heterogeneous catalysts. The advantages include the eliminated need to vapourise water

and the ability to process feedstocks, which cannot be vaporised without first degrading them, e. g. glucose.

Generally, H_2 produced from hydrocarbons contains an oxide of carbon. There are, however, some exceptions to the rule: E. g. Methane Decomposition (Equ. 1.4) [1,68] and Methane Dehydro-Aromatisation (Equ. 1.5) [88, 106]. These two processes are slightly endothermic and produce H_2 as the only gaseous compound, albeit at a lower yield of H_2 per carbon atom than other processes. The co-products of methane dehydroaromatisation are benzene and naphthalene. By virtue of their value in comparison with methane, they are the main motivation for the research in this area.
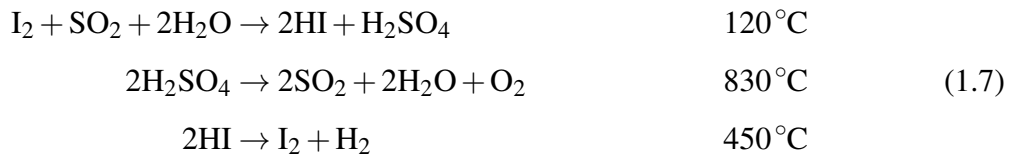
$$CH_4 \rightarrow C + 2\,H_2 \qquad\qquad \Delta_r h^{\ominus} = 90\,kJ/mol \qquad (1.4)$$

$$6\,CH_4 \rightarrow C_6H_6 + 9\,H_2 \qquad\qquad \Delta_r h^{\ominus} = 88\,kJ/mol \qquad (1.5)$$

Water as Feedstock

The splitting of water can be divided into three categories: electrolysis, thermolysis and photoelectrolysis – depending on the source of energy used to split one of the most abundant chemical compounds on earth in its constituents.

Electrolysers are commercially used for the production of hydrogen since the 1890s and essentially convert electrical energy into chemical energy in the form of hydrogen and oxygen. There are many different types available differing in operating temperature, materials and efficiencies – similar to fuel cells. The three most prominent types are alkaline electrolysers (most developed, lowest capital cost, lowest efficiency) [91], polymer electrolyte membrane (PEM) electrolysers (higher efficiency, higher cost, smallest size) [89] and solid oxide electrolysis cells (highest electrical efficiency, least developed) [110]. One advantage of electrolysers is the ability to operate them under elevated pressure. The generated pressurised H_2 is otherwise costly to produce, while pressurising water is relatively cheap. The reaction scheme of a PEM electrolyser is given as an example for this technology in Equ. 1.6. The protons travel from the anode to the cathode through the membrane, the electrons through the electrical circuit.

$$2\,H_2O \rightarrow O_2 + 4\,H^+ + 4\,e^- \qquad\qquad (Anode)$$

$$4\,H^+ + 4\,e^- \rightarrow 2\,H_2 \qquad\qquad (Cathode) \qquad (1.6)$$

In the classical, single-step thermochemical water splitting or thermolyis, water is heated high enough for the chemical equilibrium to shift sufficiently away from water and towards hydrogen and oxygen. Ideally, temperatures around $2500\,°C$ are targetet [70]. Such high grade heat is problematic in terms of materials and process efficiencies and led to the development of thermochemical water splitting cycles. They operate at lower temperatures and elevated pressures with often corrosive chemicals, as e. g. the sulphur-iodine cycle (Equ. 1.7). This technology is not commercially viable at the moment. Interest for thermochemical cycles came traditionally from the nuclear energy community [12, 70]. Recently, developments in utilizing concentrated solar radiation, e.g. through heliostats,drive this research [83]. Solar furnaces also increased the number of technically viably cycles, as higher temperatures can be safely achieved in comparison to nuclear power [82].

$$I_2 + SO_2 + 2H_2O \rightarrow 2HI + H_2SO_4 \qquad\qquad 120\,°C$$
$$2H_2SO_4 \rightarrow 2SO_2 + 2H_2O + O_2 \qquad\qquad 830\,°C \qquad (1.7)$$
$$2HI \rightarrow I_2 + H_2 \qquad\qquad 450\,°C$$

Photoelectrolysis [35] uses the energy of photons or sunlight to decompose water [9,52,54]. Similar to photovoltaics, pairings of doped semiconductor materials are used to generate an electric field and an electron where a photon strikes the anode. Instead of driving an external load, water is split in the electrolyte the cell is suspended in.

Purification

As carbon monoxide (CO) deactiviates a wide range of catalysts applied for example in ammonia production or low temperature fuel cells, it has to be removed from the hydrogen gas before further use.

The Water Gas Shift (WGS) reaction is the classic industrial process to reduce the amount of CO and increase the amount of H_2 in the gas mixture, see Equ. 1.2. The process is typically split into two reactors: The main part of the conversion is achieved in a High Temperature Shift (HTS) reactor ($\approx 350\,°C$), which promotes a fast conversion but is limited by the chemical equilibrium. It is followed by a Low Temperature Shift (LTS) reactor ($\approx 200\,°C$) to reduce the CO content to below $1\,\%$. In this process, H_2 is not separated from the source gas. The emphasis is on the reduction of the CO content in the gas mixture.

Pressure Swing Adsorption (PSA) is an established technology in modern H_2 production plants. The H_2 is separated to high purities (typically 99.9 % or higher) from other source gas constituents. The process is based on the varying affinities of different gases to adsorb on solid surfaces, rather than on chemical reactions. Energy for the operation of gas compressors is required.

Preferential Oxidation (PrOx) seeks to remove CO from a H_2-rich gas mixture by catalytic oxidation with oxygen. The catalyst's selectivity is based on the same properties that cause CO to usually "poison" catalysts: its good adsorptivity. Depending on the amount of oxygen added and the quality of heat removal, H_2 is lost in this process, too. PrOx is relatively prominent in industry as it is a low cost method for reducing CO content to desired levels.

Membrane reactors that separate generated H_2 are under development. Thin layers of metal, e. g. palladium, are used. These can withstand reasonably high process temperatures. With the integration in WGS reactors or reformers, thermodynamic constraints can be overcome by in-situ removal of the reaction product H_2.

The Steam Iron Process (SIP) is an old process concept (see Sec. 1.2.1) that regained interest in the last two decades. In this process CO as well as H_2 are consumed in the first of two reaction steps to reduce iron oxide to iron (Equ. 1.8). In the second step, steam is brought into contact with the reduced iron to produce H_2(Equ. 1.9). Thereby iron oxides are formed. These iron oxides can then be recycled in the first step. The net reaction is the WGS (Equ. 1.10). Note that for simplicity, only FeO is mentioned in this example; More details on the oxides of iron are found in Sec. 2.3. The SIP can be regarded as a WGS reactor with iron as an oxygen storage material that mediates between gas oxidation and reduction. The SIP integrates WGS reactor and a gas separator. The SIP can also be classified as a chemical looping reactor and is most often implemented with two fluidised beds that exchange the solid.

$$CO/H_2 + FeO \rightarrow CO_2/H_2O + Fe \qquad (1.8)$$

$$H_2O + Fe \rightarrow H_2 + FeO \qquad (1.9)$$

$$CO + H_2O \rightarrow H_2 + CO_2 \qquad (1.10)$$

1.2. Cyclic Water Gas Shift Reactor (CWGSR)

The Cyclic Water Gas Shift Reactor (CWGSR) is an implementation of the steam iron process (SIP). It is therefore used to generate high purity H_2 from syngas, which is in turn obtained
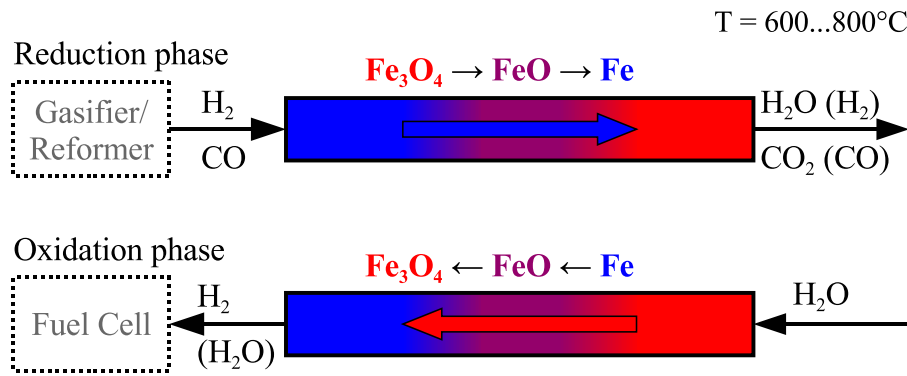
Figure 1.1.: Operating principle of the Cyclic Water Gas Shift Reactor (CWGSR), illustrated here in the flow reversal mode.

from hydrocarbon feedstocks. The oxygen storage is realised in a *fixed bed* consisting of iron oxide. The two operating phases (Equs. 1.8 and 1.9) which form one operating cycle are illustrated in Fig. 1.1. During the reduction phase, a fuel gas containing carbon monoxide and hydrogen is used to reduce iron oxides to iron. This fuel gas may originate from a reforming process or a gasification unit. The gaseous product during this phase is oxidised to a high extent, but it still contains significant fractions of combustible species. It may be used to produce heat in a combustion unit. As soon as the fixed bed has been reduced to a sufficient extent, the feed gas is switched to steam. During the following oxidation phase, the steam is used to oxidise the fixed bed back to iron oxide. The gaseous product is a mixture of hydrogen and steam, which is free of carbon monoxide and other undesired species. The product gas can be utilised in low temperature fuel cells or in chemical processes.

As illustrated in Fig. 1.1, the iron oxides formed in the CWGSR at temperatures above $574\,°C$ are wuestite (FeO) and magnetite (Fe_3O_4). Haematite (Fe_2O_3) will not form with CO_2 or H_2O as oxidation agent alone [8, 103] (see also Sec. 2.3).

The overall reaction in the CWGSR corresponds to the water gas shift reaction. With the help of the fixed bed, this redox reaction is split into a reduction and an oxidation reaction, which are separated in time. The fixed bed material serves as an intermediate oxygen storage. The CWGSR could be used to replace the sequence of shift reactors and a preferential oxidation unit.

The direction of the gas flow through the reactor can either stay the same throughout a cycle or change. The latter will be called flow reversal mode and is illustrated in Fig. 1.1. Most importantly, this is predicted to increase reactor efficiencies in conjunction with short cycles [45]. These predictions in turn, are based on the assumption that reaction zones form

7

inside the fixed bed, which move in the same direction as the gas phase [45, 46]. These phenomena distinguish the CWGSR from other implementations of the SIP.

1.2.1. Historical Background

Anton Messerschmitt's German patent from 1911 [66] is most commonly cited as the original source of the steam iron process (i. e. [24, 41, 48, 98]). An earlier US patent filed in 1908 [65] is also mentioned in the academic literature [60]. However, these, as well as many other patents filed by Messerschmitt in the first three decades of the 20th century all over Europe and North America[2] only claim process improvements or improved apparatuses.[3] Indeed, Messerschmitt himself references hydrogen generation by "oxidizing incandescent metallic iron by means of steam" followed by an iron oxide reduction with a reducing gas as a "well known process" [65].

Prior references in the patent literature are hard to come by. A survey requires a dedicated piece of work, since almost no patents before 1900 are digitised. They can only be accessed through the physical patent archives of the countries in question. The steam iron process itself, however, is known to varying degrees long before the second industrial revolution (or "the technological revolution") at the end of the 19th century. Antoine Lavoisier, one of the founders of modern chemistry and the one who gave hydrogen its name, produced it at the end of the 18th century by piping steam through an iron tube heated by fire. It should also be noted, that whenever a blacksmith quenches a piece of glowing iron in water, hydrogen is produced through the steam iron process. The hydrogen is then sometimes ignited above the water surface and the flame faintly visible.

Two more early patents shall be cited. Credit for the first process to continuously generate hydrogen with the steam iron process goes to Lyle S. Abbot and his US patent filed in 1915 [2], illustrated in Fig. 1.3. He describes the simultaneous, but out of phase operation of at least four reactors to the effect that at least one reactor is always in the hydrogen producing phase. The claimed apparatus is remarkably similar to modern multi-bed adsorber configurations, as applied e. g. pressure swing adsorption or temperature swing adsorption. The problem of

---

[2]Patents were filed in Austria, Canada, France, Germany, Great Britain, USA and Switzerland, possibly other countries as well.

[3]I. e. the mentioned US patent claims the addition of a certain amount of steam to the reducing gas, which may contain hydrocarbons, in order to avoid coking and to enable what is today known to be steam reforming. The often cited German patent claims the implementation of the steam iron process in, essentially, a tube-in-tube reactor which facilitates the external heating of the reactive bed, see Fig. 1.2.
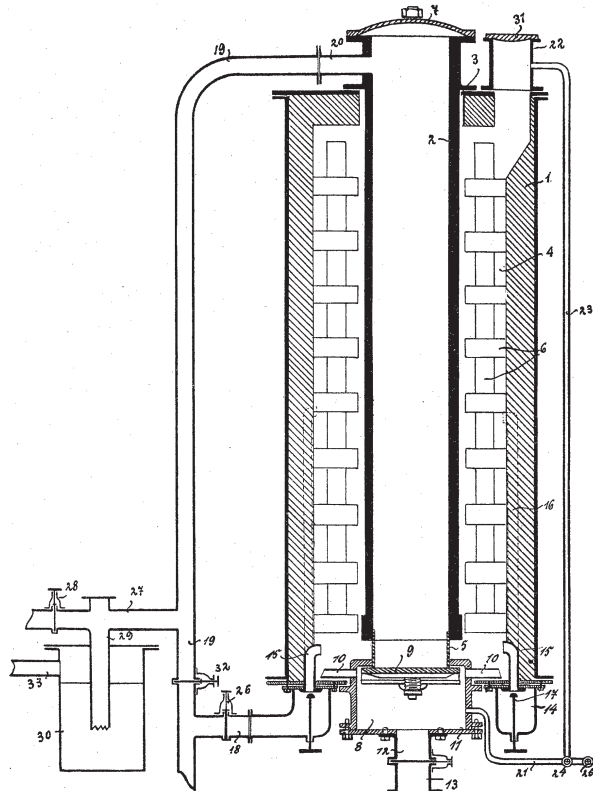
Figure 1.2.: Messerschmitt's often cited patent DE266863 [66] describes only an improved way of heating the inner iron/iron oxide reactor. It does not claim the invention of the steam iron process itself.

heating is solved by a heating stage, at which the reactor temperature is raised by hot gases flowing through them, thus avoiding the elaborate design of Messerschmitt.

Charles E. Parsons also claims the invention of a continuous steam iron process in 1926 [73]. Effectively, a moving bed reactor is employed which moves the iron material counter-currently to the gases by means of gravity and a bucket elevator, as illustrated in Fig. 1.4. It can be interpreted as a predecessor to many later designs employing fluidised beds and is the first patent using the term "steam iron process".

Due to the complex design of the SIP and higher efficiencies achieved with steam reforming and classical water gas shift reactors, the SIP technology was never commercially applied on a large scale and regained interest in the patent literature only shortly during the oil crisis of the 1970s.
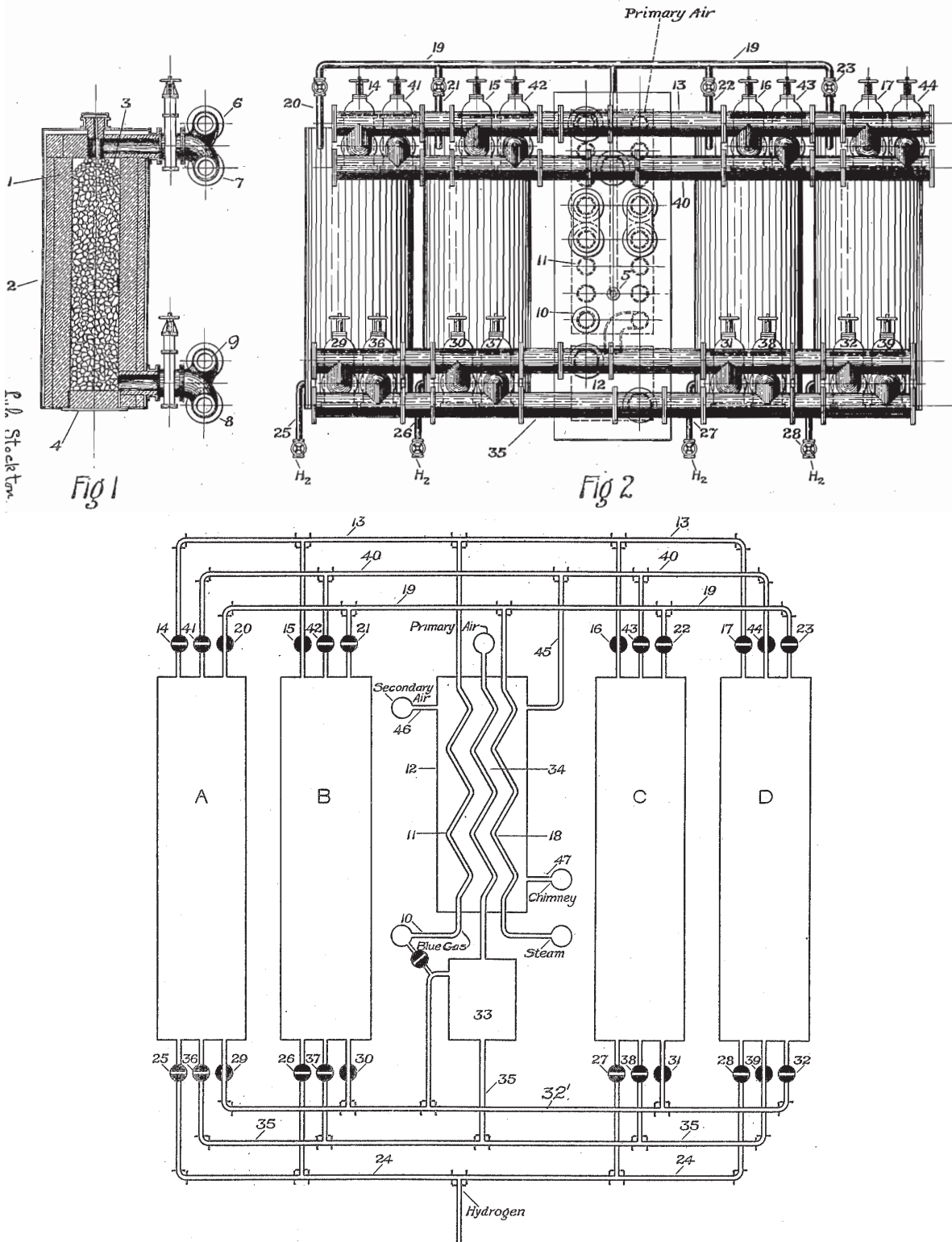
Figure 1.3.: Figures from Abbott's 1920 patent [2]. Fixed bed of iron oxides (*Fig 1*) are connected in parallel to gas fedd and product lines (*Fig 2*).By switching a series of valves (*Fig 3*) oxidation, reduction and heating phases can be operated simultaneously.
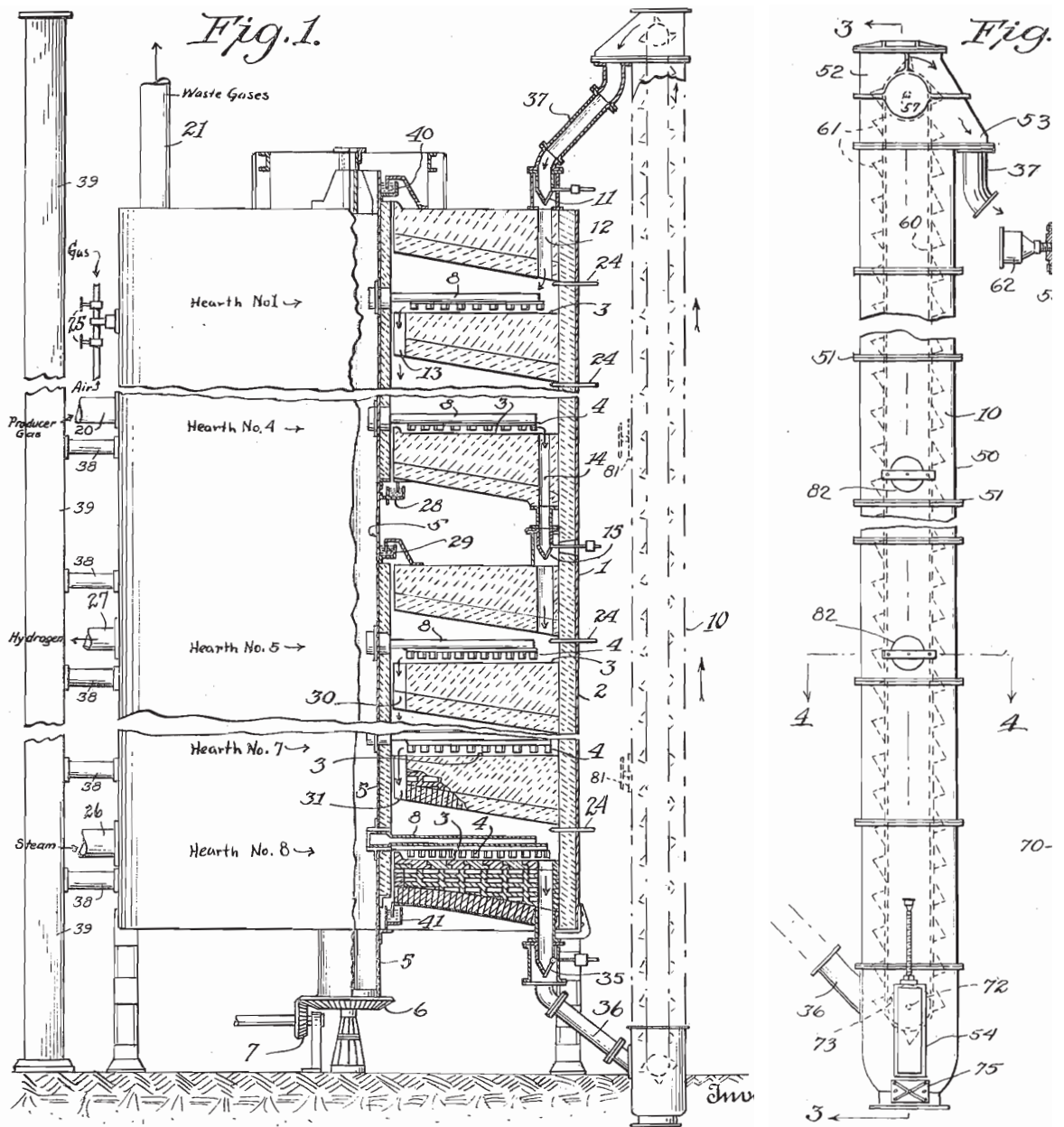
Figure 1.4.: Parsons' moving bed reactor for continuous production of H$_2$ from his 1926 patent [73]. Iron oxide is moved to the top by a bucket elevator (right) and flows via a chute system through a reduction and a oxidation zone back down again.

1.2.2. Recent Developments

Interest into the process regained strength in the last two decades as alternative forms to produce hydrogen for fuel applications came into the focus of the research community.

Hacker et al. [40, 41] and Sime et al. [86] published experimental data for the steam iron process implemented in fixed beds. They repeatedly reduced and oxidised larger amounts of commercially available iron oxide pellets. Although not stated explicitly, their reactors showed CSTR-like behaviour, i. e. gas output concentrations which could have been produced by a fluidised bed batch process. Although Hacker et al. [40] presented results from a one-dimensional mass and energy balance model, it was not explicitly stated and no conclusions regarding the operation of the reactor were drawn.

Seiler and Emig [84] have applied a spatially one-dimensional model of a CWGSR reactor based on nickel to evaluate the effect of varying operating parameters. But this model is not validated with experimental data from a CWGSR plant. Lorente et al. [61] also proposed a spatially distributed model which they used to simulate the coupling of the fixed bed with a high temperature fuel cell (SOFC). It is simplified with respect to certain details such as the reaction system and no experimental validation is shown for this model. Heidebrecht et al. [45] have published a one-dimensional, dynamic mathematical model of a CWGSR, but without taking thermodynamic limitations for chemical conversions into account and, again, without experimental validation.

Heidebrecht and Sundmacher [46] formulated a shortcut model for a CWGSR. Based on a one-dimensional representation of the reactor, rapid gas flow reversal, and assuming thermodynamic equilibrium between gas and solid, their model reduces to a few algebraic equations, which can be used to estimate cyclic steady states of the reactor.

Some groups investigated the integration of a reformer with a fixed bed implementation of the steam iron process, like Hacker et al. [39], Kindermann et al. [53] and Fraser et al. [24].

The bulk of the research works focused on the implementation of the steam iron process in fluidised beds, often in conjunction with reforming methane (e. g. Chiesa et al. [13], de Diego et al. [18], Go et al. [33] or Wolf et al. [105]), pyrolysis oil (Bleeker et al. [6]) or coal (Cleeton et al. [15], Yang et al. [107]). Many of those publications include investigations on complete H_2 production systems.

The CWGSR was used in process systems simulations on electricity production from biomass by Hartono and Heidebrecht [43, 44]. Logist et al. [59] optimised operating parameters

of a CWGSR based on the dynamic one-dimensional CWGSR model by Heidebrecht et al. [45].

Several names for the process and related technologies emerged and are used in the literature. A short overview is attempted here:

Steam Iron Process (SIP) Most common name to reference the two-step process of generating hydrogen with steam and iron, and reducing the formed iron oxide thereafter with reducing gas.

Sponge Iron Process/Reactor (SIP, SIR) Essentially the same as the steam iron process. The emphasis is on using "sponge iron", which is formed by reducing naturally occurring iron ore and has a high porosity and large active surface. The term is most often used in the vicinity of the group of Hacker at TU Graz (i. e. [40, 42, 98]). The term *sponge iron* (although without "process" or "reactor") predates the use of *steam iron process* in the patent literature (see Messerschmitt [65] vs. Parson [73]).

Cyclic water Gas shift reactor (CWGSR) (Germ.: Zyklischer Wassergas Shift Reaktor, ZWGSR) used in the group of Sundmacher in Magdeburg (i. e. [25–30, 43–48]) to denote the steam iron process implemented in a fixed bed, utilising dynamic phenomena like moving reaction zones. The fixed bed material is, in principle, not limited to iron oxide.

Reformer Sponge Iron Cycle (RESC) A steam iron process downstream of a hydrocarbon reformer. Most often used in the group of Hacker at TU Graz (i. e. [24, 39, 98]).

1.2.3. Comparison With Other Reactor Concepts

Several other reactor and process concepts share some of the properties of the CWGSR.

The steam iron process can be classified as a chemical looping reactor. This is a general class of processes, where a solid or liquid is repeatedly subject to a two or three step chain of reactions in as many reactors or temporal stages. It is usually used to extract a part of a gas stream (free or covalent bound) and to release it in a second gas stream. Examples are the steam iron process (SIP) to extract covalently bound oxygen from steam and release it in a syngas stream by oxidising it; chemical looping combustion (CLC) to extract molecular oxygen from air and release it into a fuel stream; or calcium looping (CaL) to extract CO_2

from combustion off-gases and release it in a pure CO_2 stream. Chemical looping reactors are usually implemented in fluidised bed reactors.

The CWGSR shows similarities to other cyclically operated fixed bed reactors, like a recuperating (Matros) reactor used for catalytic combustion of diluted volatile organic compounds (Matros and Bunimovich [64]). Or periodically operated fixed bed reformers (Glöcker et al. and Eigenberger [32]). These fixed beds usually promote certain reactions and store heat: An exothermic reaction is used to heat up the bed, so that an endothermic reaction can be conducted therein afterwards. However, the CWGSR differs in one important aspect to these reactors: besides promoting reactions and storing heat, it also serves as an oxygen storage. Thus, the model equations and especially the results from the model analyses of cyclically operated fixed beds cannot be directly transferred to the CWGSR.

Adsorption beds are similar to the CWGSR in that they store material and exchange them between the operating phases. However, in a chromatographic column, the composition of the solid phase (adsorbend) is more or less uniquely correlated to the gas phase via an adsorption isotherm, which is continuously differentiable. This is not the case with the gas-solid reactions in the CWGSR, where several gas compositions can be in equilibrium with a solid species (see Sec. 2.4). This forces the formation of shock waves in the CWGSR, which occur in adsorption beds only for nonlinear adsorption isotherms [32, 46].

1.3. Objectives Of This Work

Based on the idea of implementing the steam iron process in a fixed bed with potentially rapid gas flow reversal, this work seeks to contribute to the development of the CWGSR by

- Investigating the gas-solid reaction kinetics of an iron-based material: Experimental study of all oxidations and reductions involving Fe, FeO and Fe_3O_4 and their dependency on temperature, gas and solid composition. Formulation of kinetic expressions which are consistent with the experimental data and thermodynamic equilibria.

- Experimental analysis of a CWGSR. Confirmation of assumptions (reaction fronts [46]) as well as predictions (advantageous gas flow reversal mode [47], operating regimes [46]) of previously published models.

- Derivation of a model of the CWGSR based on the experimental findings, which can be used for detailed analysis and optimisation of the reactor.

2. Oxygen Storage Materials

The material used as the oxygen storage material in this work, i. e. the fixed bed of the CWGSR, should naturally be based on a metal which can act as an oxygen carrier within redox reactions with $CO/CO_2/H_2/H_2O$. Additionally, it has to have a bigger set of optimal properties to be the material of choice. The bed material is subjected to high stress, due to the high operating temperature as well as the constant change of chemical composition and crystal structure. The material is therefore very prone to sintering on a microscale.

The sintering decreases two important properties of the material over the course of its operating time: surface area, i. e. reactivity, and the available oxygen storage capacity. The capacity of a fixed bed to store oxygen is dictated by the amount of storage material close to a gas-solid surface, since mass transport in the solid may be too slow for practical application depending on the material (see Sec. 2.2.3).

The aforementioned stress which the material is subjected to, also leads to structural instability on the macroscale. This is experienced as the reactor concept is scaled up and the oxygen storage material has to be pelletised to keep the pressure drop over a fixed bed managable. Simple pressure molded pellets disintegrate easily.

Any additives or supports of the material should be chemically stable. Any side reactions, especially irreversible ones of the solid reactants, are unwanted. All those properties should of course be in balance with the materials price or ease of acquisition, relative to its oxygen storage capacity.

Many metals have been considered for this process in the literature, with iron, nickel, copper and manganese as the most promising materials [92, 109]. Iron was chosen in this work for its low cost, good availability and high reactivity [3, 14, 37, 97].

In the present worrk, two iron-based materials were used: One, developed by Vladimir Galvita at the Max Planck Institute for Dynamics of Complex Technical Systems in Magdeburg [25–30], which specifically addresses the properties and requirements discussed above. This material was used in the kinetic measurements presented in Ch. 3 and is described in detail in Sec. 2.1.2. The second material was made from commercially available iron oxide

with the emphasis on expendability. It was used in preliminary proof of concept experiments of the CWGSR and is described in Sec. 2.1.1.

2.1. Applied Materials

2.1.1. Pure Iron Oxide

This material is easy and fast to prepare. It consists of laboratory-grade, commercially available Fe_2O_3 powder from Strem Chemicals with an average particle size of $d_{50} = 1.8\,\mu m$ and a purity of $> 99.8\,\%$. A sodium silicate solution was used as a binding agent to form pellets as described in Sec. 2.2.1.

This material was prone to fast degradation. Nevertheless, the proof of concept experiments of the CWGSR described in Ch. 4 could be performed with it.

2.1.2. Stabilised Iron Oxide

Galvita et al. [25–27, 29, 30] especially addressed the problem of sintering of the iron based oxygen storage material. The sintering, sped up by high temperatures and solid-solid phase transitions between crystal structures of the different oxides, leads to a very rapid loss of surface area and reactivity over the number of performed redox cycles. This translates to a decline of the usable oxygen storage capacity during long term CWGSR operation.

A solution to this problem was found by adding other metal oxides to the iron material. Especially $CeZrO_2$ was found to mitigate the sintering processes. In a detailed study [25], the $CeZrO_2$ content was systematically varied. The optimal composition was found to be 80 m% Fe_2O_3 and 20 m% $Ce_{0.5}Zr_{0.5}O_2$. This material was used in the kinetic analysis of Ch. 3 in this work.

The preparation of the material was done via urea hydrolysis from the following chemicals: $Fe(NO_3)_3 \cdot 9H_2O$ (99.99+%, Sigma-Aldrich), $Ce(NO_3)_3 \cdot 6H_2O$ (99.99%, Aldrich), and aqueous $ZrO(NO_3)_2$ (Fluka). For details see the publication by Galvita et al. [25]. The synthesis yields a fine powdery material which was pressed, milled and sieved to obtain particles with a size distribution of 280 to 560 μm. These particles are agglomerates of smaller sized crystals in the 100 nm range, see Fig. 2.1. The BET surface area ranges from 10 (fresh) to 5 m^2/g after several redox cycles [30].
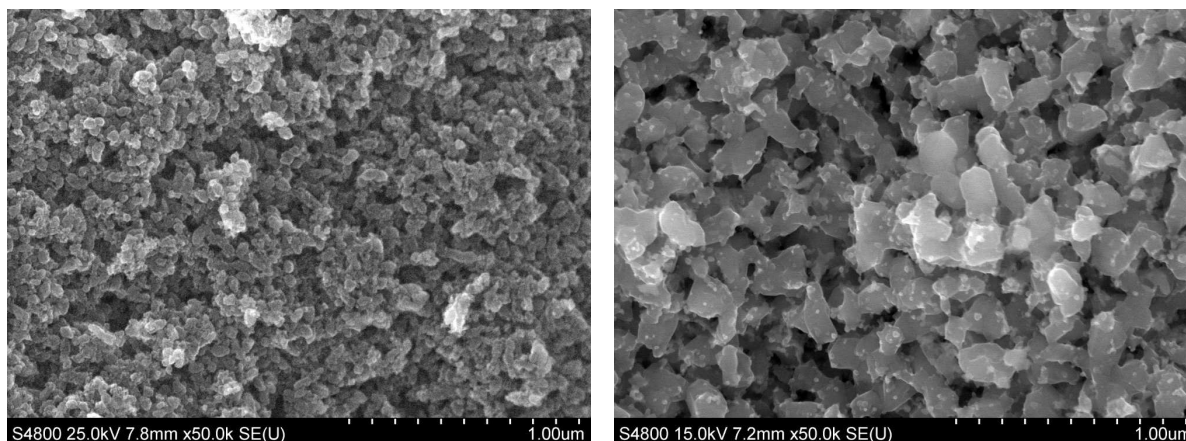
Figure 2.1.: SEM images of the 80 m% Fe_2O_3 and 20 m% $Ce_{0.5}Zr_{0.5}O_2$ material after synthesis (left) and after 100 redox cycles (right). Images from [25].

The inclusion of non-iron oxides introduces the possibility of additional reactions during the cyclic operation. Galvita et al. suggest that CeO_2 converts to Ce_2O_3 during a reduction phase [25, 29, 30]. However, these reactions will be neglected in the kinetic analysis of this work for two reasons:

a.) Ceria and Zirconia exist in a number of different compounds in the material, e. g. CeO_2, ZrO_2, $CeFeO_3$, $CeZrO_2$, as Galvita showed by XRD measurements [25]. Sim et al. [85] describe a much more complex situation in a similar material (WO_3 stabilised with CeO_2 and ZrO_2). The incorporation of all the corresponding reactions leads to very complex models not suitable for reactor optimisation.

b.) The importance of side reactions to the overall capacity of the oxygen storage material is negligible. A reduction of CeO_2 to Ce_2O_3 would account for 0.34 mmol of oxygen per gram of storage material. Whereas the reduction of Fe_3O_4 to Fe will yield 12 mmol, about 35 times as much (see Appendix A.1 for the corresponding calculations).

2.2. Pelleting

Pelleting of the iron oxide powder was necessary to keep the pressure loss in a tubular reactor sufficiently low. The goal was to create pellets of 3 mm in diameter, which are structurally stable during repeated redox and temperature cycles.

These goals could not be achieved by solely applying high pelleting pressure. Thus, a binding agent was needed. An aqueous solution of sodium silicate, or "waterglass" was suc-

cessfully applied as binding agent. This material improves the stability also on the microscale, as it is reported that a high SiO_2 content in iron ores correlates with low sintering rates [98].

The chemical inertness of waterglass in CWGSR conditions was tested by treating the pellets in Fe_2O_3-state with a $5\,g\,h^{-1}$ steam flow for $4\,h$ at $600\,°C$. Sodium was not found to be released by H_2O from the fixed bed during the simulated oxidation step. Negligible weight loss was observed, but attributed to the handling ($437\,mg$ to $435\,mg$ after treatment). Therefore, the binding agent was treated as inert in this work.

2.2.1. Pure Iron Oxide

To pellet the commercial Fe_2O_3 powder, $5\,m\%$ of sodium silicate were added to an aqueous slurry of the iron oxide (e. g. $0.8\,L\,H_2O$, $500\,g\,Fe_2O_3$, $75.2\,g$ of a $35\,m\%$ sodium silicate solution[1]). The paste was thoroughly mixed and spread on a tray to form a layer of $1\,cm$ thickness. The sheet was dried, broken to pieces and sieved. Finally, the 2.24 to $5\,mm$ fraction was calcined at $800\,°C$ for $10\,h$. The resulting pellets (see Fig. 2.2) were mechanically stable in the CWGSR over many redox cycles and fused only slightly with each other while maintaining their porosity (see Fig. 2.3). In contrast, calcination at $650\,°C$ produced pellets which disintegrated to their powdery source material during the first reduction, thereby completely blocking the reactor.

The Fe_2O_3-pellets are slightly hydrophobic and suitable for measuring the packed bed porosity by water displacement. In a cylinder with the same inner diameter as the reactor ($2\,cm$), the packed bed porosity was found to be $\varepsilon_{packed\,bed} = 0.51$; the average packed bed bulk density is $\rho_{packed\,bed} = 0.81\,g/cm^3$. The density of a pellet is therefore $\rho_{Pellet} = 1.64\,g/cm^3_{Pellet}$. Assuming a solid density of the iron oxide material with $5\,m\%$ waterglass of $5\,g/cm^3$, the pellet pore volume fraction computes to approximately $\varepsilon_{pellet} = 0.6$. This high porosity is probably due to the generation of gaseous H_2O and CO_2 during heat treatment and solidification.

2.2.2. Stabilised Iron Oxide

The material developed in-house was not used in the reactor as described in Ch. 4. Attempts to pellet the material were not successful.

The preparation method was the same as described in the previous section, with the exception of using $3\,mm$ PTFE moulds to form the pellets. This helped to considerably conserve

---

[1]"Natronwasserglas, reinst", Merck Millipore, Order No. 1 05621

Figure 2.2.: Pellets made from Fe_2O_3 and sodium silicate after preparation.

(a) Slightly fused part of the fixed bed. The missing length disintegrated to its constituent pellets upon removal from the CWGSR tube.

(b) Detail view of the CWGSR fixed bed. Visible is the high porosity of granular the material.

Figure 2.3.: Part of the fixed bed of the CWGSR after about 20 redox cycles and 3 thermal (room to operating temperature) cycles, in reduced state.

material and speed up preparation. However, the calcined pellets were too fragile to with-stand even one single reduction. The main reason might be the much coarser base material ($d_{50} = 50\,\mu m$). Possible solutions to produce more stable pellets are using more waterglass at the possible expense of blocking more reactive surface with the binding agent or milling the source material down to a similar size as the commercial material.

2.2.3. Possible Mass Transport Limitations

The dynamic behaviour of a whole fixed bed will be measured, modelled and analysed in this work. These dynamic phenomena are influenced amongst others by reaction rates and mass transport rates. The reaction rates for small particles will be measured in Sec. 3 and applied in a model of a fixed bed in Sec. 4.2. If reaction rates are limited by mass transport rates, a model employing the reaction rates will not fit the experimental data or lead to wrong conclusions.

Several scenarios for mass transport limitations on the pellet level are therefore investigated to determine their time scales or characteristic time constants. If these are in the order of typical time scales observed for dynamic phenomena in the fixed bed reactor of about 5 to 50 min (see Sec. 3.1), the observed dynamics are likely governed by mass transport limitation. A model of the reactor would have to include these effects.

Refer to Fig. 2.4 for an overview of the different elements of the fixed bed, which based on the pure iron oxide material (Sec. 2.1.1 and 2.2.1). There are three conceivable rate determin-ing limitations which can dominate the reactor dynamics:

a.) Assumption: All primary particles in the pellets are accessible by gas phase; Gaseous diffusion in the pellet controls the mass transfer. As discussed previously, the pellets are highly porous ($\varepsilon = 0.6$) with an average primary particle size of $2\,\mu m$. Free diffusion, as opposed to Knudsen diffusion, is therefore assumed to be dominating with a coefficient of $D = 10^{-4}\,\mathrm{m^2\,s^{-1}}$ at reactor operating conditions (see the Sec. A.3 for estimation). The pellet size is about $l = 10^{-3}\,\mathrm{m}$. The characteristic time constant of mass transport in the pellet's gas filled pores can be obtained from:

$$\tau = \frac{l^2}{D} \tag{2.1}$$

With the parameters discussed above this yields to $\tau = 10^{-2}\,\mathrm{s}$. Thus, under typical experimen-tal conditions with reduction times of 5 to 50 min (see Sec. 4.1), intrapellet gaseous diffusion is too fast to limit the actual reaction kinetics.
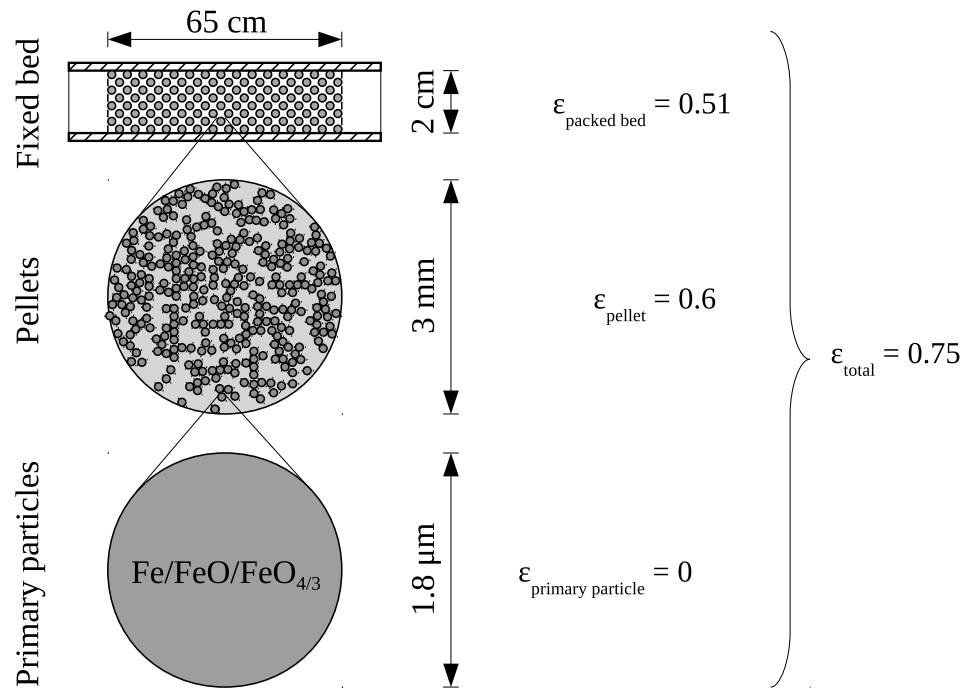
Figure 2.4.: Scale comparison of the different elements of the CWGSR fixed bed made from commercially available Fe_3O_4.

b.) Assumption: Gas pores in the pellet are totally blocked and the main transport mechanism of oxygen in the pellet is by solid diffusion in the iron / iron oxide lattice. If sufficiently slow, solid diffusion might control the reaction kinetics. Maier [63, p. 299] states a diffusion coefficient of $D = 10^{-12}\,\mathrm{m^2\,s^{-1}}$ for oxygen ions in iron oxides at 900 °C. Combined with the pellet's size, Eq. (2.1) yields a typical time constant of about 10^6 s for the complete reduction of a whole pellet. This is far longer than the observed reaction times.

c.) Assumption: Gas phase mass transport to the pellets' primary particles is sufficiently fast, but rate limitations arise due to mass transport processes inside the primary particles. Combining the diffusion coefficient of case b.) with the primary particle size of about 10^{-6} m, a typical time of 1 s can be associated to this transport process. This is again too fast to have a measurable effect on the experiment's results.

It is therefore concluded that the dynamic phenomena observed in the fixed bed reactor and discussed in Sec. 3.1, like the change in the rate of carbon monoxide consumption, are most likely to be governed by the reaction rates, which were measured on primary particles.

1:	$3\,FeO_{4/3} + CO$	$\rightleftarrows$	$3\,FeO + CO_2$
2:	$FeO + CO$	$\rightleftarrows$	$Fe + CO_2$
3:	$3\,FeO_{4/3} + H_2$	$\rightleftarrows$	$3\,FeO + H_2O$
4:	$FeO + H_2$	$\rightleftarrows$	$Fe + H_2O$

Table 2.1.: Main gas-solid reactions of the CWGSR considered in this work.

2.3. Reactions Considered

The main chemical reactions occurring in the CWGSR are listed in Tab. 2.1 and consist of the reduction of Fe_3O_4 and FeO with CO or H_2, as well as their counter reactions. Reactions involving Fe_2O_3 are not considered, as the oxidation of Fe_3O_4 with CO_2 or H_2O is thermodynamically not feasible at the chosen reactor operating pressures and temperatures ($T = 574\ldots750\,°C$, $p = 1\ldots10\,bara$) [6, 103].

FeO and Fe_3O_4 are treated as distinct chemical species, not as mixtures of other species. In this present work FeO is assumed to have a fixed stoichiometric ratio of 1 between iron and oxygen atoms. A more detailed and correct observation of FeO being a mixture of different oxides with a varying total stoichiometric ratio of 0.865 to 0.955 [103] is neglected. The terms Fe_3O_4 and $FeO_{4/3}$ are used interchangeably in the text of this work to refer to magnetite. The species $FeO_{4/3}$ is used in all calculations and models. The quantity of iron in a mole of any iron oxide is therefore always the same, which simplifies calculations.

The deposition of solid carbon on the fixed bed is assumed to take place via the Boudouard reaction:

$$C + CO_2 \rightleftarrows 2CO \tag{2.2}$$

The formation of iron carbide (Fe_3O) is neglected because of its instability at CWGSR operating conditions [103].

2.4. Chemical Equilibria

The conversion of gases in the system described in Tab. 2.1 is severely limited by the thermodynamic equilibria of the respective chemical reactions. The Baur Glaessner diagram has become a standard tool to visualise these equilibria in metallurgy and is also used in this

work [8, 103]. Fig. 2.5 shows two Baur Glaessner diagrams for the reaction system under discussion.

These diagrams show existence regions of certain oxidation states of solids as function of temperature and gas composition. The temperature on the abscissa applies to both gas and solid phase. The ordinate defines the gas phase composition. The relative H_2O, resp. CO_2, content is given on a scale of 0 to 1. It is defined by the mole fractions of the reactive gas species, as given in Eq. (2.3).

$$y_{H_2O} = \frac{x_{H_2O}}{x_{H_2} + x_{H_2O}} \qquad ; \qquad y_{CO_2} = \frac{x_{CO_2}}{x_{CO} + x_{CO_2}} \qquad (2.3)$$

The diagrams are split into three regions, where either Fe, FeO or Fe_3O_4 exist. No mixtures of solid species can exist under thermodynamic equilibrium conditions, except on the boundaries of these regions as specified in the diagram. FeO is only stable at temperatures above a threshold temperature of 574 °C. For this reason, the oxidation of Fe to Fe_3O_4 will have no intermediate step at temperatures below this threshold. Due to the fact that the CWGSR as described in this work, is not operated at temperatures below 574 °C, this direct conversion of Fe to Fe_3O_4 can be neglected. The equilibria of the reactions in Tab. 2.1 are only sensitive to the ratio of partial pressures of the gaseous reactants. Dilution by inert gases or a change of the pressure of the gas mixture do not have any effect due to the equimolarity of the reactions w. r. t. to the gas phase. As mentioned in the Sec. 2.3, the stoichiometric ratio of iron and oxygen in FeO is not exactly 1 and not completely constant in the region denoted as "FeO" in the Baur Glaessner diagram. Nevertheless, this assumption of a fixed FeO species was taken for the sake of a simplified analysis. A more detailed analysis of iron(II)-oxide is given by Bogdandy [8].

If a given gas mixture comes in contact with a solid phase that does not match the domain given in the Baur Glaessner diagram, a reaction will occur until a chemical equilibrium is achieved. Illustrated in Fig. 2.6 is as example: A gas with $y_{H_2O} = 0.8$ is brought in contact with a solid of FeO at $T = 750$ °C. The solid will be oxidised to Fe_3O_4 and the gas will be reduced to $y_{H_2O} \approx 0.6$. This process is visualised in the diagram as a point, denoting the gas composition, moving from $y_{H_2O} = 0.8$ and 750 °C horizontally (isothermally) to the left, until the boundary between the FeO/Fe_3O_4 regions is met. From that point on, the gas has no driving force or oxidation potential left to oxidise the solid any further, or be reduced by the material toward lower y_{H_2O}.
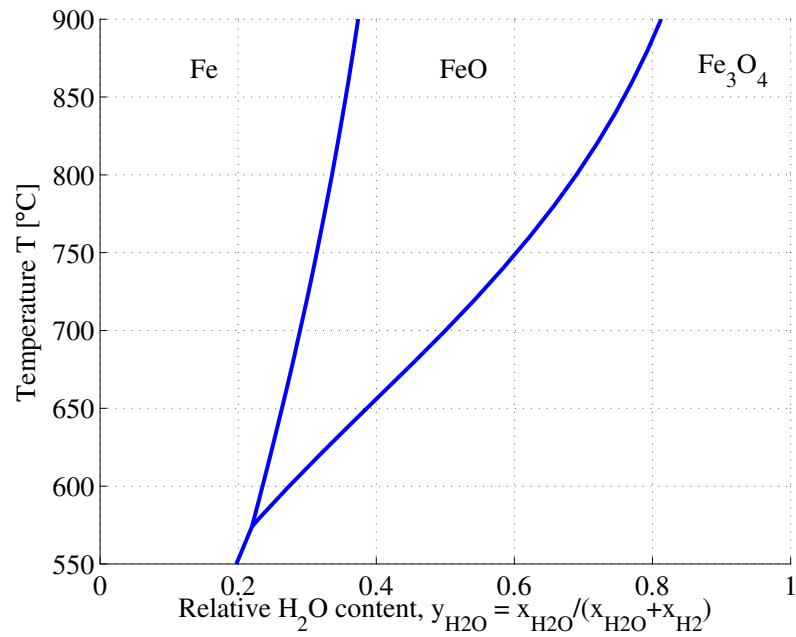
(a) Iron / iron oxide in hydrogen / steam.
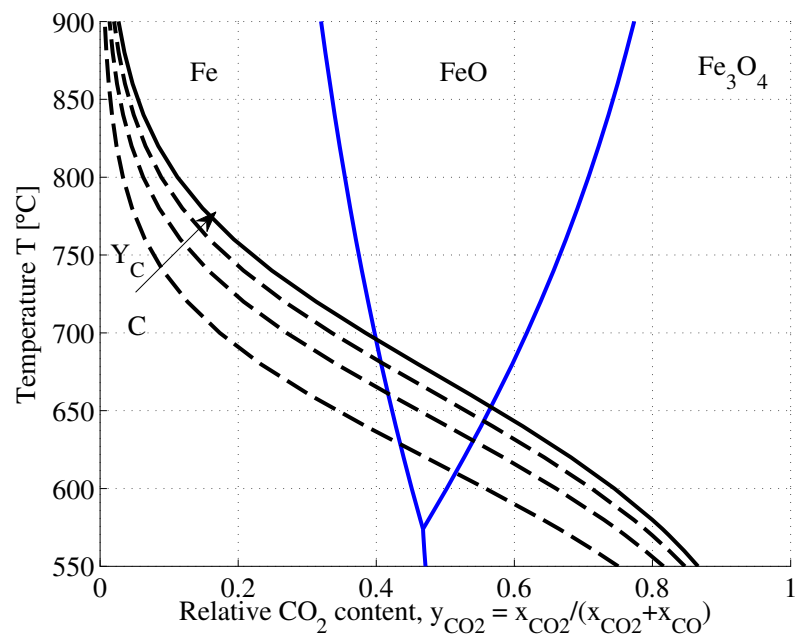
(b) Iron / iron oxide in carbon mon-/dioxide. Additionally, the equilibrium of the Boudouard reaction (at $Y_C = 0.25, 0.5, 0.75, 1$) is marked by the black lines.

Figure 2.5.: Baur Glaessner diagrams showing regions of gas-solid systems in equilibrium. Based on data of Tab. 2.2. Parameters defined in Eqs. (2.3), (2.4).
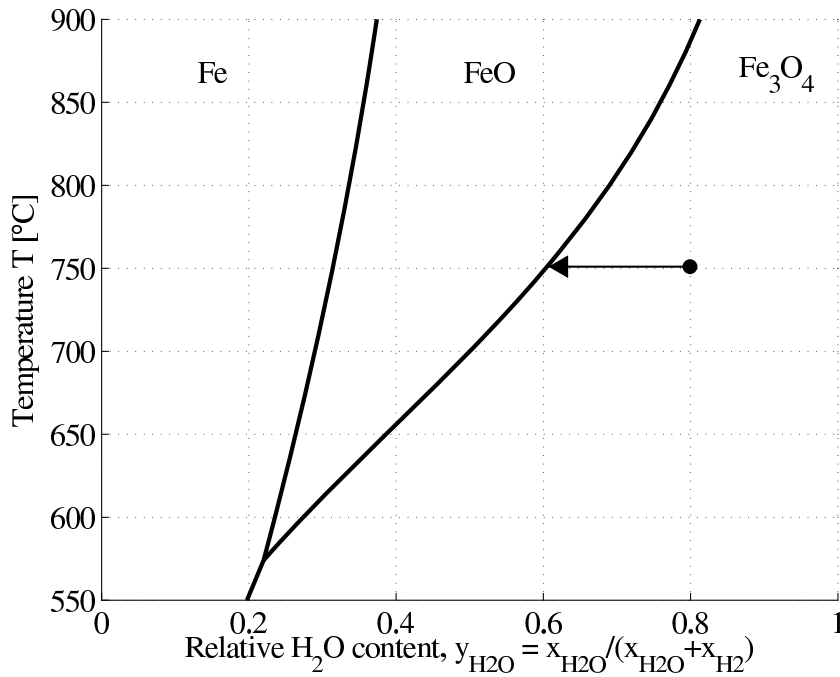
Figure 2.6.: Illustration of the reduction of a gas ($y_{H_2O} = 0.8$, $T = 750\,°C$) with FeO. The gas is in equilibrium with FeO and Fe_3O_4 at $y_{H_2O} = 0.6$ and cannot be reduced further at this temperature without Fe available.

With the Bauer Glaessner diagram at hand, one can easily estimate the maximum conversions in the CWGSR. Steam entering the reactor at $750\,°C$ will be converted by $40\,\%$ ($70\,\%$) to H_2 if enough FeO (resp. Fe) and time is given. The lower the temperature, the more favourable the equilibria will be. The opposite judgement of the temperature dependence will be given for the reaction in the opposite direction, i. e. the reduction. A CO conversion of $38\,\%$ ($66\,\%$) to CO_2 can be achieved at the same temperature.

The black lines in the CO/CO_2 diagram of Fig. 2.5 show the equilibrium of the Boudouard reaction. Coking will occur in the region to the left of the line, which grows with lower temperatures. At these lower temperatures, coking is more likely to occur albeit the reaction rate will be slower. Coking has to be avoided in the CWGSR, as it decreases active surface area. A reaction of steam with carbon to carbon oxide during oxidation phase will also be likely, which misses the objective to produce CO-free hydrogen. Solid carbon deposits are not favoured thermodynamically to the right of the line. Since this reaction is nonequimolar w. r. t. to the gas phase, it is sensitive to the overall amount of carbon in the atmosphere. The

	$FeO_{4/3}$	FeO	Fe	H_2	H_2O	CO	CO_2	C
$\Delta_f h^\ominus$ /J mol^{-1}	-326795	-224865	30556	20688	-215794	-88824	-360092	11785
$\Delta_f s^\ominus$ /J mol^{-1} K	118.90	120.46	65.94	166.22	232.75	234.54	269.32	24.51
$c_p(T)$/J mol^{-1} K^{-1}	77.97	75.36	50.48	30.85	43.24	33.95	55.89	19.74

Table 2.2.: Thermochemical data used for equilibrium calculations [8, 58]. $T = 1000\,\text{K}$

parameter Y_C is introduced in Equ. 2.4 to describe this carbon content. The equilibria are plotted from left to right for Y_C of 0.25, 0.5, 0.75 and 1.

$$Y_C = x_{CO} + x_{CO_2} \qquad (2.4)$$

These diagrams and the presented equilibria can be computed by applying the mass action law of each reaction as a function of the temperature; here, exemplified for reaction 1:

$$\frac{x_{H_2O}}{x_{H_2}} = \exp\left(-\frac{\Delta_r g^\ominus(T)}{RT}\right) \qquad (2.5)$$

Equ. 2.5 assumes ideal behaviour of the gases. With Equs. 2.5 to 2.7, Equ. 2.8 can be derived, which can directly be used to plot the Baur Glaessner diagrams.

$$\frac{y_{H_2O}}{y_{H_2}} = \frac{x_{H_2O}}{x_{H_2}} \cdot \frac{x_{H_2O} + x_{H_2}}{x_{H_2O} + x_{H_2}} \qquad (2.6)$$

$$1 = y_{H_2O} + y_{H_2} \qquad (2.7)$$

$$y_{H_2O} = \exp\left(-\frac{\Delta_r g^\ominus(T)}{RT}\right) / \left(1 + \exp\left(-\frac{\Delta_r g^\ominus(T)}{RT}\right)\right) \qquad (2.8)$$

The standard free enthalpy of a reaction as a function of temperature, $\Delta_r g^\ominus(T)$, is calculated via the values of the standard enthalpy and entropy of formation, $\Delta_f h^\ominus$ and $\Delta_f s^\ominus$, and the heat capacity c_p at 1000 K, as listed in Tab. 2.2. The values for the gases H_2, H_2O, CO, CO_2 and C were taken from NIST data [58]; The value for the solids Fe_3O_4, FeO and Fe were obtained from Bogdandy's publication [8].

3. Reaction Kinetics

The acquisition of kinetic parameters and models is one of the fundamental prerequisites for the design of a chemical reactor. The goal of this chapter is the determination of an applicable model for the heterogeneous chemical reactions in the system $Fe/FeO/Fe_3O_4 - H_2/H_2O - CO/CO_2$, as shown in Tab. 2.1, which is adequate for use in the CWGSR model discussed in Ch. 4.

The reduction of iron oxides is one of the more investigated chemical reaction systems, since the production of iron is an elementary technical process of our industrial age. The overwhelming part of these investigations (e. g. [10, 96, 99, 100]), however, focuses only on the complete reduction of iron oxide ores to iron in the presence of $C–CO/CO_2–H_2/H_2O$. Other studies focus on temperatures at which FeO is not present (e. g. [60]). The design of the CWGSR on the other hand, requires knowledge about the iron oxidation states Fe, FeO and Fe_3O_4, as well as the rate of the individual reduction *and* oxidation steps. The published kinetic parameters show a high variation. The review by Pineau et al. [77] lists activation energies from 13.4 to $167\,\mathrm{kJ\,mol^{-1}}$. The most likely reason is the high sensitivity of these parameters to the employed form of iron oxide, namely the source of the ore or the synthesis of the iron material and its physical preparation/handling before the kinetic experiment is started.[1] The iron-based material which was planned to be used in the CWGSR was especially synthesised for its purpose at the Max-Planck-Institute in Magdeburg. A specific kinetic study for this material was therefore deemed necessary.

To quantitatively observe the reaction behaviour, experiments by thermogravimetric analysis (TGA) were conducted (Sec. 3.1). The modelling of the measurement method and reaction kinetics are the focus of Sec. 3.2. The following Sec. 3.3 describes the fitting procedures as well as the final kinetic model with its parameter set. A summary is given in Sec. 3.4.

---

[1]A broad review is given by Szekely et al. [95, Ch. 8]. The determined kinetics depend strongly on the type of material, its properties (porosity), source (natural, synthetic) and trace minerals. This is also stressed by another review of Pineau et al. [76].

3.1. Experimental

This section describes the acquisition of the raw data used in the following sections to determine rate expressions for the reaction kinetics. The material used for this kinetic study was the in-house material described in Sec. 2.1.2.

3.1.1. Setup

To investigate the reaction kinetics, the technique of thermogravimetric analysis (TGA) was employed.

Traditionally, TGA involves heating a solid sample over a period of time while measuring its weight. This is usually done in an inert atmosphere. The evolution of weight over time or temperature is used to study processes like drying and thermal decomposition.

However, this technique can be extended to study a wide range of chemical reactions which involve solid and gaseous reactants by controlling not only the temperature, but also the atmosphere in the measuring cell. Reactions can therefore arbitrarily be defined, started and stopped on the weighing pan. The extent of reaction is tracked via the weight of the solid reactant. Since weighing can be a lot more precise and have shorter response times than, e. g. measuring the effluent gas composition over time, this technique can give better defined information on a solid-gas reaction – albeit only a single quantity is measured.

The equipment used in this study's setup comprises two main parts: gas supply & dosage and the TGA/SDTA851^e by Mettler-Toledo (see Fig. 3.1). The latter functions as a heated differential reactor with a weighing arm connected to a scale to support the solid sample. Attached to the inlet is the gas dosage unit with the ability to supply an inert purge gas (N_2), a $CO/CO_2/N_2$ mixture to study reaction 1 and 2 of Tab. 2.1 and a H_2/N_2 mixture. Both the TGA, and the valves and mass flow controllers (MFCs) of the gas supply are controlled by a programmable logic control (PLC). The latter is also used as a synchronised data recorder.

3.1.2. Procedure

The goal of this study was to characterise all eight reactions of Tab. 2.1 separately. In order to do this, the sample was exposed to a gas mixture that would only allow the reaction to the next oxidation state. E. g. the reduction of Fe_3O_4 in a CO/CO_2 atmosphere at 750 °C would only be studied in a gas with a y_{CO_2} between 0.38 and 0.68 (see Eq. 2.3, p. 25). This would result in
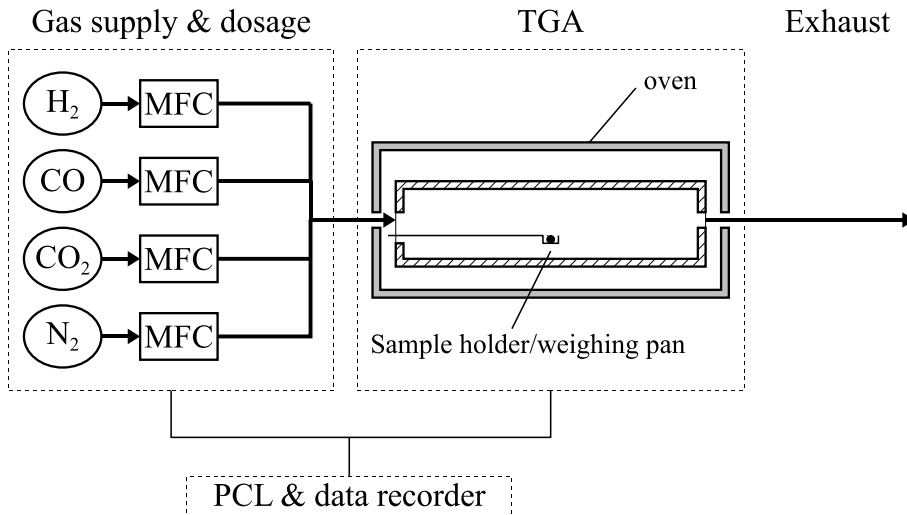
Figure 3.1.: Simplified flow scheme of the kinetic study's experimental setup.

a reduction to FeO, whereas a lower CO_2 gas concentration level, y_{CO_2}, would further reduce the material to Fe (see Sec. 2.4 for a discussion of the chemical equilibria of the system).

After achieving the steady state, the gas mixture was changed to induce the reaction to the next oxidation stage. A typical sequence for the sample in reduction experiments was therefore $Fe_2O_3 \rightarrow Fe_3O_4 \rightarrow FeO \rightarrow Fe$ as seen in Fig. 3.2. In oxidation experiments, the sequence was $Fe_2O_3 \rightarrow Fe \rightarrow FeO \rightarrow Fe_3O_4$. The samples cannot be oxidised to Fe_2O_3 (see Sec. 2.3); Only freshly synthesized material contains Fe_2O_3, as confirmed in XRD measurements. The material was not recycled for another oxidation or reduction sequence because degradation of the material and thus changes of the kinetic parameters was expected. This important field of study was part of other studies, e.g. [7, 25]. All experiments were conducted at isothermal conditions at 650, 700, 750 and 800 °C. A typical sample size was 10 mg and the total flow of the gas phase was 0.120 NL/min.

The design of the experimental parameter variation was done with the objective of robust parameter identification, i.e. fitting. This means that all experimental parameter except one (gas parameters Y_H/Y_C, y_{H_2O}/y_{CO_2}; temperature T) were held constant, while the remaining was varied three or four times. This prevented the need for simultaneous fitting of more than two parameters at a time. Once all parameters were estimated through this procedure, a good set of starting values for a fit of a complete set of parameters to a complete set of experiments was had. See Sec. 3.3.1 for more information.

The range of experimental parameters used is visualised in Fig. 3.3. Every experimentally applied gas mixture and temperature is marked in the Baur Glaessner diagram. Not shown
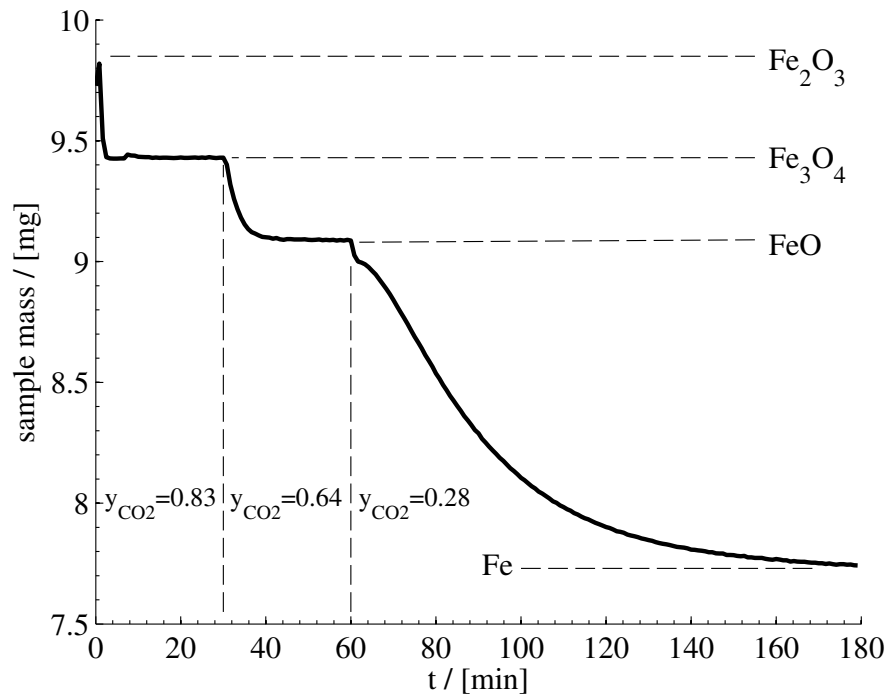
Figure 3.2.: Exemplary TGA measurement of an iron oxide reduction with CO/CO$_2$. The sample mass decreases over time as the sample reacts with CO and looses oxygen atoms to the gas. The gas atmosphere was switched after 30 and 60 min to allow the reduction to the next oxidation state of the sample. The experimental parameters are marked red in the equilibrium diagram of Fig. 3.3
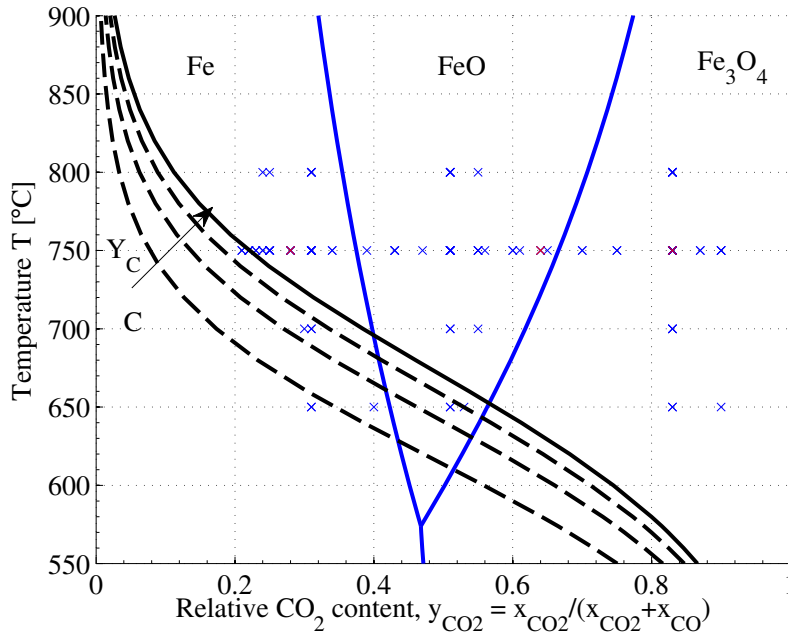
Figure 3.3.: Visualisation of the experimental parameter range covered in the study. The range of Y_C is not shown. The highlighted points correspond to the experiment shown in Fig. 3.2. An explanation of the diagram is given in Sec. 2.4.

is the third parameter $Y_C = x_{CO} + x_{CO_2}$ describing the overall carbon content of the gas mixture. This parameter ranged from $0.17 \ldots 0.42$ ($Fe_3O_4 \rightarrow FeO$), $0.17 \ldots 0.83$ ($FeO \rightarrow Fe$), $0.25 \ldots 0.83$ ($Fe \rightarrow FeO$) and $0.42 \ldots 0.83$ ($FeO \rightarrow Fe_3O_4$). These ranges were limited by one or more of the following factors: time allowed for a measurement, avoidance of coke formation, range of the MFCs, and supplying a minimum N_2 gas flow as seal/purge gas for the scale chamber.

As can be seen in Fig. 3.1 the TGA equipment unfortunately offered no possibility to generate $H_2/H_2O/N_2$ gas mixtures. Neither stepwise reductions of the material to Fe, nor oxidations could therefore be conducted in the system described by reaction three and four of Tab. 2.1. However, complete reductions with H_2/N_2 gas mixtures could be performed and were compared to reductions by CO/N_2 to extrapolate towards $H_2/H_2O/N_2$ kinetics. This will be discussed more in-depth in Sec. 3.3.1 on p. 47.

A blank run was conducted with each new gas composition or temperature setting. This blank curve was subtracted from the measurement data of subsequent experiments. This was necessary as the scale was sensitive enough to register the change in buoyancy of the sample holder in the varying gas atmospheres of an experiment.

3.1.3. Results

A typical transient of the sample mass during a reduction was presented in Fig. 3.2. Three distinct steps are recognisable, corresponding to the three reaction steps necessary to reduce Fe_2O_3 to Fe. The first reduction step, Fe_2O_3 to Fe_3O_4, was not analysed, due to its irrelevance to the CWGSR. At $t = 30\,min$ the gas composition is changed to trigger the reduction to FeO. The sample mass decreased again, as oxygen was released to the gas phase. The relative mass at which the sample stops in the state of FeO varies slightly, due to the oxidation range in which FeO exists and the applied gas composition (see Sec. 2.3). The reduction of FeO always starts with a small step – a fast, small and distinct mass loss – before displaying its characteristic form described later. The step could be interpreted as the remaining reduction in the FeO range or the reduction of other substances in the sample. However, the size of the step could not be correlated to the gas composition applied in the previous reduction step, although it is of the same magnitude as the predicted reduction of CeO_2 to Ce_2O_3 in Sec. 2.1.2.

The reproducibility of the TGA results was good. One experiment, the reduction of Fe_3O_4 to FeO in $y_{CO_2} = 0.51$, $Y_C = 0.17$ at $750\,°C$ was repeated seven times. All results are shown in Fig. 3.4. The measurement noise during an experiment is much smaller than the deviation from one experiment to the other. This indicates that the actual weighing process of the sample during an experiment is an error source that can be neglected. Possible sources of the deviations between the experimental results are: a) setting of the gas concentrations by the gas supply; b) inhomogeneities in the employed sample material can have a large effect on the composition of the small sample used in an experiment; c) changes in the environment of the TGA between the blank and measurement run.

The reduction of FeO is about an order of magnitude slower than the reduction of Fe_3O_4 as shown in the examples of Fig. 3.5 and 3.6. The first diagram shows a range of reaction times of $2 \ldots 10\,min$ at $750\,°C$ and varying gas compositions. The change of temperature to 650 or $800\,°C$ did not lead to more extreme cases in the employed parameter space. Visible is the correlation between lower y_{CO_2} and reaction rate, as well as high Y_C and reaction rate. The steady state level of the sample mass at the end of the experiment, which is a measure for the total conversion rate, correlates only with y_{CO_2}. This is due to the existence of a continuum of oxidation states of FeO, depending on the location in the Baur Glaessner diagram; see Sec. 2.3. The curves show a small lag phase which might be due to non ideal switching of the gas phase composition.
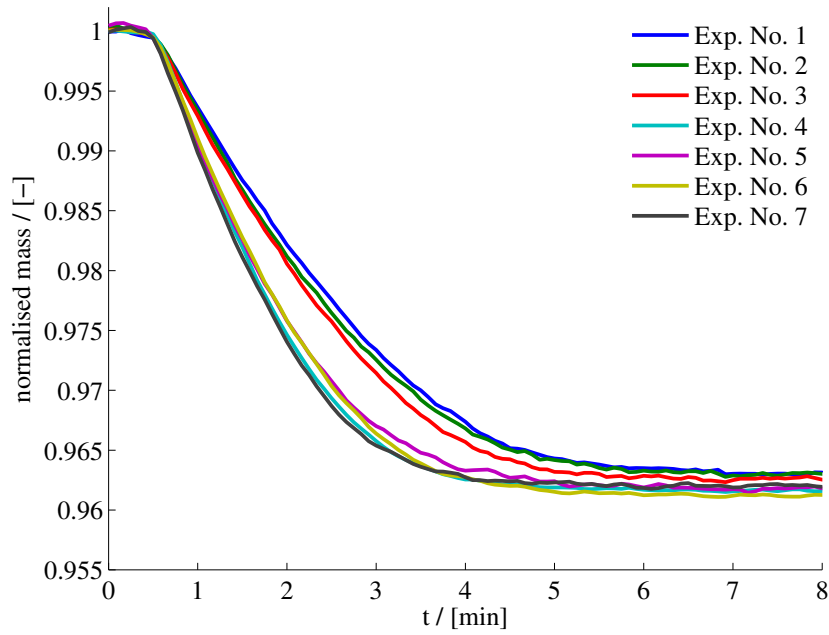
Figure 3.4.: Repeatability check of TGA experiments. Shown are Fe_3O_4 reductions to FeO at $y_{CO_2} = 0.51$, $Y_C = 0.17$ and $650\,°C$ with different samples from the same batch.
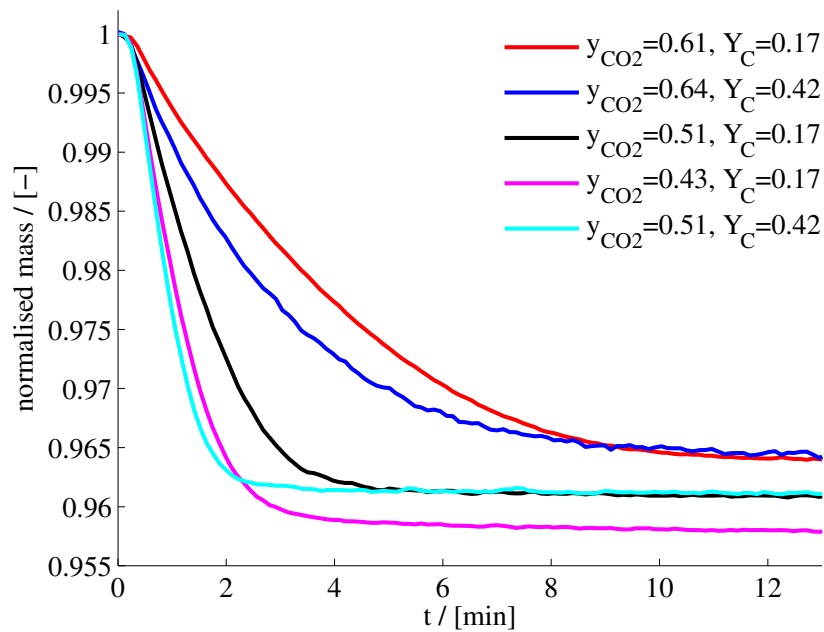
Figure 3.5.: Typical spread of TGA measurements for the reduction of Fe_3O_4 at $750\,°C$ in $CO/CO_2/N_2$.
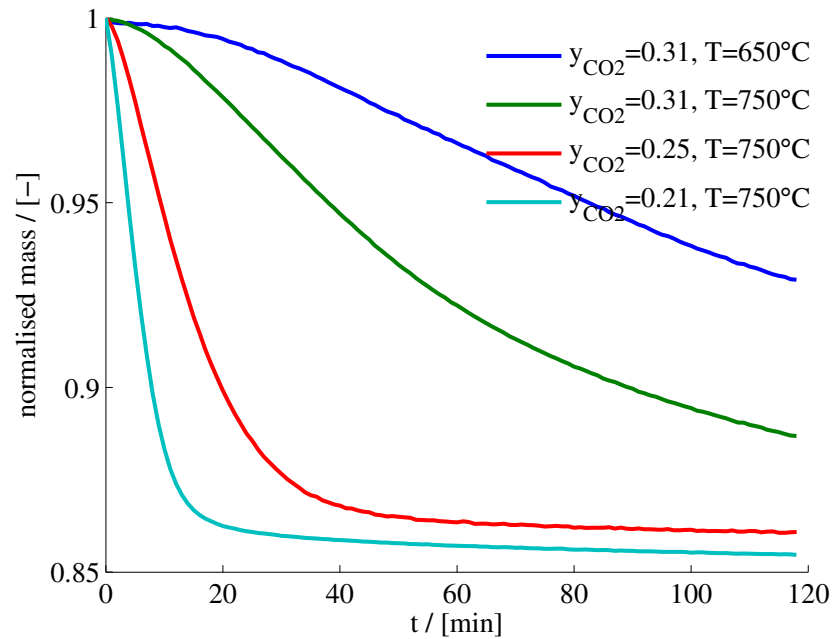
Figure 3.6.: Typical spread of TGA measurements for the reduction of FeO at $Y_C = 0.67$ in $CO/CO_2/N_2$. Note the larger range of the ordinate to accommodate for the larger weight loss during this reduction compared to the reduction of Fe_3O_4 (see Fig. 3.4 and 3.5).

Fig. 3.6 shows a range of FeO reduction experiments. The reaction rate correlates again with y_{CO_2}, Y_C and T. The most striking feature is the sigmoid nature of the curves of slower reductions. This means that reactions with constant low external driving forces start out slow, increase their rate during reaction and slow down towards the equilibrium. The smaller the total reaction time, i. e. the higher the driving forces, the smaller the first shoulder of the sigmoid curve becomes. This trend converts the sigmoid shape into the common one of exponential decline. With high driving forces the highest reaction rates are measured at the start of the reaction.

3.1.4. Discussion

A possible interpretation involves the notion of crystal growth and fault points in a lattice as their "seeds". Each particle of the samples subjected to the TGA had to endure three complete phase transitions as they were reduced from Fe_3O_4 to Fe. Such a transition of an at least partly crystalline solid does not happen homogeneously across the whole particle. It starts at fault points in the lattice and grows from there into the surrounding material. If only a small number
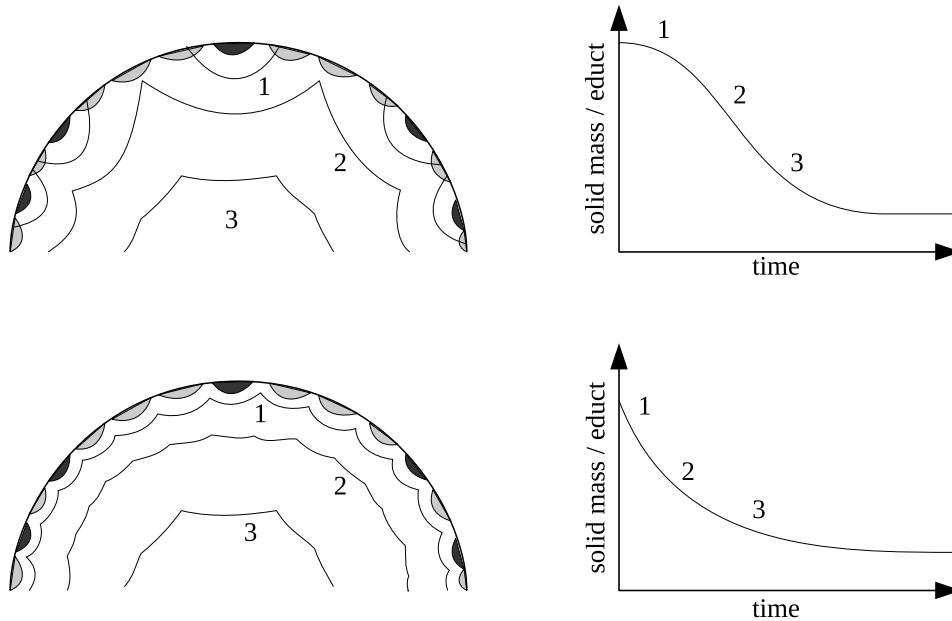
Figure 3.7.: Schematic representation of the FeO reduction mechanism. The numbers 1 to 3 represent progress of the reaction in the particle (left) and points in time (right). The reaction starts in high (dark) and low (light grey) energy lattice fault points. Depending on the strength of the driving forces (y_{CO_2}, Y_C, T) and the utilisation of only high energy or more lattice fault points, the apparent kinetics change from being similar to be typical of the shrinking core model (SCM).

of highly energetic fault points act as those growth seeds, the area where reaction occurs, is small in the beginning, grows to a maximum during the reaction and decreases again as the reacting surfaces merge – compare to Fig. 3.7. The behaviour is different, if the external driving forces are large and reactions also starts at lower energetic, i.e. more fault points in the lattice. The reaction surface is large in the beginning and will only decrease as the reaction continues. The surfaces merge early on and move through the remaining particle. The first case describes a reaction kinetic similar to the one described by and known as Avrami (or Johnson-Mehl-Avrami-Kolmogorov, JMAK) and the second a classic shrinking core model (SCM). Both models will be tested for their suitability in Sec. 3.2 and 3.3.

The step wise oxidation of Fe to Fe_3O_4 in a CO/CO_2 atmosphere shows a similar behaviour to the reduction experiments described above: A slow transition from Fe to FeO, with slightly varying degrees of steady-state oxidation in FeO. The oxidation to Fe_3O_4 is again fast, mirroring the behaviour of the reductions.

The experimental equipment did not allow the stepwise TGA using steam. It was assumed, that the reactions of the iron oxide material in H_2/H_2O show the same qualitative behaviour as

j = 1:	$3\ FeO_{4/3} + CO$	$\rightleftarrows$	$3\ FeO + CO_2$
j = 2:	$FeO + CO$	$\rightleftarrows$	$Fe + CO_2$
j = 3:	$3\ FeO_{4/3} + H_2$	$\rightleftarrows$	$3\ FeO + H_2O$
j = 4:	$FeO + H_2$	$\rightleftarrows$	$Fe + H_2O$

Table 3.1.: Gas-solid reactions described by the TGA model.

in CO/CO_2 mixtures. Complete reductions to Fe in H_2/N_2 were an order of magnitude faster than in CO/N_2.

3.2. Modelling

This section explains the formulation of the model used to simulate the TGA experiments and discusses the different possibilities to model the reaction kinetics.

3.2.1. TGA Experiments

The purpose of this model is to simulate the mass of the sample over time. It is based on a molar balance of the solid species. A quasi-homogeneous reactor without mass transport limitations is assumed, as well as constant temperature and gas phase composition.

The change of the molar amount of solid species i during reaction j (only two solid species are present during any TGA experiment) is described in Eq. 3.1:

$$\frac{dn_i^s}{dt} = v_{ij}^s \cdot m_0 \cdot r_j(x, T) \tag{3.1}$$

$$v_{ij}^s = \begin{array}{ccc} Fe & FeO & FeO_{4/3} \\ \begin{pmatrix} 0 & 3 & -3 \\ 1 & -1 & 0 \\ 0 & 3 & -3 \\ 1 & -1 & 0 \end{pmatrix} \end{array} \tag{3.2}$$

with the stoichiometric factor for the solid species v_{ij}^s, the weight of the sample at the start of the TGA ("weigh in", Fe_2O_3) m_0 and the reaction source term r_j in $mol_j/(g_{weigh\ in}\ s)$. Reactions are listed in Tab. 3.1.

New quantities are introduced to reshape the the balance: the solid fraction[2] of species i, x_i^s, the total number of iron atoms in the sample (associated with any species), $n_{\text{Fe,t}}^s$, and the concentration or initial density of iron atoms, $c_{\text{Fe,t}}^s$, in $\text{mol}_{\text{Fe}}/\text{g}_{\text{weigh in}}$:

$$x_i^s = n_i^s / n_{\text{Fe,t}}^s \tag{3.3}$$

$$c_{\text{Fe,t}}^s = n_{\text{Fe,t}}^s / m_0 \tag{3.4}$$

The molar balance, Eq. 3.1, can now be reformulated in terms of x_i^s, which will be later used for the kinetic expressions. To model the mass of the solid m^s, it is considered that only oxygen is leaving or entering the solid:

$$\frac{dx_i^s}{dt} = v_{ij}^s \cdot \frac{1}{c_{\text{Fe,t}}^s} \cdot r_j(x,T)\,, \qquad x_i^s(t=0) = 1 \tag{3.5}$$

$$\frac{dm^s}{dt} = v_{\text{O}j} \cdot M_\text{O} \cdot m_0 \cdot r_j(x,T)\,, \qquad v_{\text{O}j} = -1 \,\forall j\,, \quad m^s(t=0) = m_0^s \tag{3.6}$$

with the stoichiometric coefficient $v_{\text{O}j}$ and the molar mass of the oxygen atom $M_\text{O} \approx 16\,\text{g}_\text{O}/\text{mol}_\text{O}$.

Whether the model is best solved analytically or numerically strongly depends on the chemical reaction rate expression r_j. Different options for r_j formulations are discussed in the next section.

3.2.2. Reaction Kinetics

There are numerous gas-solid reaction models, which can be applied to the present system. Superb overviews and detailed discussions are already available in the literature, e. g. by Levenspiel [56] and Szekely et al. [95]. Therefore this section will only give a brief discussion of the various models, which usually fall somewhere in the spectrum from the simple, phenomenological, numerical robust and flexible to the complex, physically motivated, and expensive to solve. The discussed models are illustrated in Tab. 3.2 and 3.3 along with their rate expressions.

The **Shrinking Core Model (SCM)** is a standard kinetic model in solid phase reaction engineering. Conversion is taking place on a thin shell, which is moving inward through the solid particle as the material is converted.

---

[2]x_i^s is called solid fraction to avoid the term molar fraction, which might imply a homogeneous mixture.

Name	Rate Expressions	Illustration
Shrinking Core Model (SCM)	reaction controlled $$r = k \cdot f(c^g) \cdot (x^s)^{2/3}$$ diffusion controlled $$r = k \cdot f(c^g) \cdot \frac{(x^s)^{1/3}}{1-(x^s)^{1/3}}$$	
Uniform Conversion Model (UCM)	$$r = k \cdot f(c^g) \cdot (x^s)^n$$	
Avrami Model (JMAK)	$$r = k \cdot f(c^g) \cdot \frac{x^s \cdot (-\ln(x^s))^n}{1-n}$$	
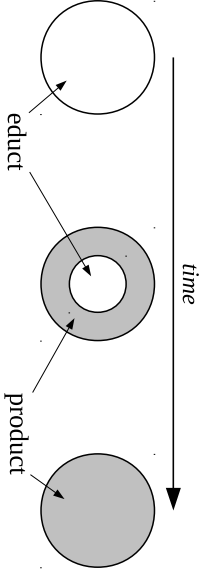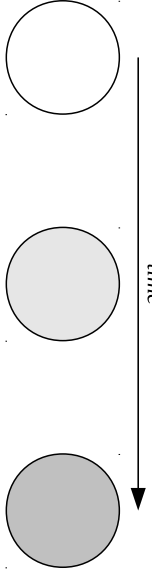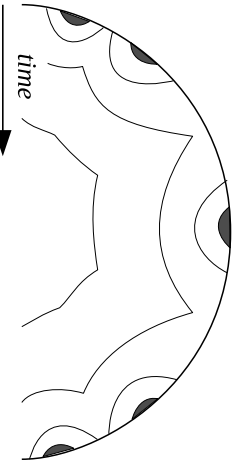
Table 3.2.: Gas-solid reaction models discussed for the iron oxide material oxidation and reduction. Part 1/2.

Name	Rate Expressions	Illustration
Grainy Pellet Model (GPM)	$$r = \frac{1}{4/3\,\pi P^3_{pellet}\,\rho_{pellet}} \cdot \int_0^{P_{pellet}} (1-\varepsilon)\,4\pi P^2\, r_{grain}\,\mathrm{d}P$$ $$r_{grain}(P) = k_{grain} \cdot f(c^g_{grain}) \cdot (x^s_{grain})^{2/3}$$ $$0 = -\varepsilon \frac{1}{P^2}\frac{\partial}{\partial P}\left(P^2 D_i \frac{\partial x^g_i}{\partial P}\right) + (1-\varepsilon) v_i\, r_{grain}$$ $$\mathrm{BC}: \left.\frac{\partial x^g_i}{\partial P}\right|_{P=0} = 0$$ $$\left. x^g_{grain}\right|_{P=P_{pellet}} = x^g_{TGA}$$ $$\frac{\partial x^s_{grain}(P)}{\partial t} = \frac{1}{\rho_{Fe_2O_3}\, c^s_{Fe,t}} v_i\, r_{grain}$$	educt product
Changing Voidage Model (CVM)	$$\varepsilon(P) = \varepsilon_0 + (1-\varepsilon_0)(1-x_{grain}(P))\left(\frac{v_{educt}-v_{product}}{v_{educt}+v_{inert}}\right)$$	

Table 3.3.: Gas-solid reaction models discussed for the iron oxide material oxidation and reduction. Part 2/2.

3. Reaction Kinetics

Without mass transport limitation, the conversion rate of the particle is controlled by the surface reaction kinetics. This is called the **reaction controlled** subtype of this kinetic. If a product layer is built up while the reaction shell is moving inwards, the macro kinetics can be controlled by the diffusion rates of gaseous educts and products. This **diffusion controlled** subtype is another extreme of the SCM. Cases of the SCM with mixed control show a behaviour within the limits set by diffusion and reaction controlled regimes.

Although the model is derived with a very specific setting of gas and solid in mind, Levenspiel [56] notes that many possible reaction mechanisms and types of solid (porous & non-porous), with or without gaseous reactant, show the same behaviour and can therefore be described by the SCM.

Since the macroparticles in iron ore reduction "[do] not appreciably change in size" [57] the shrinking core model for spherical particles of unchanging size was selected in this work.

The **Uniform Conversion Model (UCM)** does not take any mass transport or locally confined reaction zones into account. All parts of the particle are converted at the same time to the same extent. The rate expression is similar to a power law as used in gas reactions. Albeit the latter can be rigorously derived from thermodynamics, this is not the case for the UCM.

The UCM is a phenomenological model which can describe the behaviour of many underlying reaction mechanisms. Many extremes of the other models can be cast into the form of the UCM.

The original idea of the **Avrami Model** (or Johnson-Mehl-Avrami-Kolmogorov, **JMAK**, applied to Fe_3O_4 reduction by e. g. Lorente et al. [60]) is one of a phase change model. As such, it does not necessarily model reaction and mass transport of the reactants. The solid phase is converted into a new phase (the product) around nuclei or already present parts of the new phase (or product). The conversion boundary is spreading outward from the nuclei, only stopping when the edge of the particle is encountered or the boundary merges with another.

The Avrami model can produce S-shaped conversion-time curves. Due to its structure and an initial reaction rate of exactly Null, the model can give computational problems. Solving a dynamic model over time via numerical integration might lead to unexpected results as the Avrami reaction might never start; or only start because of numerical errors.

The **Grainy Pellet Model (GPM)** [93, 94] is a representation of a porous solid (the pellet, with the radius R_{pellet}) consisting of many, equally sized (r_{grain}) non-porous grains. Each is described by the SCM and is in a different state x^s_{grain} depending on its location R in the pellet.

42

Gaseous reactants permeate the pellet through the voidage ε with the diffusivity D_i between the grains. The grains, and therefore the pellet voidage, do not change in size. Estimations for these parameters are given in Sec. A.3.

Since a new dimension is introduced into the model, the rigorous computation becomes much more expensive than with the models described above. But the model formulation is resembling the actual physical system of the iron oxidation/reduction much better than previous models. The GPM can in some mixed control regime show a behaviour which qualitatively differs from the SCM and UCM [56].

The **Changing Voidage Model (CVM)** [31,56,79] is an extension of the GPM. The voidage ε is now allowed to change as the grains can swell or shrink. The diffusional resistance for the gaseous educts moving between the grains therefore also changes.

This model is the most complex of the here presented ones, as well as the one most closely resembling the target system, as iron oxide changes in molar volume v when converted between different oxidation states (see Sec. A.4) and it can be assumed that the microparticles also change in size.

Due to its complexity, the model can show a wide range of behaviours, including S-shaped conversion time curves. However, many of the model parameters like changes in molar volume should not be adjusted for the model to generate a better fit to experiments. These parameters are given by physical properties of the material. The spectrum of reproducible behaviours is thus narrowed, if the "bottom up" philosophy in deriving the model is to be honoured.

Most derivations of gas-solid kinetics use the molar gas concentration of the educt, c^g, to denote the **influence of the gas phase** exerted on the reaction rate – if the educt gas concentration c^g is zero, the reaction stops. In reaction systems with the equilibrium strongly on the product side, this gives acceptable results. In the reaction system discussed in this work, however, the reaction rate should be zero if the gas mixture is in equilibrium with the solid phase. Referring to the Baur Glaessner diagram of Sec. 2.4, reactions should stop if the gas phase is in the same region as the solid phase. The more the gas mixture differs from one of the boundaries in the equilibrium diagram, the higher the driving force and the faster the

3. Reaction Kinetics

reaction should occur. To quantify this, the gas driving force $(x_i^g - x_i^{g,eq})$ is introduced. Using the definitions in Eq. 2.3 to 2.5, this can be transformed into

$$f(x_i^g) = Y_C \left(y_{CO} - \frac{1}{1 + K_{j,\pm}(T)} \right) \qquad \text{for oxidation steps} \qquad (3.7)$$

$$f(x_i^g) = Y_C \left(\frac{1}{1 + K_{j,\pm}(T)} - y_{CO} \right) \qquad \text{for reduction steps} \qquad (3.8)$$

in CO/CO$_2$ systems, with $K_{j,\pm}(T)$ being the equilibrium constant of the corresponding reaction.

The previously mentioned models did not take the reaction rate **dependency on the temperature** into account. The Arrhenius equation for the reaction rate coefficient $k_{j,\pm}$ is used here in the following form:

$$k_{j,\pm}(T) = k_{j,\pm}^{\otimes} \exp \left(-\frac{E_{j,\pm}}{R} \left(\frac{1}{T} - \frac{1}{T^{\otimes}} \right) \right) \qquad \text{with } T^{\otimes} = 1073\,\text{K} \qquad (3.9)$$

with the pre-exponential factor $k_{j,\pm}^{\otimes}$, the activation energy $E_{j,\pm}$, the universal gas constant R and a standard temperature $T^{\otimes}$. In this formulation, sometimes referred to as temperature centring [104], $k_{j,\pm}^{\otimes}$ is based on the standard temperature of the CWGSR and not on an infinite temperature. This will tighten the confidence intervals for the fitted values for $k_{j,\pm}^{\otimes}$ [81].

These extensions of the models increase the number of fitted model parameters to four $(k^{\otimes}, E, m, n$; an example is given in Eq. 3.17), resp. three for the SCM, where n is fixed to ⅔. The GPM and CVM have more model parameters, but these should be determined a priori from physical parameters of the participating species.

To **summarise**, a trend to more complexity and more detailed representations of possible reaction mechanisms is observed in the range of presented models. But a problem becomes apparent when in view of the intended future application, the CWGSR: full reduction or oxidation of the iron material will rather be the exception than the normal operating mode. Many assumptions (e. g. completely oxidised pellet at $t = 0$) in the model derivations are therefore not met. Furthermore, the interpretation of fitted kinetic parameters through their mechanistic models can be problematic due to their ability to simulate behaviour originating from considerably different reaction mechanism [56]. It can therefore be concluded that the form and source of the model is a secondary objective.

The same can be argued for the qualitative behaviour of the models. Some models can show the experimentally observed S-curves, while some do not. As long as there is no indication, that this property of the reaction kinetics is important for the behaviour of the reactor, it should not determine the model as long as a quantitatively reasonable fit over the whole range of experimental conditions is achieved.

The two main properties a kinetic model must fulfill to be useful for the purpose of reactor analysis are (1) consistency with the thermodynamic equilibria and (2) agreement with the experimental TGA data. The former is ensured by the formulation of the gas driving force. The latter can be achieved via the quantitative comparison of the model fit in the next section.

3.3. Model Discrimination

The selection of a kinetic model was performed as a two stage procedure. In the first stage, all the models were implemented and fitted to a small experimental data set for preselection. In the second stage, the two most promising models were fitted to the whole experimental data set and statistically evaluated.

From a mathematical point of view, the reaction controlled SCM is a special case of the UCM, with a fixed exponent $n = 2/3$ for x^s. This one lacking degree of freedom led to the inability to fit multiple experiments with a single parameter set. The SCM was therefore discarded in favour of the UCM.

Similarly, the GPM also lacked flexibility and could not simulate the wide spectrum of experimental data generated by the TGA of one reaction with one parameter set. The additional parameters used by the model, pellet porosity and diffusion coefficients, ε and D_i, were estimated separately (Sec. 2.2.1 and A.3) and were not subject of the fitting, as this would disregard the physical motivation of the model.

The CVM, while being able to simulate S-shaped TGA curves, could clearly not produce the sometimes very pronounced sigmoid shape of the experiments. Again, the additional parameters like molar volumes and diffusion coefficients were determined a priori (Sec. A.4). Fits that were similar to the quality of the ones with the Avrami model could only be produced by utilising unrealistic diffusion coefficients and impossible changes in molar volume.

This preselection process leaves the UCM and Avrami model, which will both be fitted against the whole experimental data set in the next section.

3.3.1. Parameter Estimation

To estimate model parameters, all TGA data of the four reactions ($Fe_3O_4 \rightarrow FeO$, $FeO \rightarrow Fe$, $Fe \rightarrow FeO$ and $FeO \rightarrow Fe_3O_4$, all in $CO/CO_2/N_2$ atmosphere) were collected in four data sets. These data sets consisted of 10 to 20 TGA measurements each. For each reaction, i. e. data set, a TGA model with UCM and a model with Avrami kinetics was implemented. This resulted in eight fitted parameter sets, two for each reaction. The fitting was done via a least squares optimisation:

$$\min_{X} \quad \sum_{\substack{\text{all TGA} \\ \text{measurements} \\ \text{of } j; + \text{ or } -}} \sum_{t} \left(\left(\frac{m_t^s}{m_{t=0}^s} \right)_{\text{exp}} - \left(\frac{m_t^s}{m_{t=0}^s} \right)_{\text{model}} \right)^2 \qquad \text{with } X = [k^{\otimes}, E, n, m]_{j, \pm}$$

$$\text{subject to eq. (3.6)} \tag{3.10}$$

To remove a bias caused by different initial sample weighs, all TGA measurements were normalised to their start weight. Another bias is introduced through the use of measurement with equal sampling frequency, yet different lengths. Long duration experiments have more data points than short measurements do. The fitted parameters should therefore describe slow reactions at low driving forces in a better quality. However this is offset again, because fast reactions with high driving forces were measured more often. Resampling the measurements by numerical interpolation of the original data to have a constant number of data points per measurement might solve avoid this bias, but was not done in this work.

The optimisation parameters, X, have absolute numerical values differing up to eight orders of magnitude. A normalisation was mandatory for stable optimisation. The optimisation was done with a Gauß-Newton algorithm implemented in the Matlab 2008[3] function lsqnonlin().

To increase robustness of the fitting process, the experiments were designed to allow for the successive optimisation of no more than two parameters simultaneously (see Sec. 3.1.2): In a first step a lumped model parameter k'' and the model parameter n were fitted to a subset of experiments with no variation of experimental conditions. In a second step, variation of experimental gas conditions were used to fit m and a new lumped parameter k', while the previously estimated parameter n was used but kept constant. After the next step of introducing data sets obtained at different temperatures and determining $k^{\otimes}$ and E, all model parameters were fitted simultaneously to all experiments, using the previously determined values as starting values.

---

[3]Numerical computing environment by The MathWorks, Inc., Natick, Massachusetts, USA.

Estimation of H$_2$/H$_2$O Parameters

Due to technical limitations, the TGA could not be operated with steam as reaction educt (see Sec. 3.1). Without data from reactions with varying H$_2$/H$_2$O ratio, parameters for these reactions could not be fitted directly; They were extrapolated from CO/CO$_2$ data.

It was assumed, that parameters E, m and n are identical to their CO/CO$_2$ reaction counterparts. These assumptions have been made before in the literature (e. g. Takenaka et al. [96], with evidence for the soundness of this assumption documented by Tsay et al. [99] and Moon et al. [67], and further support in the review by Pineau et al. [76]). A constant factor was applied to all $k^\otimes$ values to account for the faster reaction rates associated with H$_2$/H$_2$O mixtures.

TGA experiments with pure H$_2$ ($y_{H_2O} = 0$) could be conducted. The CO/CO$_2$ model was then fitted to the H$_2$ data varying only $k^\otimes$. The kinetic parameters used for the reactions with H$_2$/H$_2$O are therefore the same as the one with CO/CO$_2$, except for the frequency factor. Although the kinetic parameters obtained here are extrapolated and have to be used with caution, they can be assumed to adequately approximate the real parameters, given the experimental circumstances.

3.3.2. Confidence Intervals

The estimation of confidence intervals from least squares fits of nonlinear dynamic models against a collection of data sets over time is not standardised. The method used here follows closely the arguments given by Rawlings and Ekerdt [81] and Bard [5]. It is illustrated and extended here for the sake of clarity and the application to the experimental data obtained in this work.

The region of confidence around a fitted pair of parameters (e. g. X_1^* and X_2^*) can be visualised as the area inside an ellipse centred at X^* as sketched in Fig. 3.8. The ellipse is described by a covariance matrix derived from the data and the fit. Usually individual confidence intervals are given to each parameter of a parameter set. This corresponds to a box, which circumscribes the ellipse and thus overestimates the confidence region. An ellipse can be described by Eq. 3.11 and the corresponding confidence box by Eq. 3.12.

$$X^T A X = b \tag{3.11}$$

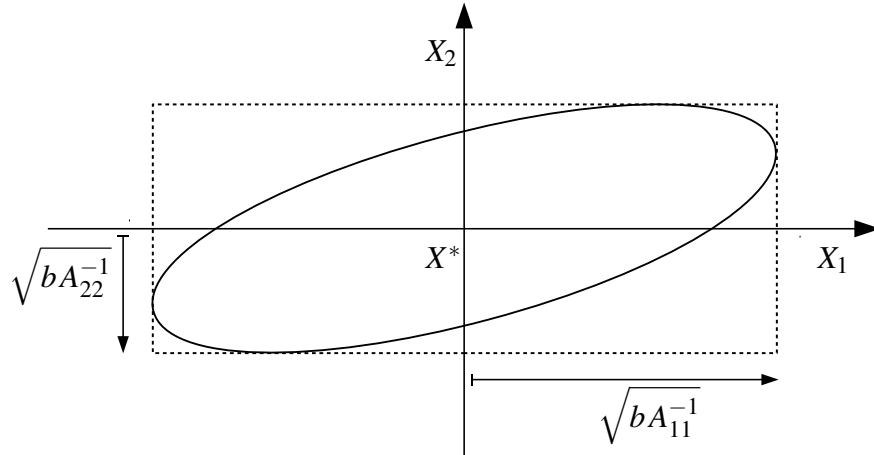$$\begin{bmatrix} X_1^* \pm \sqrt{b A_{11}^{-1}} \\ X_2^* \pm \sqrt{b A_{22}^{-1}} \end{bmatrix} \tag{3.12}$$

Figure 3.8.: The geometry of an ellipse $X^T A X = b$ as confidence region around a parameter set X^*.

When parameters are computed via a least squares optimisation of a nonlinear model, the description of all parameter sets inside the confidence interval can be formulated as Eq. 3.13 [81]. Its form is analogous to the ellipse described in Eq. 3.11.

$$(X - X^*)^T \cdot H_{X=X^*} \cdot (X - X^*) \leq 2 \cdot s^2 \cdot n_p \cdot F(n_p, n_d - n_p, \alpha) \tag{3.13}$$

with the (true/fitted) parameter set (X^*) X, the variance s^2, the Fisher probability function F, the number of model parameters n_p, the number of data points n_d, the confidence level α, and the Hessian H of the objective function at X^*.

H can be approximated as $H \approx 2J^T J$ with the Jacobian J, as is done in the Gauß-Newton optimisation algorithm for solving least squares problems. In this application, the Jacobian can also be interpreted as the sensitivity of the model fit against the variation of parameters.

The confidence interval, or box for each parameter of the set can therefore be computed with Eq. 3.14, derived from Eqs. 3.11 through 3.13.

$$\text{box}_i = \sqrt{(2 \cdot s^2 \cdot n_p \cdot F(n_p, n_d - n_p, \alpha)) \cdot (2J^T J)^{-1}} \tag{3.14}$$

On Estimating The Variance

If the variance does not change from data point to data point, the variance can be estimated from
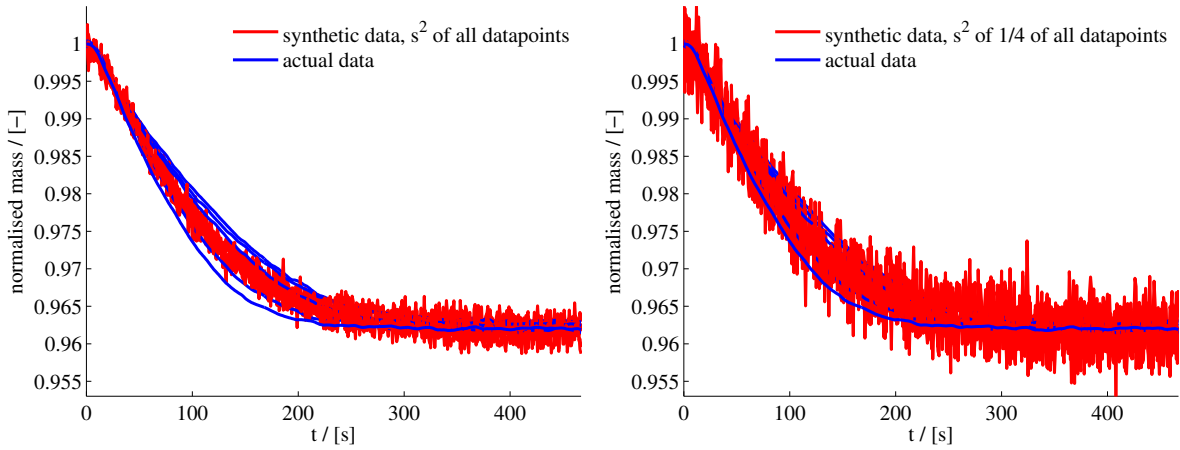
$$s^2 = \frac{RSS(X^*)}{n_d - n_p} \tag{3.15}$$

Figure 3.9.: Visualisation of the estimated data variance by generating synthetic data from the model and noise with s^2. Left: Using all data points for s^2 estimation. Right: Using only the "worst quarter" by deviation, thus better covering the data's spread. The actual data plotted are of Fe_3O_4 reductions at $y_{CO_2} = 0.52, Y_C = 0.17, T = 750\,°C$.

with $RSS(X^*)$ as the residual sum of squares at optimum.

Problems arise with a variance changing over time or data points, as is the case e. g. with the TGA data: All data points at $t = 0\,$s have the same value of 1 as all data sets have been normalised w. r. t. to their initial values. Additionally, they have very similar values at the end of the data sets at steady state, since the reactions are limited by thermodynamic constraints. It is between those two boundaries where the variance is almost zero, that the data sets differ significantly because of differing reaction rates.

Another problem is the prerequisite for Eq. (3.15) that all n_d data points are independent from each other. For the data points taken in a time series of a TGA experiment this is not the case. They do depend on the previous states of the system, which are represented by the previous measurements.

Therefore, if the estimation in Eq. 3.15 is applied to the data, the variance is underestimated as is visualised in Fig. 3.9. To estimate a more representative variance, only the quarter of all data points was used, with the highest deviation between fitted model and measurement (Eq. 3.15). This typically selected the second quarter of measurements in the time series.

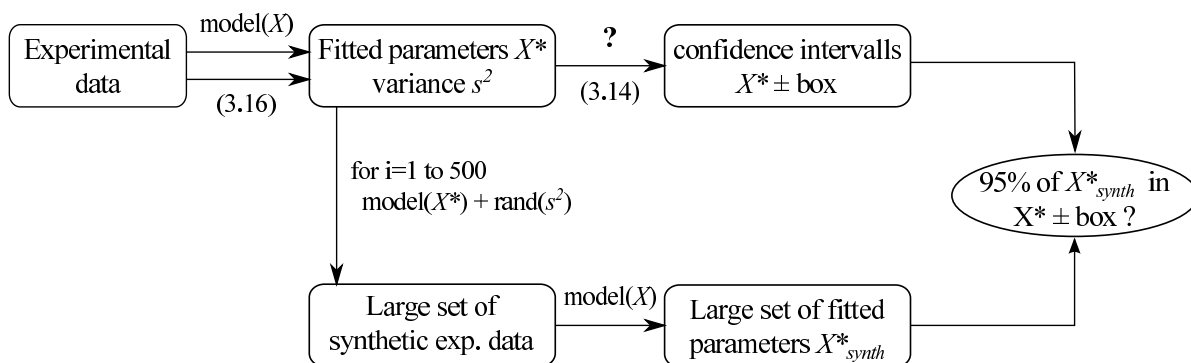$$s^2 = \frac{RSS_{\text{top25\%}}(X^*)}{1/4 n_d - n_p} \tag{3.16}$$

Figure 3.10.: The confidence intervals calculated from Eq. 3.14 might not be correct, because the applied kinetic model is strongly non-linear. The computed confidence intervals were therefore tested via the Monte Carlo method.

Testing The Estimated Confidence Intervals

During the process of estimating the confidence intervals, a number of approximations were applied. A statistical method for calculating confidence intervals for parameters of linear models fitted to independent data points was expanded for nonlinear models and non-independent data points. The models were effectively linearised at X^* for the determination of the Jacobian. Furthermore, the Gauß-Newton approximation of the Hessian was used.

To test the computed confidence intervals, Rawlings [81] proposes the application of a Monte Carlo study for each parameter set. This method generates a large number of synthetic data sets from fitted kinetic parameters and tests, whether new kinetic parameters obtained from these synthetic data sets are within the original confidence intervals. The procedure includes the following steps:

1. Generate a synthetic data set from the model with original, fitted parameters and Gaussian noise with variance s^2.

2. Fit a new parameter set to that data set by least squares optimisation.

3. Repeat steps 1 & 2 a large number of times, e. g. 500.

4. Test, whether more than 95 % of the new fitted parameter sets from step 2 are within the $\alpha = 0.95$ confidence interval of the original fit (see Eq. 3.13). In a linear model with independent measurements this is always the case.

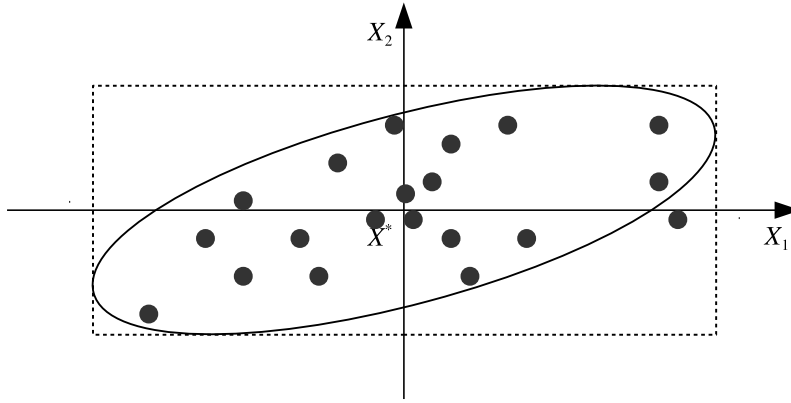This Monte Carlo study is also illustrated in in Fig. 3.10 and 3.11.

Figure 3.11.: Example for Monte Carlo study with 20 synthetic data sets generated from parameter set X^* with 95 % confidence interval. Parameter sets generated from synthetic data sets are marked by dots. In this illustration the study indicates that the stated confidence interval is not underestimated because no less than 95 % of generated parameter sets are in the original confidence ellipse.

All given parameter sets passed the Monte Carlos study. Approximately 95 % of the corresponding synthetic parameter sets were within the 95 % confidence ellipse and much more inside the (larger) rectangular confidence box. An exemplary visualisation is done for the Avrami model fit of the reduction of Fe_3O_4 to FeO in Fig. 3.12. The estimated confidence intervals are therefore not impaired by the simplifications used in calculating them.

3.3.3. Results

The parameters for the two kinetic models, Avrami and UCM, are given in Tab. 3.5. As presented, they are to be used for reaction 1 and 2 from Tab. 3.1, that is for the reduction and oxidation of the iron material with CO/CO_2. As discussed on page 47, the parameters for the reactions with H_2/H_2O are assumed to be the same as for the CO/CO_2 redox pair, except for $k^{\otimes}$: When using the Avrami model the pre-exponential factors are multiplied by 6.06 ($k^{\otimes}_{3/4,\pm} = 6.06\,k^{\otimes}_{1/2,\pm}$). In case of the UCM, the factor is 6.48 ($k^{\otimes}_{3/4,\pm} = 6.48\,k^{\otimes}_{1/2,\pm}$).

The residuals of the parameter fits as calculated by the `lsqnonlin` algorithm, i. e. the sum of the squared deviations between model and experiment, are listed in Tab. 3.4. They can be used to compare the two model fit qualities to each other, since both models have the same number of parameters.

The parameters are to be used with the kinetic models presented in Sec. 3.2.2. Complete examples of the kinetic expressions are given in Eqs. 3.17 and 3.18. The former describes the forward (reduction, "+") and backward (oxidation, "−") direction of reaction 1 with the UCM.
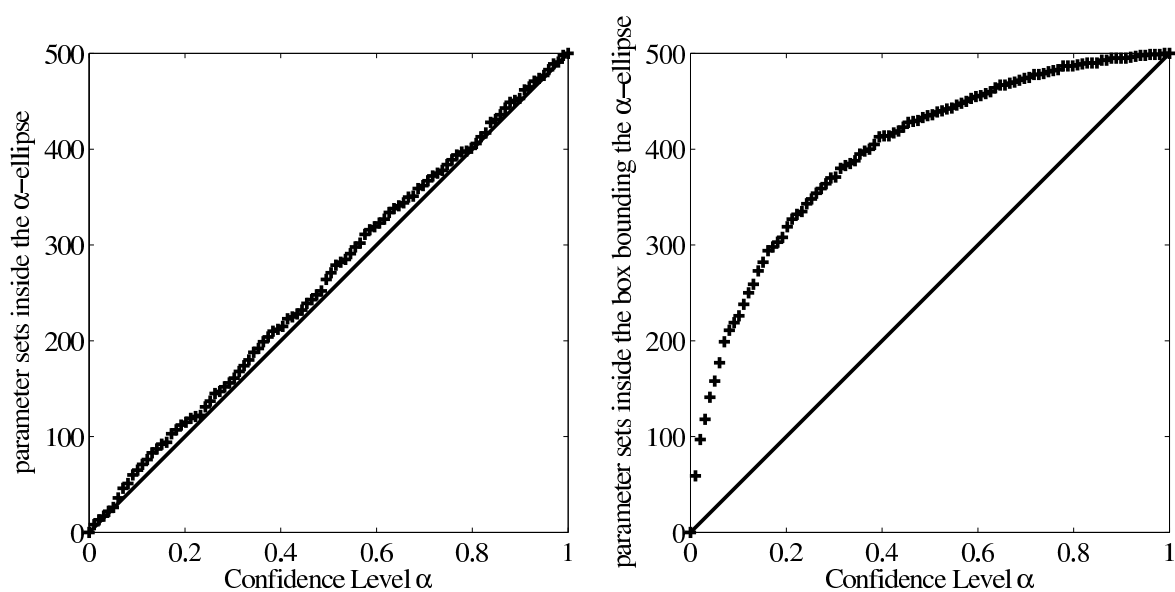
Figure 3.12.: Monte Carlo study of estimated confidence intervals around kinetic parameter sets. Plotted in crosses is the number of parameters sets obtained by the Monte Carlo method that are within the confidence ellipse/interval at level α given in the original estimation. E. g. about 110 of 500 kinetic parameter sets from the MC study are within the confidence small ellipse at level $\alpha = 0.2$. About 477 of 500 kinetic parameters set form the MC study are within the much wider ellipse at $\alpha = 0.95$. The given confidence interval is not underestimated. The results for the evaluation of the ellipse's bounding box described by individual confidence interval per parameter (as given in Tab. 3.5) is more favourable, because the box is larger (see Fig. 3.8).

Eq. 3.18 describes both directions of reaction 4 with the Avrami model. The formulation of all other expressions follows along the lines of these examples.

$$
r_1 =
\begin{cases}
k_{1,+} \exp\left(-\frac{E_{1,+}}{R}\left(\frac{1}{T}-\frac{1}{T^\otimes}\right)\right) \cdot \left(x^s_{Fe_3O_4}\right)^{n_{1,+}} \cdot Y_C\left(y_{CO}-\frac{1}{1+K_1^{eq}}\right)^{m_{1,+}} & \text{if } \frac{x_{CO_2}}{x_{CO}} < K_1^{eq}(T) \\[2ex]
k_{1,-} \exp\left(-\frac{E_{1,-}}{R}\left(\frac{1}{T}-\frac{1}{T^\otimes}\right)\right) \cdot \left(x^s_{FeO}\right)^{n_{1,-}} \cdot Y_C\left(\frac{1}{1+K_1^{eq}}-y_{CO}\right)^{m_{1,-}} & \text{if } \frac{x_{CO_2}}{x_{CO}} > K_1^{eq}(T)
\end{cases}
$$

(3.17)

$$
r_4 =
\begin{cases}
k_{4,+} \exp\left(-\frac{E_{4,+}}{R}\left(\frac{1}{T}-\frac{1}{T^\otimes}\right)\right) \cdot \frac{x^s_{FeO}(-\ln x^s_{FeO})^{n_{4,+}}}{1-n_{4,+}} \cdot Y_H\left(y_{H_2}-\frac{1}{1+K_4^{eq}}\right)^{m_{4,+}} & \text{if } \frac{x_{H_2O}}{x_{H_2}} < K_4^{eq}(T) \\[2ex]
k_{4,-} \exp\left(-\frac{E_{4,-}}{R}\left(\frac{1}{T}-\frac{1}{T^\otimes}\right)\right) \cdot \frac{x^s_{Fe}(-\ln x^s_{Fe})^{n_{4,-}}}{1-n_{4,-}} \cdot Y_H\left(\frac{1}{1+K_4^{eq}}-y_{H_2}\right)^{m_{4,-}} & \text{if } \frac{x_{H_2O}}{x_{H_2}} > K_4^{eq}(T)
\end{cases}
$$

(3.18)

	Avrami		UCM	
	+	−	+	−
$Fe_3O_4 \rightleftarrows FeO$	0.0205	0.742	0.0228	0.737
$FeO \rightleftarrows Fe$	5.94	1.35	5.50	1.34

Table 3.4.: The residuals of Eq. 3.10 given by Matlab's lsqnonlin() for the parameter fits given in Tab. 3.5.

		Avrami		UCM	
		Reduction →,+	Oxidation ←,−	Reduction →,+	Oxidation ←,−
$Fe_3O_4 \rightleftharpoons FeO$	$k^{\otimes}$ / 10^{-4} mol s⁻¹ g⁻¹	4.43 ± 6.9%	17.2 ±20.7%	3.52 ± 7.3%	28.7 ±23.6%
	E / 10^3 J mol⁻¹	5.51 ±73.5%	263 ± 3.3%	5.87 ±70.6%	278 ± 3.5%
	n / -	0.214 ± 8.1%	0.254 ±10.2%	0.579 ± 5.4%	1.48 ± 9.5%
	m / -	0.832 ± 2.6%	3.47 ± 3.4%	0.828 ± 2.2%	3.64 ± 3.1%
$FeO \rightleftharpoons Fe$	$k^{\otimes}$ / 10^{-4} mol s⁻¹ g⁻¹	4.49 ±4.13%	9.44 ± 4.8%	3.94 ± 5.2%	9.05 ± 4.9%
	E / 10^3 J mol⁻¹	176 ± 0.9%	123 ± 1.7%	179 ± 1.0%	122 ± 1.6%
	n / -	0.109 ± 7.4%	0.172 ± 9.3%	0.91 ± 2.1%	0.93 ± 2.7%
	m / -	1.84 ± 0.9%	2.04 ± 1.4%	1.80 ± 1.1%	2.03 ± 1.4%

Table 3.5.: Identified kinetic parameters for the system Fe_3O_4/FeO/Fe/CO/CO_2 based on the experiments described in Sec. 3.1 and the models described in Sec. 3.2. Examples for the kinetic formula are given in Eqs. 3.17 and 3.18. The kinetic parameters used for the reactions with H_2/H_2O are the same, except for the pre-exponential factors $k^{\otimes}$, which are multiplied by 6.06 (Avrami) or 6.45 (UCM) to account for the higher reaction rates.

Four of the eight fits are shown in Fig. 3.13 to 3.15 to visualise their quality. The most noticeable feature not fitted by the models are the different sample masses at steady state. The reason might be the different oxidations states of FeO, which are not considered in the model (see Sec. 2.3). The seemingly different steady state masses in the most reduced state of Fe are unaccounted for.

Fig. 3.13a and 3.13b show reaction 2, the reduction of FeO, modelled with the Avrami model and the UCM. The fits have very similar quality. The Avrami model can produce slightly sigmoidal TGA curves with slow reactions. Only a selection of curves is shown, due to the large number of fitted data sets.

Fig. 3.14 shows the oxidation of iron, which does not show sigmoidal curves. It is fitted nicely by the Avrami model (shown) and the UCM. Similar things hold for the reduction of Fe_3O_4 in Fig. 3.15 and the other, not shown, reactions. Fig. 3.15 shows all fitted data sets to give an impression of their number.

3.3.4. Discussion

The Avrami model and the UCM show quite similar results in the qualitative fit (Fig. 3.13), the quantitative fit (Tab. 3.4) and the values for parameters $k^{\otimes}$, E and m in each reaction. The Avrami model does not exhibit its capability to fit sigmoidal TGA curves as strikingly as expected for the sake of a better fit of all FeO reduction experiments. When comparing the residuals, the UCM even has a slight advantage in the fitting of this reaction, but is on par with the competing model overall. Comparing the confidence intervals, which will themselves be discussed below, yields the same result: neither model is better. Because of its simplicity, the UCM was chosen for the CWGSR model of Chapter 4.

An interesting result of the data collected in Tab. 3.5 is the exceptionally low activation energy of the reduction of Fe_3O_4 and the high value for the backward reaction. This can be interpreted as different sensitivities to temperature changes, which might be exploited to adjust the ratio of oxidation and reduction durations in a CWGSR setting.

The interpretation of n and m as reaction orders is tempting. But, adding to the argument that at least the UCM is a very phenomenological model, not representing the true mechanics of the reactions, Levenspiel in [56] argues that

> "In homogeneous reactions the reaction order is tied to the mechanism of action of the molecules and it has theoretical meaning. For catalyst decay the order of deactivation is a convenient tool which leads to generalisations, simple mathematics
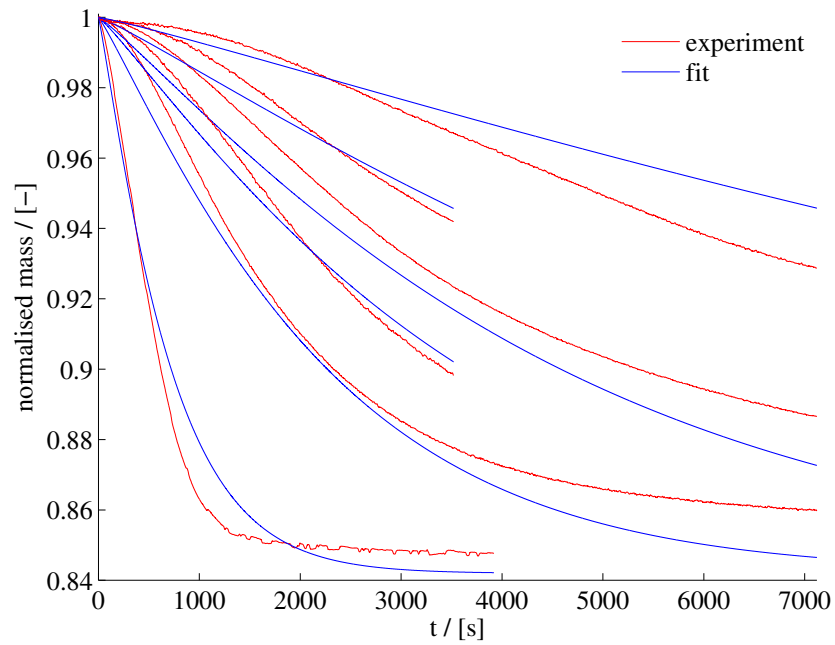
(a) Avrami Model (JMAK)
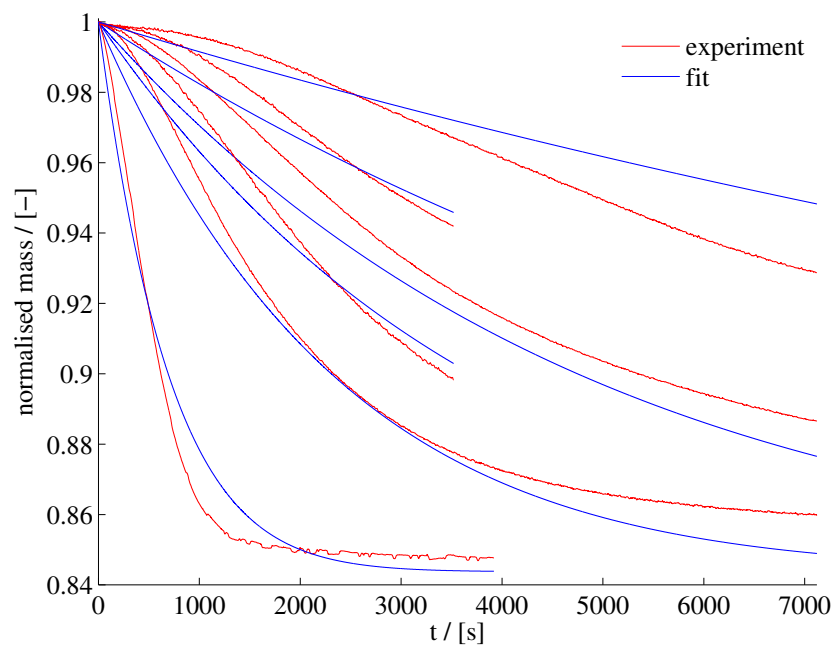
(b) Uniform Conversion Model (UCM)

Figure 3.13.: Reduction of FeO to Fe with CO/CO_2. A selection of experimental data and model fits. Parameters are summarised in Tab. 3.5.

Figure 3.14.: Oxidation of Fe to FeO with CO/CO_2. A selection of experimental data and fits using the Avrami model.

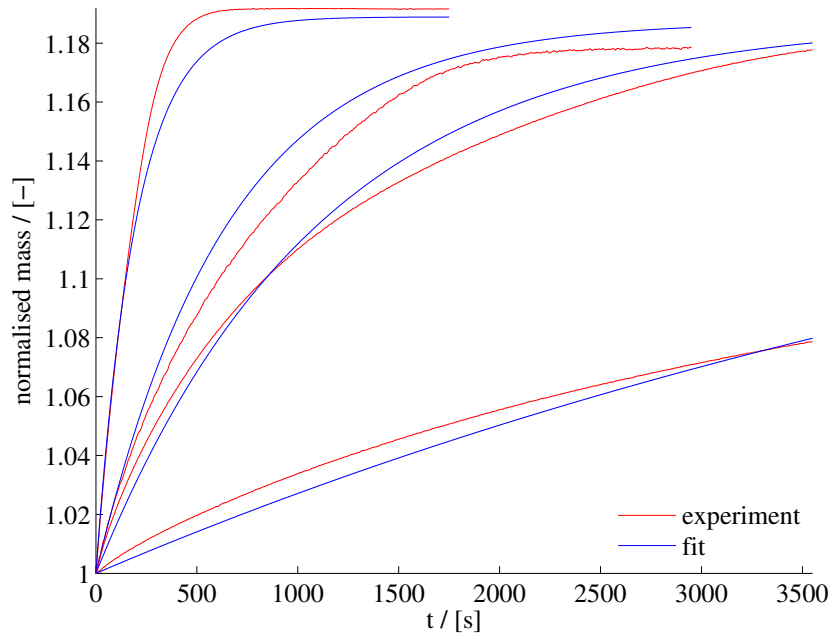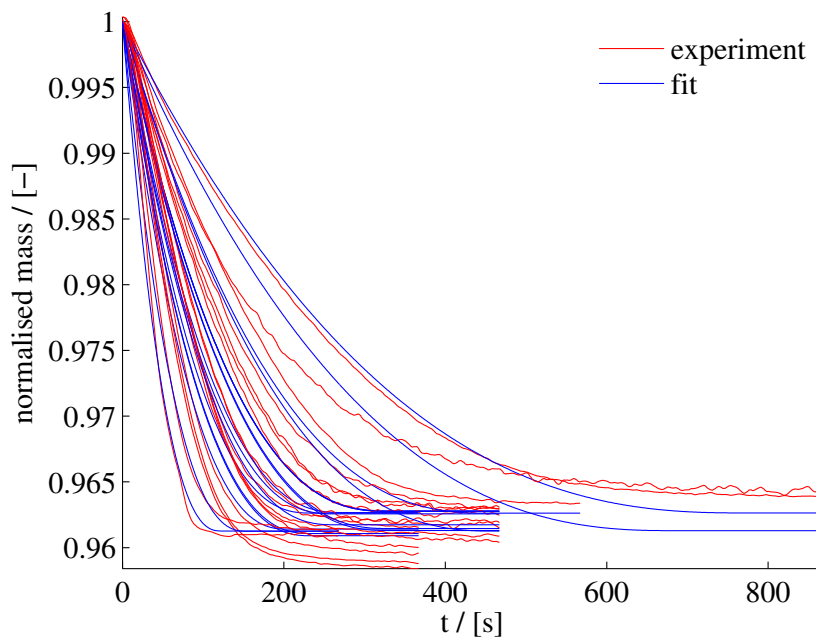Figure 3.15.: Reduction of Fe_3O_4 to FeO with CO/CO_2. All measurements and their fits using the Uniform Conversion Model (UCM).

and simple design. However for the conversion of solids the reaction order does not seem to be a simplifying concept and it does not particularly clarify. Thus it is best to avoid using it."

The spread of the identified activation energies is huge compared to the data of a single work in literature, but not implausible compared to the range given in reviews (13.4 to 246 kJ mol^{-1} in [76, 77]). For the reduction of iron oxide, Tsay et al. [99] reported 64 to 74 kJ mol^{-1}), Takenaka et al. [96] 67 to 75 kJ mol^{-1}, Moon et al. [67] 20 to 42 kJ mol^{-1} and Valipour et al. [100] 75 to 117 kJ mol^{-1}. The increase of the reaction rates involving H$_2$ is also smaller in literature: Tsay describes a factor of 1 to 2, Moon between 2 and 3, and Takenaka uses a factor of 5. All cited studies used natural iron ore with different amounts of trace minerals.

A notable feature of the given kinetic parameters are the small error estimates or confidence intervals. They seem to be oblivious to the wealth and spread of kinetic data in the literature. That is because the literature and measurements other than the ones taken in this work were not used for the estimation of said intervals.

The parameters as well as the error estimates are model and experiment dependent values. The model is based on many assumptions and the experiments depend on many variables of which some might be wrong or systematically skewed. A true value might be outside of a given confidence interval. But regarding the set of measurements in this work and this model, the chance of that is below the 5 % margin.

The given confidence intervals are less a measure of the quality of fit, but more a measure of sensitivity of the model fit with respect to parameter variation. In this interpretation, a large confidence translates into a low sensitivity of the model fit.

3.4. Summary

The reaction rates of 400 µm particles of the self-prepared iron oxide material (Sec. 2.1.2) were measured via TGA in a CO/CO$_2$/N$_2$ atmosphere of varying composition and temperature. A variety of models was formulated that conform to the thermodynamic equilibrium conditions and reflect a potential reaction mechanism. Two models, the Avrami model and the Uniform Conversion Model, were fitted to the experimental data (Tab. 3.5) with similar accuracy. The subsequent modelling of the CWGSR will be done with the UCM as the reaction submodel.

In the future, the biggest improvement could be achieved by dedicated measurements of reduction and oxidation reactions in different H$_2$/H$_2$O/N$_2$ atmospheres. The kinetic parameters

for these important reactions for the CWGSR were extrapolated from the CO/CO_2 data and one data set as point of reference in the H_2 realm.

A complete study of the material's reaction kinetics would also involve a thorough experimental analysis of the influence of the pelleting process as well as the pellet size on the reaction rates. This was assessed in Sec. 2.2.3 by estimations based on material properties and correlations. However, the CWGS reactor model would benefit from dedicated measurements.

4. CWGSR Analysis

The previous two chapters addressed the preparation and kinetics of an oxygen storage material to be used as fixed bed in the cyclic water gas shift reactor (CWGSR). The present chapter will employ these findings and test, whether the CWGSR can actually show the properties and behaviours like moving reaction zones and an advantageous flow reversal flow mode, that were predicted by Heidebrecht, Sundmacher and the author [46–48]. For the experimental investigation of the reactor, a test stand was constructed. A model, able to simulate the experimental results, was formulated for the model based analysis of the CWGSR.

4.1. Experimental

Three experiments are described in this thesis. It was tested, whether

(a) moving reaction zones can be created in an iron-based CWGSR, whether

(b) a stable, CO consuming, H_2 generating cycle can be established, while maintaining moving reaction zones, and whether

(c) the operation mode based on short cycle duration and flow reversal is better in comparison to long cycle duration and/or keeping the gas flow direction uniform (feed forward mode).

The fixed beds used in these experiments are based on pure iron, pelleted with a silica solution as described in Sec. 2.2.1. Albeit a number of these fixed beds were prepared, all experiments presented and analysed in Sec. 4.1.2 were done with one and the same fixed bed. All experiments of Sec. 4.1.3 and 4.1.4 were performed on another fixed bed, which was prepared in an identical way. Results obtained from other fixed beds were not used in this analysis.

Figure 4.1.: Composite photograph of the CWGSR test stand in the Laboratory Pilot Hall of the Max Planck Institute for Dynamics of Complex Technical Systems, Magdeburg.

4.1.1. Reactor Test Stand Setup

A test stand was built in the Laboratory Pilot Hall of the Max Planck Institute for Dynamics of Complex Technical Systems, Magdeburg. The test stand could supply CO, CO_2, H_2, N_2 and steam, feed a tube reactor of 1 m length from both ends at $750\,°C$ and measure the composition of the exhaust gases continuously.

The test stand, shown in Fig. 4.1, was built by lab engineer Torsten Schröder with input on equipment sizing, operating requirements and design conditions from the author, and the mechanical and electrical workshops of the Max Planck Institute. Testing and characterisation was done by the author with additional contributions from his student Elina Gedicke, supervised during the preparation of this work (see page 117).

The process and instrumentation diagram (P & ID) is given in Fig. 4.2. The test stand can be divided into three sections: The gas supply (marked red on the P & ID), the reactor itself (blue) and gas analytics (green). The following paragraphs describe these three units in more detail.

Figure 4.2.: Process and instrumentation diagram (P & ID) of the CWGSR test stand. Gas mixing is marked red, the reactor blue, and gas analysis and vent green.

MFC	Gas	Capacity /NL/min	Type
F007	CO_2	0.5	Bürkert 8712
F001	H_2	2.0	Bürkert 8712
F002	CO	1.0	Bürkert 8712
F003	N_2	1.0	Bürkert 8712
F004	H_2O	2.1	Bronkhorst L13V02-PGD-33-K30S
F005	N_2	1.0	Bronkhorst F-201C-PGD-33
F408	N_2	0.5	Bürkert 8712

Table 4.1.: Mass flow controllers (MFC) of the CWGSR test stand. The H_2O MFC has a nominal mass flow rate of $100\,\mathrm{g\,h^{-1}}$.

The gas supply and dosing unit is shown in more detail in Fig. 4.3. Gases available are CO_2, H_2, CO, N_2 and H_2O. These gases are grouped into three lines, which can be routed via an array of six valves (V001 to V006) either to the reactor ("Strang 1") or directly to the exhaust (via static mixer M2). The latter is important e. g. for the steam supply, which takes considerable time for stabilisation after setting a flow rate. The mixing section was heated to $120\,°\mathrm{C}$ by heating tape W004, W005, W101 and W201. Mass flow controllers (MFCs, temperature and pressure corrected FICs) were tested with a film flow meter "HORIBAstec SF-1U/2U" and could be operated to a tenth of their nominal capacity, given in Tab. 4.1.

The steam supply module consists of the receiver tank B1, an MFC and the evaporator. The tank is filled with demineralised water and pressured by a nitrogen blanket to 2 bara. The evaporator is of type "aSTEAM" by "aDROP Feuchtemeßtechnik GmbH", Germany, consisting of an evaporator W007/DV2, followed by a superheating unit W008/NH1B.

The reactor unit, shown in Fig. 4.4, is made up of the reactor with its oven W304 and four valves to allow for forward and reverse gas flow (V301 to V304). The reactor tube is made of heat resistant, stainless steel (1.4845, 310), has a length of $100\,\mathrm{cm}$, an inner diameter of $2\,\mathrm{cm}$ and a wall thickness of $5\,\mathrm{mm}$. The reactor is mounted vertically. The fixed bed is $65\,\mathrm{cm}$ long and held in place by a sieve plate. The material is described in Sec. 2.1.1 and 2.2.1. Typical gas residence times are 0.5 to 2 s. The reactor's temperature is controlled by a $3\,\mathrm{kW}$ electrical oven, which completely encases the fixed bed and additional $10\,\mathrm{cm}$ of up- and downstream reactor tubing. The four surrounding valves allow the supplied gas to be fed from either side of the reactor: for forward flow V301/V3033 are closed, V302/V304 open; for reversed flow the inverse. The four valves are secondary packed bellows sealed valves by Swagelok (SS-12UW-MM-HT-6C), able to operate at up to $650\,°\mathrm{C}$.
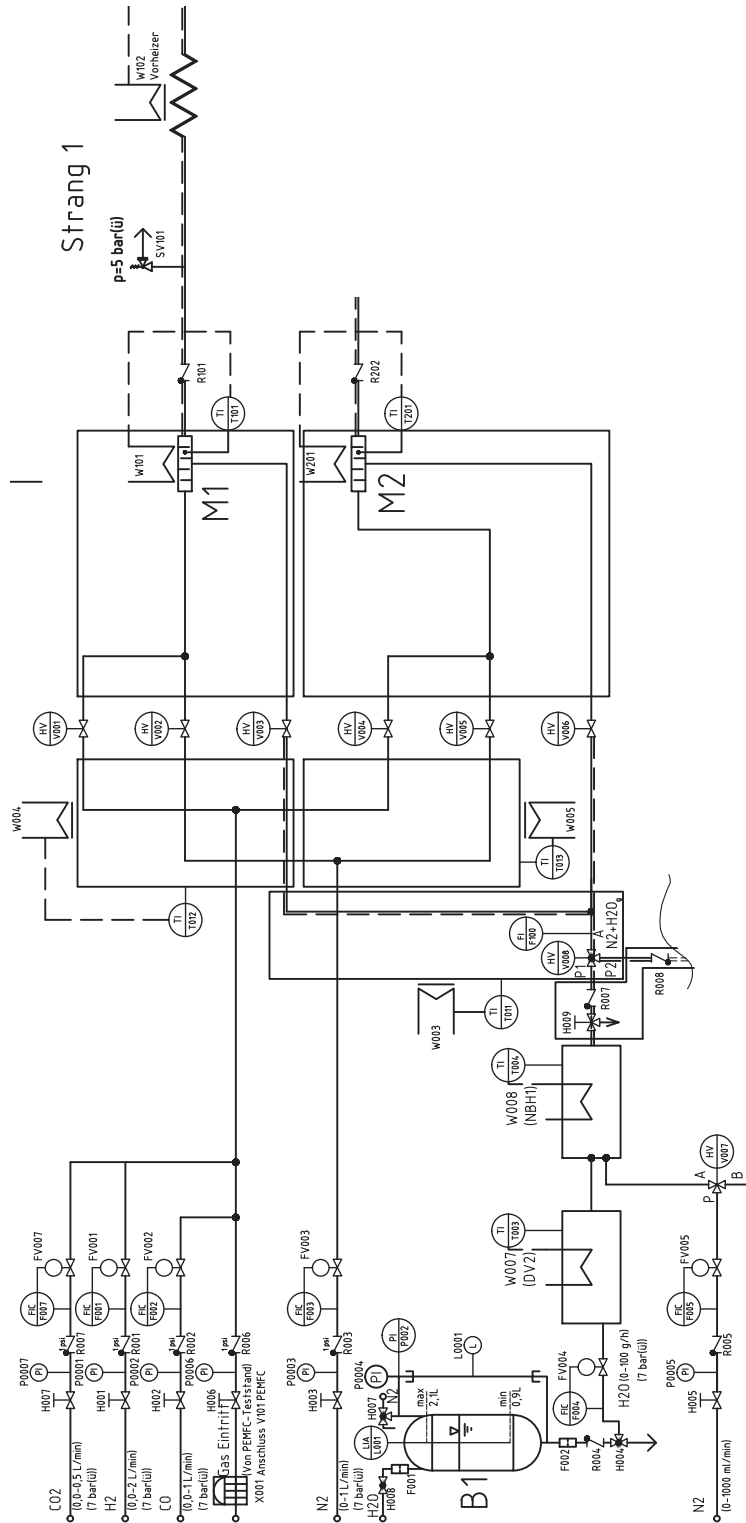
Figure 4.3.: Detail view of the gas dosing, mixing and preheating section of the test stand P & ID. Compare to Fig. 4.2, red section.
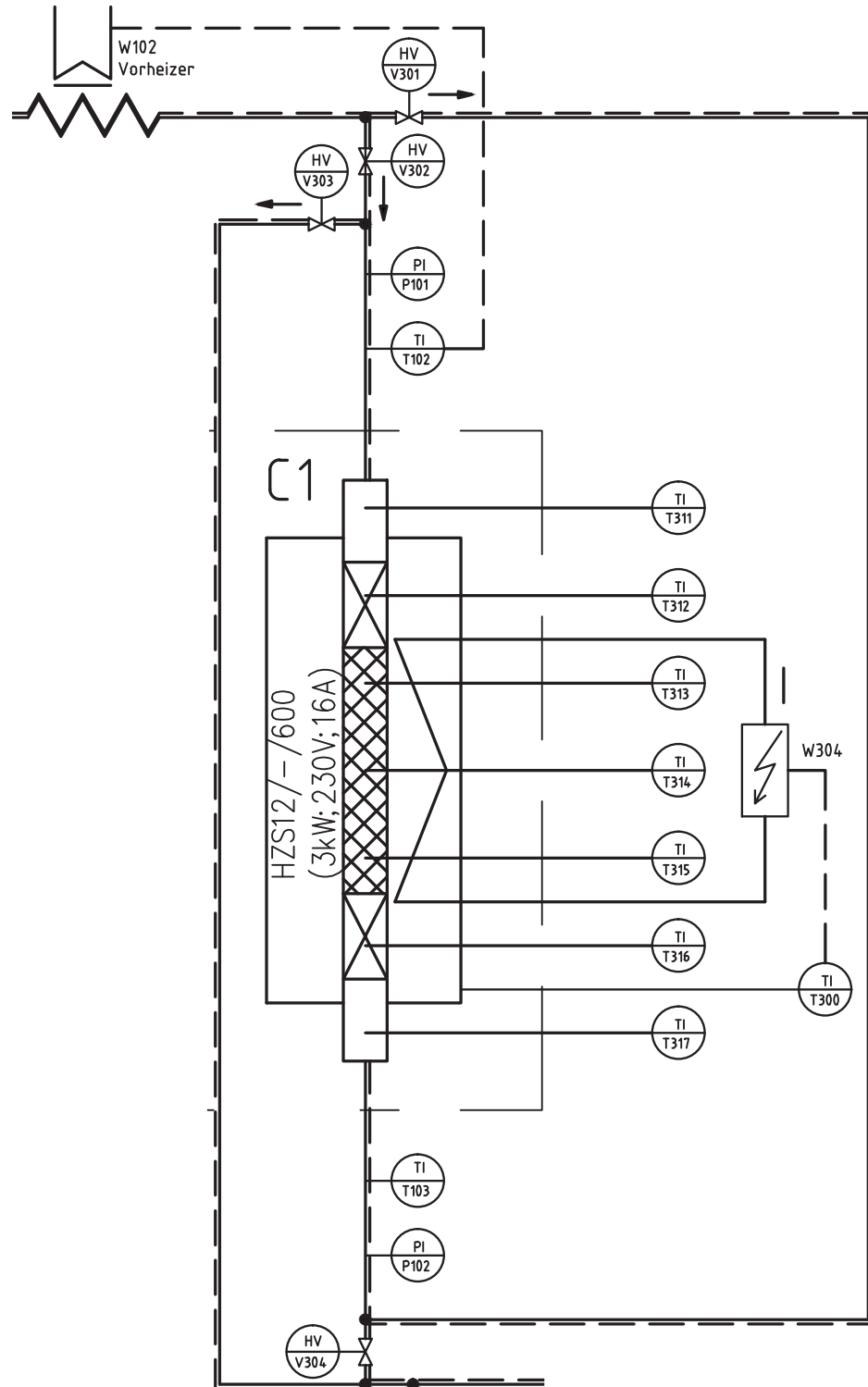
Figure 4.4.: Detail view of the reactor section of the test stand P & ID. Gas from the dosing and preheating section enters from the top left. Compare to Fig. 4.2, blue section.

The introduction of temperature measurement probes (T311 to T317) to the fixed bed was attempted but failed. The attempted configuration involved several non-shielded, axially spaced temperature elements, led out of the reactor along the central axis through the top inlet. The temperature elements were not protected by an inner tube to avoid any extra channeling effects in the fixed bed and to improve measurement response. However, this made the elements vulnerable to tearing off by any settling actions of the fixed bed, caused for example by pellet disintegration. Further problems were encountered in finding the right balance between structural stability and thermal decoupling of the service wiring.

The exiting gas was fed to the last section of the test stand for analytics and venting (see Fig. 4.5. Gas from the reactor or its bypass was cooled in W106 to condense steam and fed to the exhaust vent system of the Laboratory Pilot Hall, where it was diluted below explosion and toxic limits. A typical 10 NL/h were drawn from the gas exiting the reactor and fed to the gas analyser (Q401). To avoid drawing in gases from the exhaust in case of too little flow through the reactor, downstream of the condenser W402, N_2 could be added to the flow. This was later accounted for in the quantitative analysis.

The online gas analyser Q401 was an ABB 2000 unit by ABB, Switzerland. The concentration of hydrogen was measured by a thermal conductivity sensor (TCD unit Caldos 15 by ABB) at a sample rate of $1\,s^{-1}$. In this device, the temperature in a filament is measured via its electrical resistance. The filament temperature depends on the heat transfer coefficient between the filament and the surrounding gas, which in turn depends on the gas composition. Due to the thermal inertia of the filament, the sensor temperature could not instantaneously follow a change in gas composition. The dynamic behaviour of the TCD sensor can be described as a transfer element of first order (PT1). Dedicated experiments indicated a time constant of 10 to 30 s, depending on the average H_2 concentration, i. e. the heat capacity of the gas. CO and CO_2 were measured by a nondispersive infrared sensor (NDIR unit Uras 14 by ABB). Its dynamic behaviour was not a function of gas composition. The H_2 sensor had a measuring range of 0 to 100 vol−%, the CO/CO_2 sensors of 0 to 30 vol−%. However, the latter could be used reasonably well above this limit given careful nonlinear calibration, independent and outside of the ABB unit.

All lines downstream of the gas supply's MFCs and upstream of the analytics' condensers were heat traced to 120 °C. All lines downstream of preheater W102 were heated to 450 °C. The oven and reactor temperature was 750 °C.

The test stand was controlled and data were recorded via the PLC Siemens Simatic S7.
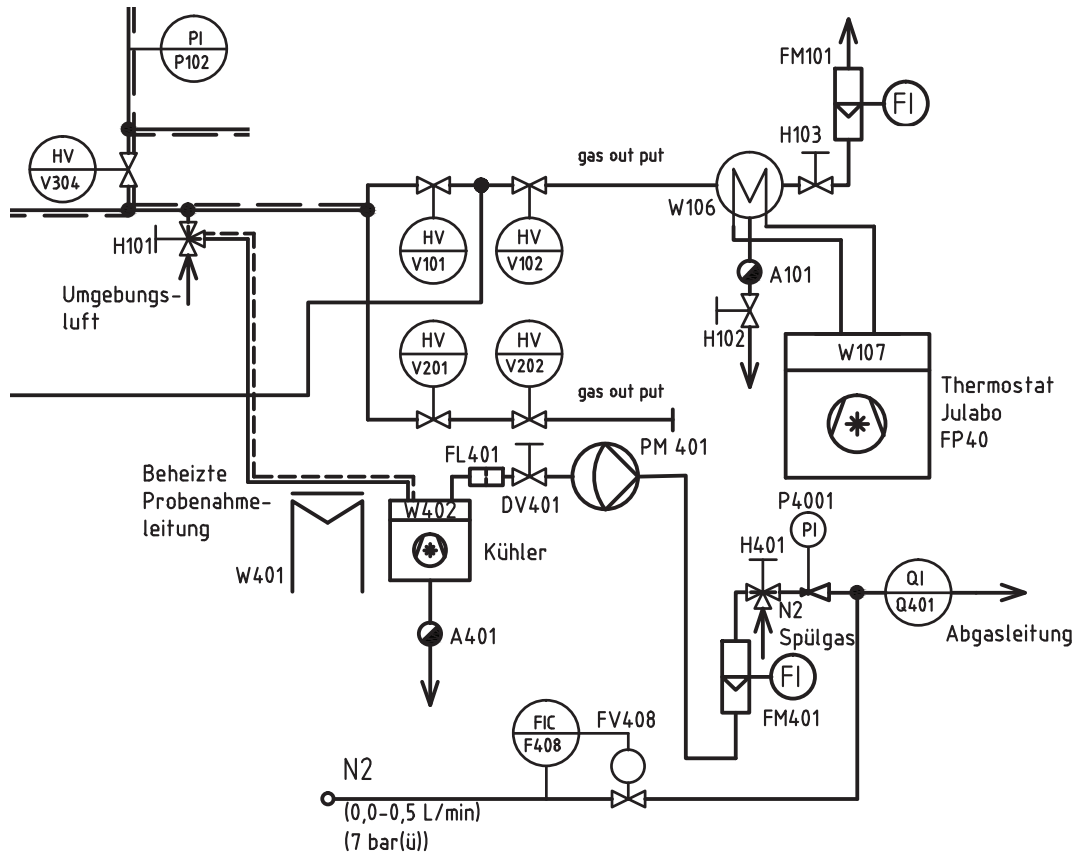
Figure 4.5.: Detail view of the gas analysis and exhaust section of the test stand P & ID. Gas from the reactor outlet enters from the top left. Compare to Fig. 4.2, green section.

4.1.2. Complete Reduction Phase

The goal of this experimental investigation on the reactor scale was to collect information about the dynamic behaviour of the CWGSR and especially to validate the formation of distinctive moving reaction zones, as predicted by Heidebrecht et al. [46]. For this purpose, a fixed bed was repeatedly reduced from Fe_3O_4 to Fe with H_2.

Experimental procedure

At the start of any experiment, the system was at steady state, the temperatures in the heated pipes and in the oven are constant, the gas flow was constant, no reactions occurred and the sensors were equilibrated. Reactions can be avoided by feeding an inert gas mixture (i. e. pure nitrogen) or by applying a gas mixture which is in equilibrium with the current composition of the fixed bed.

At $t = 0$ s, the set values of the installed MFCs were changed simultaneously. The fixed bed was then completely reduced under a constant flow of reactant gases. A gas mixture of H_2 and N_2 was used in the presented experiments. The transient signals of the gas sensors were recorded until the new steady state was reached.

Results

The hydrogen output concentration profiles during three reduction experiments are shown in Fig. 4.6. They were carried out with identical gas feed mixtures (83 % H_2, 17 % N_2), but at different gas flow rates. The transients of the concentrations at the reactor outlet are characterised by breakthroughs of reactions zones. Before and in between these breakthroughs, the gas concentration corresponds to the equilibrium composition. At the end of each experiment, the output concentration equals the feed composition.

Two breakthroughs were observed per experiment. There are two kinds of reaction zones in an iron-based CWGSR operating at temperatures above 574 °C: An iron/wuestite (Fe/FeO) zone and a wuestite/magnetite (FeO/Fe_3O_4) zone (see Fig. 4.7). The moving zones differ in speed, which is discussed on p. 71. The Fe-FeO zone trails behind the FeO/Fe_3O_4 zone.

During the first few moments of the reduction experiments, both reaction zones were present in the reactor, and the exhaust gas composition corresponded to the equilibrium of the H_2/H_2O system at the FeO/Fe_3O_4 equilibrium (shown in Fig. 2.5 on p. 26, along with an in-depth discussion on the equilibria). According to Bogdandy [8], this equilibrium is attained at the given reactor temperature (750 °C) if $y_{H_2O} = 66$ %. This means that 66 % of the fed hydrogen
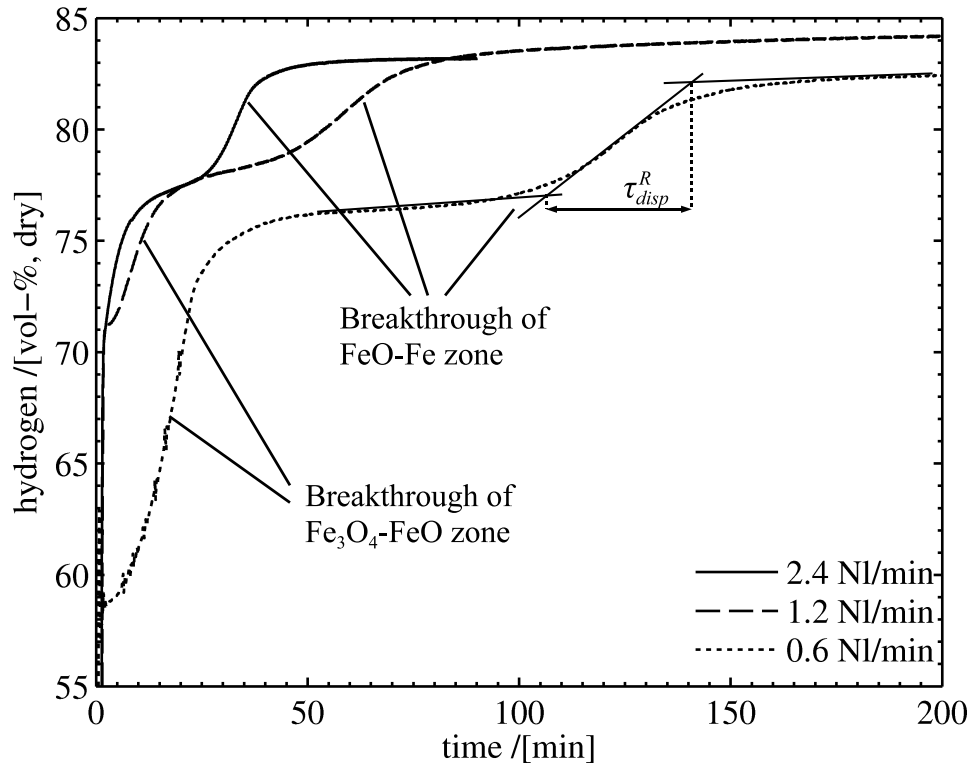
Figure 4.6.: Three reduction experiments at different gas flow rates and identical feed gas composition (83 % H_2, 17 % N_2). $T = 750\,°C$, $p = 1.3\,bara$, Material: see Sec. 2.2.1.
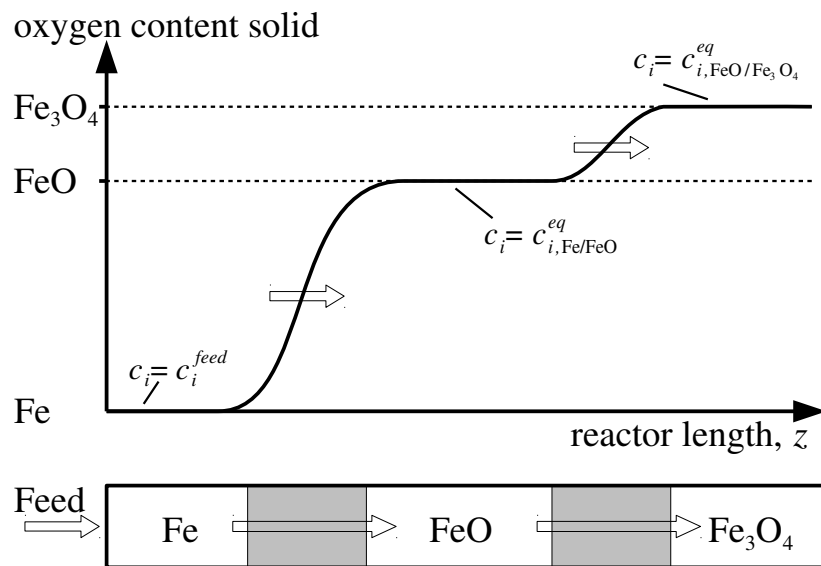

Figure 4.7.: Qualitative representation of travelling reaction zones during the reduction phase of Fe_3O_4 to Fe.

is converted to steam at the end of the FeO/Fe$_3$O$_4$ reaction zone. With a feed gas composition of 83 % H$_2$ and 17 % N$_2$, this corresponds to 55 % H$_2$O, 28 % H$_2$ and 17 % N$_2$ at the exhaust, or 62 % H$_2$ on dry basis.

In the response curve of the experiment with the lowest feed flow rate (Fig. 4.6, dotted line), a similar concentration was observed for a short time, before the FeO/Fe$_3$O$_4$ reaction zone reaches the reactor outlet and breaks through. This concentration level could not be observed in the other two experiments performed at higher gas flow rates, because the reactor was not sufficiently long for the gas to reach equilibrium. Furthermore, the dynamics of the plant (and especially the sensor) and the breakthrough dynamics the FeO/Fe$_3$O$_4$ reaction zone were overlapping.

After the breakthrough of the first reaction zone, the H$_2$ concentration at the outlet stayed approximately constant at 75 to 77 % for some time. This corresponds well with the equilibrium state between FeO and Fe of $y_{\text{H}_2\text{O}} = 33\%$ at reactor temperature. With the given feed gas composition, this corresponds to 77 % H$_2$ on dry basis. After some time, which evidently depends on the gas feed rate, the second reaction zone (Fe/FeO) broke through. After that, no reaction took place in the fixed bed and the exhaust gas composition was identical to the feed gas composition.

Residence time of the reaction zones

The travelling speed of a reaction zone depends on the amount of reactants available in the gas phase and the solid phase and on the gas velocity. Heidebrecht and Sundmacher [46] discussed this in detail and formulated the following expression for the Fe/FeO zone velocity (here simplified for a H$_2$/H$_2$O atmosphere):

$$\omega_{\text{Fe/FeO}} = \frac{u \cdot \varepsilon \left(c_{\text{H}_2\text{O,Fe/FeO}}^{eq} - c_{\text{H}_2\text{O}}^{feed} \right)}{\Delta C_{\text{Fe/FeO}}^s + \varepsilon \left(c_{\text{H}_2\text{O,Fe/FeO}}^{eq} - c_{\text{H}_2\text{O}}^{feed} \right)} \tag{4.1}$$

71

Although this equation has been derived under the assumption of chemical equilibrium, it is also applicable to describe the zone velocity at finite reaction rate constants. The residence time of the reaction zone can be formulated as:

$$\tau_{res}^R = \frac{L}{\omega_{Fe/FeO}}$$

$$= \frac{L}{u} \cdot \frac{\Delta C_{Fe/FeO}^s + \varepsilon \left(c_{H_2O,Fe/FeO}^{eq} - c_{H_2O}^{feed} \right)}{\varepsilon \left(c_{H_2O,Fe/FeO}^{eq} - c_{H_2O}^{feed} \right)} \tag{4.2}$$

The oxygen capacity of the solid phase, $\Delta C_{Fe/FeO}^s$, is three to four orders of magnitude larger than the amount of convertible oxygen in the gas phase (bracketed term in the denominator). Therefore, characteristic time scales of the gas phase are much smaller than those of the solid phase.

For stoichiometric reasons, the oxygen capacity of the solid phase in the Fe/FeO zone, $\Delta C_{Fe/FeO}^s$, is three times larger than the one in the FeO/Fe$_3$O$_4$ zone. Given equivalent conditions (e. g. difference between gas and gas equilibrium concentration), the FeO/Fe$_3$O$_4$ zone will move three times as fast as the Fe/FeO zone.

Dispersity of the reaction zones

The reaction zones also widen. The main reason for this phenomenon are the limited rates of the gas-solid reactions. In the limiting case of infinite reaction rates, a reaction zone would travel as a shock front through the reactor. In case of very slow rates or low Damköhler numbers, reaction zones are stretched and will fill the whole reactor length or even exceed it. A basic measure to quantify the dispersity of a reaction zone is the duration of their breakthroughs, τ_{disp}^R, as illustrated in Fig. 4.6.

Reaction zone time constants

The three experiments shown in Fig. 4.6 enable the estimation of time constants of the reaction zones at varying gas velocities. The results for the Fe/FeO waves of all three experiments are summarized in Tab. 4.2. They show that τ_{res}^R is clearly proportional to the inverse of the gas feed rate. The width of the reaction wave is also increasing with decreasing flow rate, but no quantitative correlation can be derived from the available data. This could be attributed to the

Flow rate / NL/min	$\tau^R_{\text{res,Fe/FeO}}$ / min	$\tau^R_{\text{disp,Fe/FeO}}$ / min	$\tau^R_{\text{res,FeO/Fe}_3\text{O}_4}$ / min	$\tau^R_{\text{disp,FeO/Fe}_3\text{O}_4}$ / min
0.6	122	32	16	19
1.2	57	28		
2.4	31	10		

Table 4.2.: Residence times and dispersion time constants estimated from the experimental data depicted in Fig. 4.6.

superimposition of effects of the gas velocity and degradation of the fixed bed material, as experiments with smaller gas velocities were conducted later in the fixed bed operating life.

Time constants for the Fe_3O_4/FeO reaction zone were only estimated for the lowest gas flow rate. Breakthroughs at higher flow rates could not be dimensioned unambiguously.

The time constants given here deviate from the ones associated with the analysis equipment or potential mass transport limitations within the pellets by at least an order of magnitude (see Sec. 4.1.1 and 2.2.3, resp.). They should therefore represent intrinsic reactor characteristics.

4.1.3. Complete Reduction-Oxidation Cycle

The generation of pure H_2 from syngas or CO and steam is the CWGSR application scenario of this work. This basic reaction scheme of the steam iron process had been tested thoroughly before. The goal of the here presented experiment was to investigate a complete cycle of the steam iron process performed in the CWGSR *and* to create and observe moving reaction zones via concentration plateaus and breakthroughs in the gas output. The utilisation of these reaction zones can lead to higher efficiencies in the operation of the steam iron process.

Experimental procedure

A freshly prepared fixed bed (149.2 g) from a new pelleting batch was used for all cyclic operation experiments. Prior to these experiments, the fixed bed was completely reduced to Fe_3O_4 by an appropriate mixture of CO/CO_2.

For this experiment, a complete reduction to Fe by CO/CO_2 and a subsequent oxidation to Fe_3O_4 by H_2O at $750\,°C$ was planned. For the first phase, a feed gas with $y_{CO_2} = 0.24$ ($x_{CO} = 0.70$, $x_{CO_2} = 0.22$, $x_{N_2} = 0.08$) was applied at $1.35\,\text{NL/min}$ for $300\,\text{min}$ until both anticipated reaction fronts passed through the reactor and the gas outputs were stable. The gas feed of the oxidation phase consisted of $x_{H_2O} = 0.76$, $x_{N_2} = 0.24$ at $0.83\,\text{NL/min}$ for another

250 min. These conditions were chosen to achieve sufficiently high reaction rates at low gas flow rates to successfully detect breakthrough phenomena at the reactor outlet.

Results

Fig. 4.8 shows the output concentrations profiles recorded during this experiment. Fig. 4.8a looks very similar to the previously discussed complete reductions with H_2 in Fig. 4.6. Two breakthroughs are clearly visible at 25 min and 245 min. The preceding plateaus match the equilibrium concentrations and expose them to be the Fe_3O_4/FeO and FeO/Fe reaction fronts. Note that the CO/CO_2 sensors are only rated for concentrations from 0 to 30 %. Higher readings are to be taken with increasing suspicion. The notable deviations from the ideally symmetric concentrations profiles are very likely caused by the measurement, not by some unaccounted reaction mechanism. Coking via the Boudouard reaction was thermodynamically not feasible at the employed gas mixtures.

Clearly discernable here is the much higher speed of the Fe_3O_4/FeO reaction zone compared to the FeO/Fe zone – both started at the same time at the upstream end of the fixed bed. As discussed in Eq. 4.1 on p. 71 the main reason for this is the three times higher amount of oxygen that the slower reaction zones has to remove from the fixed bed.

The second phase, the oxidation of the fixed bed and generation of H_2 shows a different picture. Shown in Fig. 4.8b is the H_2 output concentration of the reactor, corrected for the water trap ("wet vol-%") and any additional dilution in the gas analyser (see Fig. 4.5), which was necessary to maintain a minimum exhaust flow. Instead of two breakthroughs only one can be observed for about 75 min. Here, the slower Fe/FeO zone hinders the FeO/Fe_3O_4 zone from advancing, since it precedes the other chemically. Hence, both reaction zones move at the same speed through the reactor and leave it at the same time. A separation would be possible, if the FeO/Fe_3O_4 reaction was slowed down or turned off by applying a y_{H_2O} slightly higher than (or below, resp.) $y^{eq}_{H_2O, FeO/Fe_3O_4}$. The cause of the oscillations is most likely a pulsation of the steam generator.

A rough estimate for the amount of oxygen atoms transferred from the fixed bed to the gas phase during the reduction phase can be attempted in spite of the limited reliability of the sensors at the encountered high CO/CO_2 concentrations. Eqs. 4.3 and 4.4 estimate the amount of oxygen atoms released in the $FeO_{4/3}$/FeO reduction to be a third of the amount released in the subsequent FeO/Fe reduction, which matches the stoichiometry. But during the oxidation,
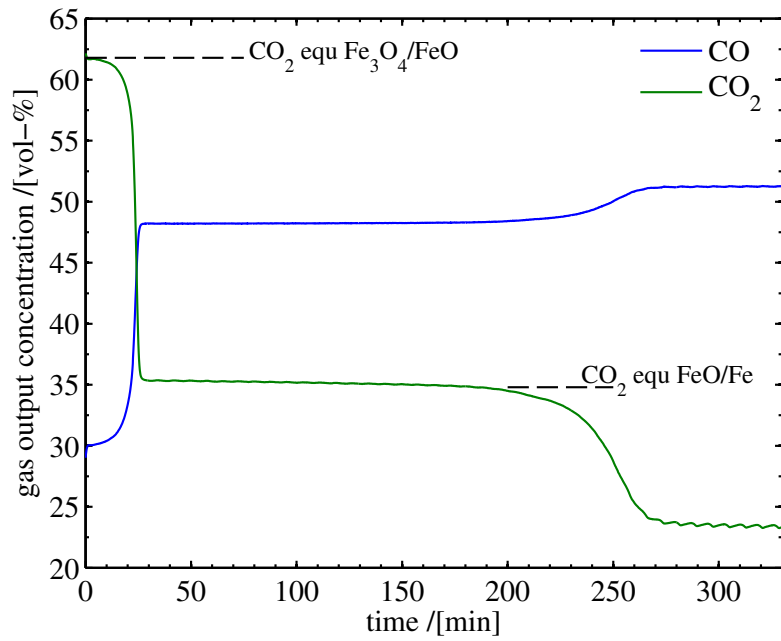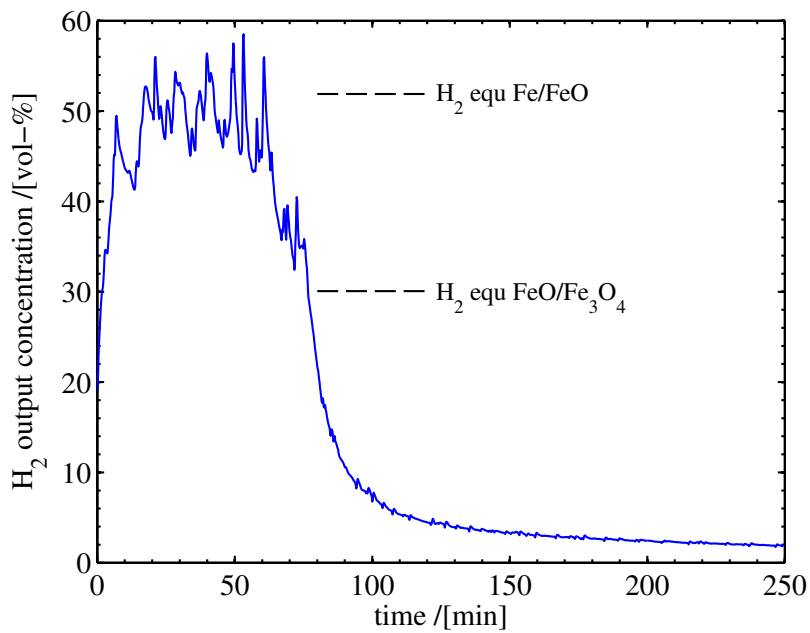
(a) Reduction phase with 70 % CO and 22 % CO_2.

(b) Oxidation phase with 76 % H_2O.

Figure 4.8.: Experimental gas output concentration profiles. Marked equilibrium concentrations ("equ") are theoretical values calculated from chemical equilibrium at feed gas conditions. The inert gas component was N_2.

only about half of the amount of oxygen atoms was reintroduced to the fixed bed (Eq. 4.5). This indicates a fast degradation of the fixed bed.

$$
\begin{aligned}
n_{Fe_3O_4/FeO,+} &\approx \left(x_{CO}^{feed} - x_{CO,Fe_3O_4/FeO}^{eq}\right) \cdot F^I \cdot \Delta t_{Fe_3O_4/FeO}^{plateau} \\
&\approx (0.70 - 0.30) \cdot 0.060\,\text{mol min}^{-1} \cdot 25\,\text{min} \qquad \approx 0.6\,\text{mol}_O \qquad (4.3)
\end{aligned}
$$

$$
n_{FeO/Fe,+} \approx \left(x_{CO_2,FeO/Fe}^{eq} - x_{CO_2}^{feed}\right) \cdot F^I \cdot \Delta t_{FeO/Fe}^{plateau} \qquad\qquad\qquad \approx 1.9\,\text{mol}_O \qquad (4.4)
$$

$$
n_{Fe/Fe_3O_4,-} \approx \left(x_{H_2,Fe/Fe_3O_4} - x_{H_2}^{feed}\right) \cdot F^{II} \cdot \Delta t_{Fe/Fe_3O_4}^{plateau} \qquad\qquad \approx 1.4\,\text{mol}_O \qquad (4.5)
$$

This finding was unexpected, as prior measurement campaigns with other fixed beds of the same type (one is documented in Sec. 4.1.2), did not suffer from fast degradation. Further experiments with this same fixed bed indicated that the oxidation from FeO to Fe_3O_4 was never again successful, as two breakthroughs in the reduction experiments could not be observed. Oxidations were done with both CO/CO_2 and H_2O. Degradation of the fixed bed material through sintering and the missing full oxidation step to Fe_3O_4 therefore seem to be the cause for the lacking oxygen capacity in the second phase. The cause of the lacking oxidation to Fe_3O_4 of this batch of fixed bed material was not discovered. This fixed bed was the last one used in the line of this work and considerably influenced the results of the next experiments.

The density of stored oxygen in the fixed bed material is another important parameter and is closely tied to the density of available iron atoms, $c_{Fe,t}^s$, which will be an important parameter in a model of the system. An approximation based on the measurements in this experiment is given in Eq. 4.6. It is a very good match of the theoretical value estimated in Eq. 4.7. This indicates that, at least in the first reduction of this batch of fixed bed material, every atom in the fixed bed was accessible by chemical reactions with the gas phase. Note that the mass of the fixed bed always relates to the initial weight after its chemical synthesis, when the material is in a completely oxidised state, i.e. Fe_2O_3.

$$
c_{Fe,t,meas}^s = \frac{1.9\,\text{mol}_{Fe}}{149\,\text{g}_{fixedbed}} \qquad\qquad\qquad\qquad\qquad \approx 0.012\frac{\text{mol}_{Fe}}{\text{g}_{fixedbed}} \qquad (4.6)
$$

$$
c_{Fe,t,theor}^s = \frac{0.95\,\text{g}_{Fe_2O_3}}{1\,\text{g}_{fixedbed}} \cdot \frac{1\,\text{mol}_{Fe_2O_3}}{160\,\text{g}_{Fe_2O_3}} \cdot \frac{2\,\text{mol}_{Fe}}{1\,\text{mol}_{Fe_2O3}} \qquad \approx 0.012\frac{\text{mol}_{Fe}}{\text{g}_{fixedbed}} \qquad (4.7)
$$

4.1.4. Continuous Cyclic Operation

Previous investigations described the gas flow reversal with short cycle phases as advantageous mode of operation. Reaction fronts can be preserved inside the reactor and subsequently used to achieve high product concentrations during short, continuous cycles [45–47]. Consequently, the CWGSR was operated with short cycles to compare the flow reversal mode with the forward flow mode.

The same fixed bed is used as in the previous presented experiment. The bed degradation observed is expected to influence the experiment severely as the formation of two reaction zones is an integral part of the reactor concept.

Experimental procedure

The reactor was repeatedly cycled where each phase had a duration of 16 min:

Reduction: $x_{CO} = 0.68,$ $x_{CO_2} = 0.22,$ $x_{N_2} = 0.10,$ $F^{Red} = 0.90\,\text{NL/min}$

Oxidation: $x_{H_2O} = 0.68,$ $x_{N_2} = 0.32,$ $F^{Ox} = 0.62\,\text{NL/min}$

A total of six cycles, or twelve phases, were carried out until the output curves seemed to represent a cyclic steady state. No intermittent flushing phase was applied. A constant amount of N_2 was added to the gas analyser train to provide a sufficient gas stream even during oxidation phases when huge portions of the exhaust could be removed by the cold trap upstream of the analyser as described in Sec. 4.1.1. This additional N_2 and the water trap was accounted for in the evaluation of the experimental data. The presented results show the theoretical "wet" concentrations at the downstream end of the reactor.

Results

Shown in Fig. 4.9 are four phases which form the last two cycles of the experiment: cycles five and six. In the first phase (reduction), a mixture of CO/CO_2 was fed to reduce iron oxide fixed bed. The amount of produced CO_2 decreased continuously during the phase. The measured CO_2 concentration was higher than the feed concentration and higher than the FeO/Fe equilibrium concentration indicating that not only FeO was reduced, but also Fe_3O_4. However, neither are full breakthroughs visible, nor are they separated. A possible configuration of the fixed bed that may have caused this behaviour is characterised by two, almost merged reaction fronts at the right end of the reactor, with the Fe_3O_4/FeO zone about halfway out of the reactor at the start of the reduction phase.
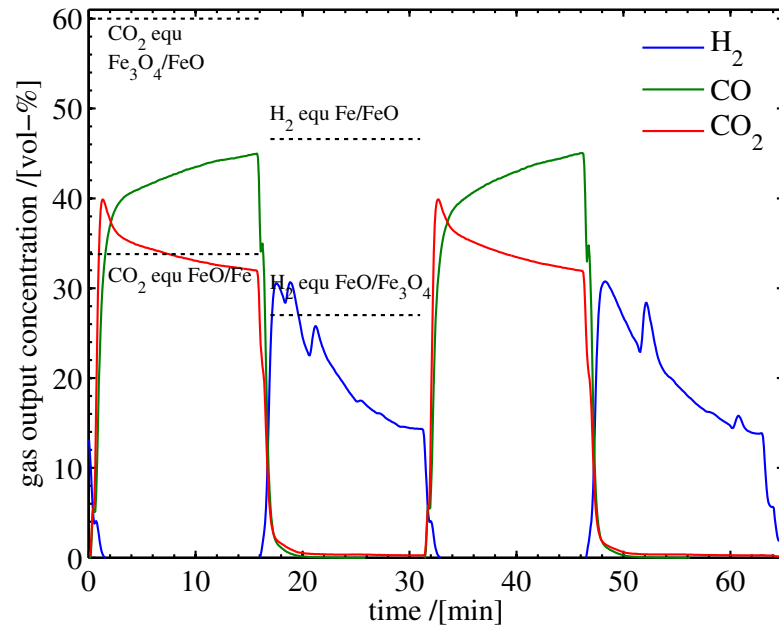
(a) Flow reversal mode.
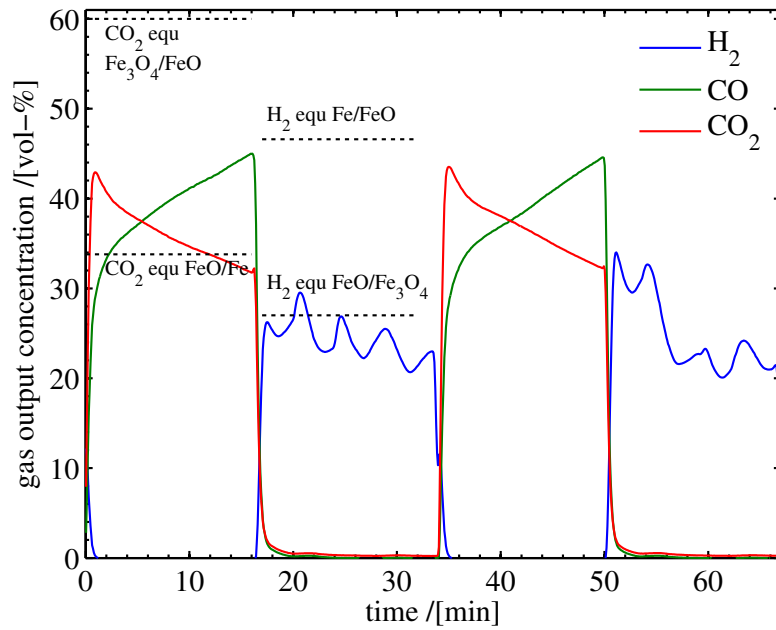
(b) Forward flow mode.

Figure 4.9.: Comparison of the two flow operating modes with short cycles under identical feed conditions. Marked equilibrium concentrations ("equ") are theoretical values calculated from the chemical equilibrium and feed conditions.
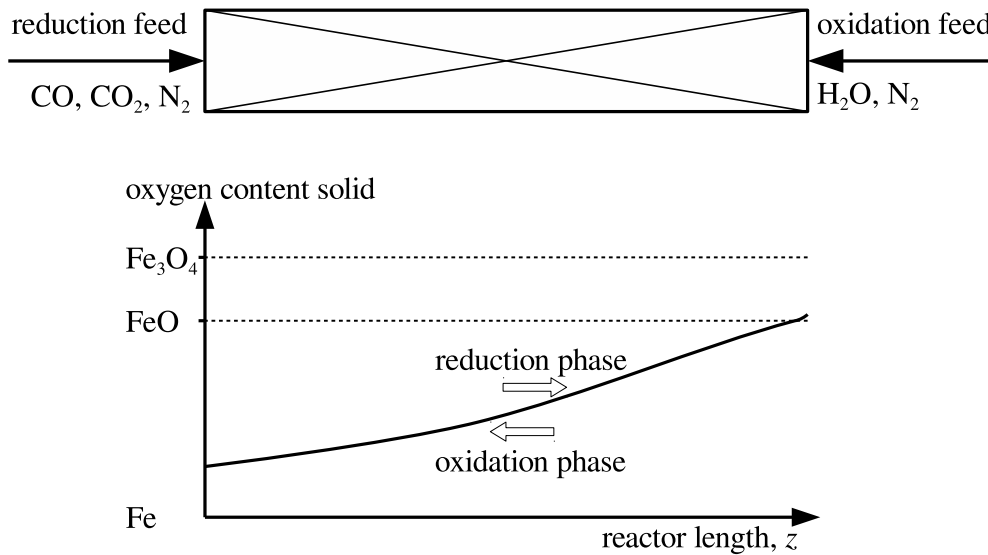
Figure 4.10.: Probable configuration of "reaction zones" in CWGSR during cyclic experiment. Compare with Fig. 4.7.

At the start of the oxidation phase of Fig. 4.9a, the flow is reversed and steam is fed to the reactor from the right hand side. Again, no plateaus are visible in the H_2 output profile. H_2 concentrations higher than the FeO/Fe_3O_4 equilibrium indicate that at least some of the produced H_2 is generated by the oxidation of Fe. The oscillations are most probably caused by the H_2O evaporators.

Taking the indications from both phases into account, a possible oxidation profile of the fixed bed is depicted in Fig. 4.10. Because of the unusually heavy degradation of this fixed bed, reaction rates have slowed down significantly. The ability to oxidise to Fe_3O_4 has nearly vanished. The reduction phase would see the reaction "zones" move slightly to the right, albeit these zones fill the entire reactor due to low reaction rates. Small amounts of Fe_3O_4 are able to oxidise CO and produce CO_2 levels higher than the FeO/Fe equilibrium. A separating plateau is not visible (compare to Fig. 4.7), as the FeO/Fe zone is already breaking through the right end of the reactor. Thus, nowhere in the system thermodynamic equilibrium was established. It is operating under kinetic control with Fe, FeO and sometimes Fe_3O_4 present at the time.

During oxidation phase, steam is fed from the right side, oxidising the fixed bed and raising the profile in Fig. 4.10. Some Fe_3O_4 is formed on the right side. In the part of the fixed bed with only Fe/FeO present, H_2 concentration should reach the Fe/FeO equilibrium concentration shown in Fig. 4.9a but is limited by the reaction rates.

Comparing the forward flow mode with the flow reversal mode in Fig. 4.9 does not support the hypothesis that flow reversal mode is better than forward flow mode. The qualitative behaviour is the same. Quantitatively it is slightly better. The same conclusions as with the flow reversal mode can be drawn from the achieved concentration levels.

The same reactor profile in Fig. 4.10 can be used to explain the reactor behaviour. In difference to the flow reversal mode, steam is now fed from the left side. Sufficiently fast reaction rates would initially raise the profile exclusively at the front of the reactor, forming a "u"-shaped, i. e. convex, oxidation profile. However, the formation of this reaction zone at the reactor entrance would provide so much H_2 (i. e. such a low y_{H_2O}, with $y_{H_2O,Fe/FeO}^{eq}$ as the minimum) that Fe_3O_4 at the right hand side of the reactor would not be formed, but would actually be *reduced* in this oxidation phase if it happened to exist there. But the high CO_2 concentrations at the start of the next phase, proof the existence of Fe_3O_4 at the downstream end of the reactor. The just described effect of forming concave or convex oxidation profiles and thus having the fixed bed oxidise and reduce at the same time is the disadvantage of the forward flow mode of operation. But in this experiment, reaction rates are slow enough that the oxidation profile is raised seemingly simultaneously at all points of the reactor. At the right side, H_2O concentrations (i. e. y_{H_2O}) are still high enough (or x_{H_2} low enough) to oxidise FeO to Fe_3O_4.

An important prerequisite for successful CWGSR operation in the flow reversal mode is the formation of two distinct reaction zones in the reactor. Reaction rates have to be high enough to limit the extent of reaction zones to a fraction of the reactor length. Due to the fast degradation of this last batch of fixed bed material, a successful and as-intended operation of the CWGSR could not be achieved in the just described cyclic experiments.

4.2. Reactor Model

A reactor model is helpful for the adequate analysis and design the CWGSR. Some models have already been proposed, e. g. simple transient models, that do not reflect the true thermodynamics [45, 47], cyclic steady state models, that neglect reaction kinetics [46], or models that assume a well mixed system, i. e. are not spatially distributed [40, 41, 86]. For this reason, a distributed nonequilibrium model was derived to adequately describe the experimental results of this chapter, based on the results of the kinetic study of the previous one. The intended

use of the model is the transient simulation of a CWGSR for optimisation studies of operating and design parameters.

This chapter discusses the model assumptions, its formulation and its numerical solution. The presented model is compared in Sec. 4.3 to the experimental results discussed in the previous section and to an alternative model.

4.2.1. Assumptions

The derivation of the model is based on the following assumptions:

(a) The reactor behaviour is dominated by the movement and breakthrough of the reaction zones. In order to reflect this dynamic behaviour, the CWGSR is modelled as an axially distributed system.

(b) Due to a small diameter to length ratio (2 cm/65 cm), gradients in radial direction are neglected. Although the relatively high particle to tube diameter ratio (3 mm/20 mm) indicates the possibility of gas phase channelling close to the reactor wall, such phenomena are also neglected, as they cannot be verified with the available experimental equipment.

(c) The gas phase follows the ideal gas law.

(d) Because the pressure loss in the experimental plant is less than 0.02 bar along the reactor, isobaric conditions are assumed.

(e) Axial dispersion in the gas phase is neglected.

(f) The gas phase is quasi-stationary. As discussed on p. 71, its dynamics is three orders of magnitude faster than the solid phase dynamics.

(g) Three solid species are considered: iron (Fe), wuestite (FeO) and magnetite (FeO$_{4/3}$). Note that wuestite is assumed to have a fixed atomic ratio of Fe/O in this model. Also note that the stoichiometric formula of magnetite is changed from the common form Fe$_3$O$_4$ in order to normalise the solid species to one iron atom per molecule.

(h) The reactions listed in Tab. 3.1 are considered. The reaction rates are described by the Uniform Conversion Model (UCM), as discussed in Ch. 3. The reaction kinetics also include the mass transport resistance between the gas phase and the fixed bed particles. With regard to the partial mass balance, the reactions are modelled as quasi-homogeneous gas phase reactions.

(i) The reactor is isothermal, the temperature is fixed to the parameter T. Temperature variations of about 15 K, as measured by Thaler et al. [98], were deemed small enough not to influence the reactor characteristics significantly. Without temperature measurements from

the experimental test stand of this dissertation, a validation of an non-isothermal model would not be possible.

4.2.2. Governing Equations

Based on the assumptions stated above, the partial and total mass balances for the gas phase can be formulated. The component mass balances in Eq. 4.8 describe the molar fraction of all components in the gas phase, x_i^g. The first term on the right hand side describes convection by use of the molar flow density, g. The second term is a pseudo-homogeneous source term representing the chemical reactions with the solid phase. σ^s is the bulk density of the fixed bed, the stoichiometric factor $\nu_{i,j}$ is given in Eq. 4.10 and the reaction term r_j is given by example of r_1 in Eq. 3.17.

$$0 = -\varepsilon \frac{\partial(g x_i^g)}{\partial z} + \sigma^s \sum_{j=1}^{4} \nu_{i,j}^g \cdot r_j \qquad x_i^g(z=0) = x_i^{g,feed} \qquad (4.8)$$

$$0 = -\varepsilon \frac{\partial g}{\partial z} \qquad g(z=0) = \frac{F^{feed}}{\pi/4\,d^2\,\varepsilon} c_t^{feed} \qquad (4.9)$$

Eq. 4.9 is derived from the total mass balance in combination with the ideal gas law and the assumption of isobaric and isothermal conditions. It describes the spatial gradient of the molar flow density, g. Since all reactions involved are equimolar with respect to the gas phase and the reactor is isothermal, g remains constant along the reactor. The boundary conditions for these first order differential equations are given by their feed conditions.

$$\nu = \left(\nu_{i,j}^G \mid \nu_{i,j}^S \right) = \begin{array}{c} \\ R_1 \\ R_2 \\ R_3 \\ R_4 \end{array} \begin{array}{cccccccc} CO & CO_2 & H_2 & H_2O & Fe & FeO & FeO_{4/3} \\ \left(\begin{array}{ccccccc} -1 & +1 & 0 & 0 & +1 & -1 & 0 \\ -1 & +1 & 0 & 0 & 0 & +3 & -3 \\ 0 & 0 & -1 & +1 & +1 & -1 & 0 \\ 0 & 0 & -1 & +1 & 0 & +3 & -3 \end{array}\right) \end{array} \qquad (4.10)$$

The composition of the solid phase, x_i^s is described as the amount of molecules of Fe, FeO, and FeO$_{4/3}$ per total amount of iron atoms that are available in the reactions. The solid composition is described by the component mass balances:

$$c_{Fe,t}^s \frac{\partial x_i^s}{\partial t} = \sum_{j=1}^{4} v_{i,j}^s \cdot r_j \qquad (4.11)$$

Because no macroscopic convective or diffusive transport is considered in the solid phase, these mass balances are ordinary differential equations in time. They describe the change of the solid phase composition depending on the reaction rates. Note that $c_{Fe,t}^s$ is the total amount of iron atoms participating in the reduction/oxidation process per mass of fixed bed material. Because every iron atom can take up a certain amount of oxygen, this parameter can be interpreted as the weight specific oxygen storage capacity of the fixed bed material.

The rate expressions for the gas-solid reactions are discussed in detail in Chapter 3 (specifically Eq. 3.17). The latter equation takes into account the thermodynamic equilibrium. The reaction rates show a discrete behaviour. Their sign depends on the relative position of the gas composition to the equilibrium. Thus, the definition of the reaction rates is formulated in a conditional form. Eq. 3.17 shows the rate formulation for reaction 1, the others are analogous. The equilibrium constant K_j^{equ} is defined in Eq. 2.5 and the relative molar fractions y and Y are given in Eqs. 2.3 and 2.4.

4.2.3. Solution

The described model consists of four ordinary differential equations (ODEs) in space (Eq. 4.8) coupled with three ODEs in time (Eq. 4.11). These are combined with several explicit algebraic equations (AEs), e. g. describing reaction rates and chemical equilibria. Two options have been explored to solve this model equation system efficiently.

Discretisation of Space Coordinate & Implementation in Matlab

The system was discretised along the spatial coordinate z, the length of the reactor. This was done via the finite volume method (FVM). The resulting system of ODEs in time and AEs could then be solved by a differential algebraic equation (DAE) solver, which is e. g. implemented in the software package Matlab.

All simulations shown in this dissertation are a result of this approach. But to ease the solution via Matlab 2008b's ode23tb(), the implicit DAE system was converted to a regular, if

somewhat stiff, ODE system by implementing the mass balances of the gas phase as dynamic equations in time, thus removing the assumption of quasi steady state in the gas phase. This increased the number of ODEs, but also increased robustness and decreased computation time. All shown results were computed with 50 discrete volumes along the reactor. One CWGSR cycle took approximately 20 s on a 3 GHz single core desktop CPU to simulate.

The advantage of the relative straightforward implementation and robustness are contrasted by the numerical cost of simulating cyclic steady states of the system. These would have to be simulated directly, which could mean to simulate several hundred or thousand CWGSR cycles until the state variables at the start of the reduction phase have the same value as at the end of the oxidation phase. There are no shortcuts possible without modifying the model. Some of the possible shortcut models were explored e. g. by Heidebrecht et al. [46,47] and Eigenberger and Kolios (e. g. [34]).

Discretisation of Time and Space Coordinates & Implementation in AMPL

The solution of the given CWGSR model via a discretisation of the spatial coordinate z (per FVM) and the temporal coordinate t (per orthogonal collocation [21] over finite elements) was explored by Viktoria Wiedmeyer [102], supervised during the preparation of this work. The resulting large system of implicit algebraic equations can be solved by an adequate algorithm to acquire the same simulation results as with the previous method. Additionally, however, the system's state variables (x_i) at the "left" and "right" boundary of the temporal coordinate t, i. e. the starting and end states, can easily be tied together. This cyclic boundary condition resembles the definition of a cyclic steady state, which can therefore be calculated directly. This solution method was implemented in the optimisation framework and modelling language AMPL [22], using the AE (pre)solver of the optimiser CONOPT [19]. This anticipated the logical step from directly calculating cyclic steady states to optimising operating and design parameters of the CWGSR.

But this method proved to be much more susceptible to numerical problems discussed in the next paragraphs. The range of attraction of a solution proved to be very small, i. e. to attain a solution the solving algorithm had to have a very similar solution (finished simulation of a complete CWGSR cycle) as a starting point. This proved to not be a viable way of solving the CWGSR model, and was therefore abandoned in this line of work.

Numerical Challenges

Both parts of the kinetic expressions, the forward and the backward reactions, have the same value of 0 at the equilibrium condition. Therefore they form a continuous function. But the derivative of composite kinetic expression has a discontinuity at the equilibrium. This non-smoothness is a major source of numerical problems, especially in conditions of "high" reaction rates and fast approaching equilibria which result in overshoots by the solver. A possible solution is the substitution of the kinetic expressions in the close vicinity of the equilibrium ($x^{equ} - \varepsilon$, $x^{equ} + \varepsilon$) with a function designed to be smooth and have a value of 0 at the equilibrium. The substitute would also have to have the same function value and derivatives as the true kinetic expressions at $x^{equ} - \varepsilon$ and $x^{equ} + \varepsilon$.

Another source of numerical problems is the sudden change of the gas phase's flow direction at the start of each CWGSR phase. This is a nonsmooth transition and potentially changes the structure of the discretised model and the configuration of the state space matrix, if e. g. an FVM with an "upwind-scheme" is used. One solution would be the to discretize the system with smoother, higher order approximations. Another option in Matlab is to force the solver to use especially small integration steps at the times of flow reversal, e. g. by solving each phase with a separate call of the solver. A possible solution when working with a sophisticated solver as CONOPT in AMPL is to use its built-in solving strategies for MINLP problems and define the phase as binary variable which switches the flow expressions in the gas balances.

4.3. Comparing Simulation and Experiment

The objective is to validate the model by comparing experimental with simulation results. Due to the problems experienced with the fixed bed in cyclic experiments described in Sec. 4.1.3, the focus will be on the reduction experiments of Sec. 4.1.2. The presented model is also compared with a previously published paper.

4.3.1. Complete Reduction Phase

The experimental data of the complete reduction experiment was condensed in a set of time constants in Tab. 4.2 on p. 73. The model is judged by how well it yields the same time constants given the same set of experimental parameters.

4. CWGSR Analysis

The residence time of the reaction wave, τ_{res}^R, is closely linked to the amount of oxygen that can be withdrawn from the fixed bed while the reaction zone is moving through the reactor. This oxygen capacity depends on the amount of iron atoms that are available for the reaction, $c_{Fe,t}^s$ (see Eq. 4.11). Assuming that the fixed bed material can be reduced completely, we already obtained a theoretical value for this parameter: $c_{Fe,t,theor}^s = 0.012 \frac{mol_{Fe}}{g_{fixedbed}}$ (see Eq. 4.7). In practice, a part of the material can be inaccessible by the gaseous reactants for example because it is blocked or passivated by the binding agent (see Sec. 2.2.1). Therefore, the real amount of available iron atoms corresponds to the theoretical value reduced by a factor, f_O:

$$c_{Fe,t}^s = f_O \cdot c_{Fe,t,theor}^s \qquad\qquad 0 \le f_O \le 1 \qquad\qquad (4.12)$$

The dispersity of the reaction wave, τ_{disp}^R, strongly depends on the reaction rates. The reaction kinetics have been determined with the help of thermogravimetric analysis (TGA) in Ch. 3. However, it is expected that the reaction rates in the CWGSR are lower than in the kinetics study for several reasons. First of all, the material used in the kinetic study had an increased catalytic activity and considerably smaller average particle diameter. Furthermore, in contrast to the CWGSR experiments, no binding agent was used in the kinetic study. Finally, only fresh iron oxide material was used in the kinetic study, whereas the material in the CWGSR reactor suffered from degradation during each experiment that was carried out. The impact of these phenomena on the reaction rate is considered by reaction rate coefficients that were modified by a factor, f_R:

$$k_j = f_R \cdot k_{j,study} \qquad\qquad 0 \le f_R \le 1 \qquad\qquad (4.13)$$

These two unknown factors, f_O and f_R, were used to fit the model to the experimental results shown in Fig. 4.6. In a traditional approach, one would fit the model output to the complete set of reactor output concentration data. But because a good agreement between the simulated and the measured time constants of the reaction wave, τ_{res}^R and τ_{disp}^R, is of special interest, the deviation between them was minimised:

$$\min_{f_R, f_O} \sum_h \left(\left(\tau_{disp,mod}^R - \tau_{disp,exp}^R \right)_h^2 + \left(\tau_{res,mod}^R - \tau_{res,exp}^R \right)_h^2 \right) \qquad (4.14)$$

with h as the number of experiment. The optimisation was carried out using the Matlab algorithm fmincon() using the three experimental data sets plotted in Fig. 4.6.

The results show that 42 % of the fixed bed material can actually be converted in the reduction phase ($f_O = 0.42$). Since the first reduction of the experiment in Sec. 4.1.3 showed the equivalent of $f_O = 1$, the effect can be attributed primarily to fixed bed degradation/sintering and not to the pelleting method. In contrast to that experiment, however, degradation effects set in slower and are much smaller. Degradation is expected to have a much smaller and predictable effect with the use of the stabilised iron oxide material described in Sec. 2.1.2.

With regard to the reaction rates, a factor of $f_R = 0.3$ was obtained from parameter optimisation. This is in the same range as f_O and is most probably correlated with it, as a smaller amount of accessible iron also causes smaller overall reaction rates.

Fig. 4.11 shows a comparison of the experimental data (solid lines) from Fig. 4.6 and the corresponding simulated experiments using the validated model (dotted lines). In addition one further experiment with a different feed concentration is depicted, which was not used for parameter estimation. In the simulations, the early breakthroughs of the Fe_3O_4/FeO zone are more distinct than in the experiment. One interpretation is that this reaction is not sufficiently slowed down with the blanket parameter f_R and deserves an own factor with a smaller value. Although the simulated output signals deviate significantly from the measured data, the time constants of this reaction wave are reflected reasonably well. Note that in the simulation with a flow rate of 2.3 and 2.4 NL/min, the breakthrough of the reaction zone starts directly after the start of the experiment. Obviously, the reaction rate is too low to attain equilibrium gas composition at this flow rate, even with a completely oxidised bed. This is in good qualitative agreement with the experimental results. At a low gas flow rate of 0.6 NL/min, equilibrium gas composition is reached for a few minutes after the start of the experiment.

The later breakthroughs of the FeO/Fe reaction zone are reflected very well by the model. This applies to both the residence time and the dispersity of these zones in all four experiments. Note that in this reaction, 75 % of the available oxygen is removed from the fixed bed, while the first reaction only removes 25 % of the oxygen. That means that the majority of the oxygen removal is reflected very well by the model. Note furthermore that only one set of fitting parameters (f_O, f_R) has been used to fit all experiments and reactions.

The absolute deviation between the measured and the simulated gas composition (for example in the experiment with 0.6 NL/min at $t = 40$ to 100 min) was not subject to minimisation. Nevertheless, this steady-state deviation is less than 1 vol-%. And this small discrepancy be attributed to errors in the calibration curves of the mass flow controllers and the sensor. In conclusion, the model is in very good agreement with the experimental data.

4.3.2. Complete Reduction-Oxidation Cycle

In the next step, the model was used with the kinetic and material parameters fitted in the previous section to simulate the complete redox cycle described in Sec. 4.1.3. Because of the fast degradation of the fixed bed used in this and the next experiment, a refitting of the model parameters was judged less important than the qualitative comparison of the experimental and simulated reactor behaviour.

Fig. 4.12 shows the simulated gas output concentrations of the experiment, which can be compared to Fig. 4.8 on p. 75. When comparing the reduction phase, please note the differently scaled ordinate. As in the experiment, two breakthroughs occur and the CO_2 concentration plateaus have the same value. The CO concentrations differ. Most likely because of the poor calibration of the sensor, which was only rated up to 30 vol−%. The oxidation in Fig. 4.8b resembles the one in the experiment in the number of breakthroughs, of which just one is observed, formed by two reactions fronts. The simulated reaction front residence times differ from the experimental because of the not fitted oxygen capacity.

To illustrate the internal states of the reactor, the degree of iron oxidation (oxygen content) is plotted over time and length in Fig. 4.13a. The oxygen content is scaled from 0 to 1 by the expression $x_{FeO} + (3/4) x_{FeO_{4/3}}$ and colour coded in the plot. Initially, the fixed bed is completely oxidised over the whole length (Fe_3O_4, red, value 0). During the first phase (from 0 to 330 min) the gas flows from left to right and reduced the fixed bed. At first FeO is formed (grey, value 0.75). This reaction front moves fast through the reactor and arrives at the right side/end of the reactor at $t \approx 25$ min, which is consistent with the first breakthrough in Fig. 4.12a. This reaction front is followed by a slower one: the reduction of FeO to Fe (blue, value 0), which arrives at $t \approx 260$ min. Thereafter, there is no change of the fixed bed's oxygen content until the start of the second phase, marked by the black line. During this time span, no reaction takes place, the output concentrations in Fig. 4.12a are the same as the feed concentrations. During the reduction phase, the gas flows from right to left, whereby reaction zones are moving into the same direction. As previously discussed, both reaction zones travel together, as the faster FeO/Fe_3O_4 zone cannot overtake the slower one as it depends on the Fe/FeO zone's reaction product FeO. For easier, albeit less exact visualisation, the fixed bed's oxygen content is henceforth plotted with an associated height in a 3d-plot given in Fig. 4.13b.
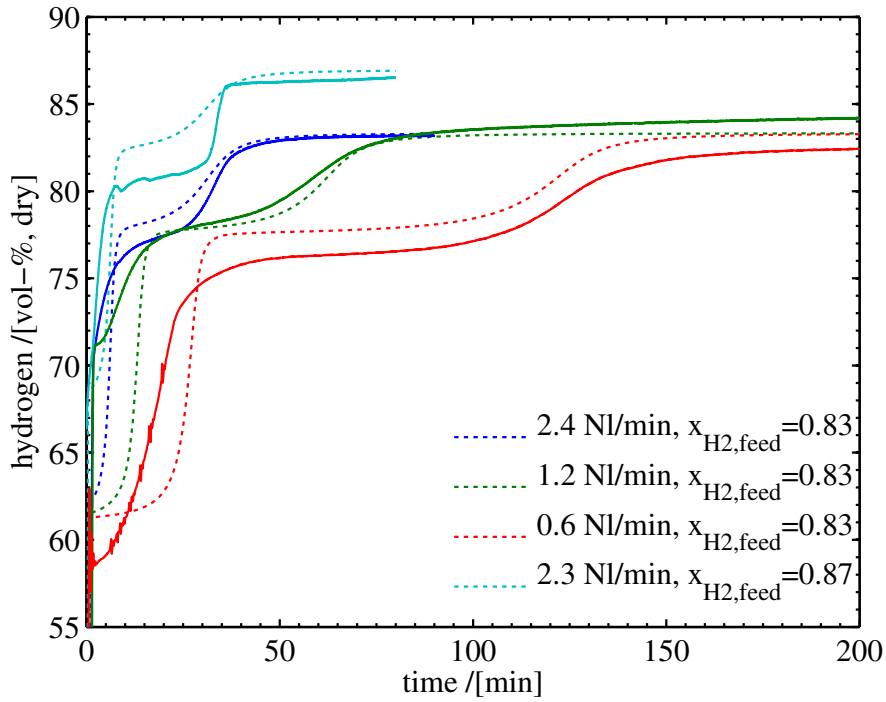
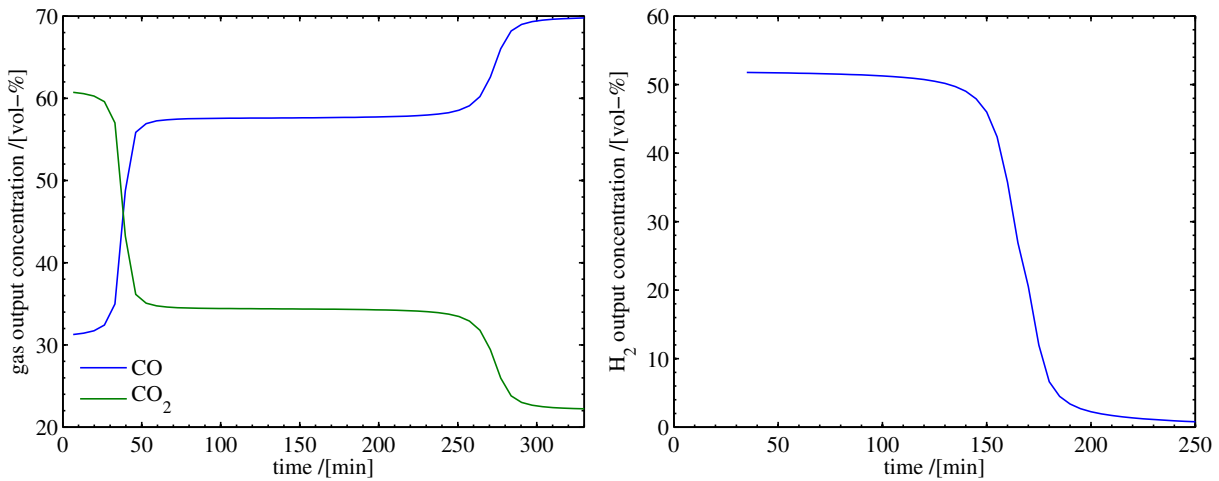Figure 4.11.: Comparison of simulated (dotted lines) and measured (solid lines) data for a series of reduction experiments. Fixed bed oxygen capacity and the reaction rate coefficients were fitted only to experiments with $x_{H_2}^{feed} = 0.83$. Compare to Fig. 4.6.

(a) Reduction Phase: 70 % CO and 22 % CO_2.

(b) Oxidation Phase: 76 % H_2O.

Figure 4.12.: Simulated gas output concentration profiles. Compare to Fig. 4.8.
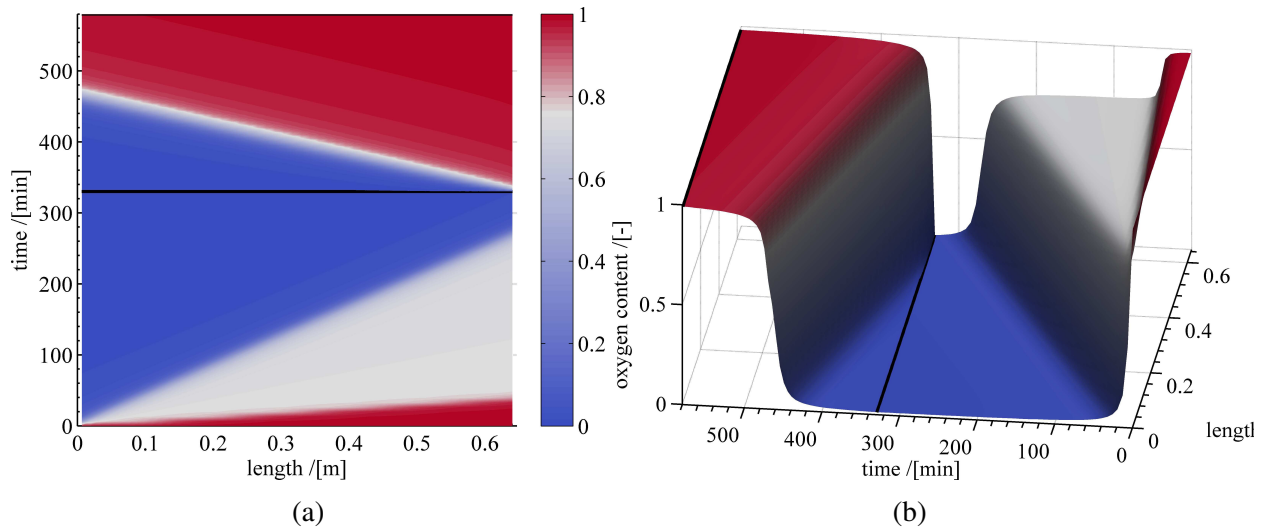
Figure 4.13.: Simulated oxygen content in the CWGSR fixed bed plotted versus time and reactor length. Oxygen content $= x_{\text{FeO}} + (3/4)\, x_{\text{FeO}_{4/3}}$, i.e. Fe is blue/0, FeO is grey/0.75, Fe_3O_4 is red/1. The black lines marks the switch in feed gas flow and direction.
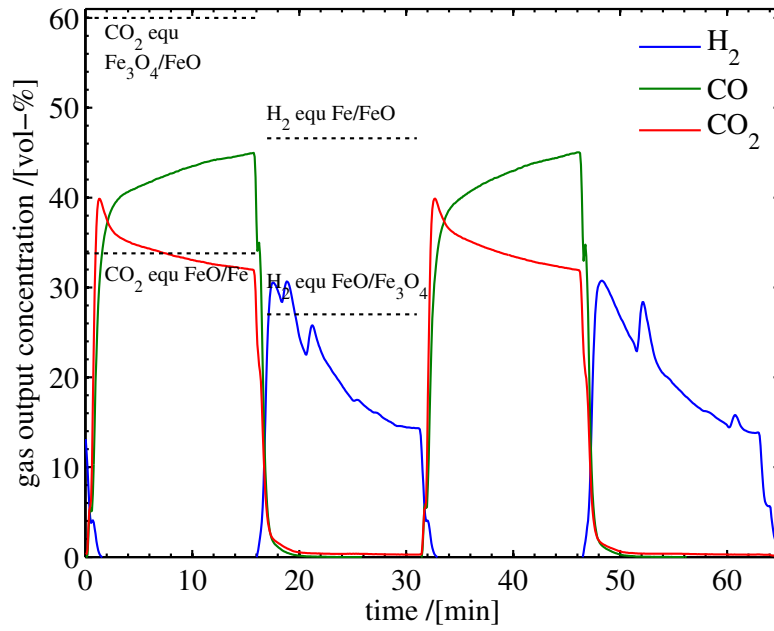
4.3.3. Continuous Cyclic Operation

A simulation of the continuous, cyclic reactor experiment of Sec. 4.1.4 was performed until the cyclic steady state was reached. The same operating parameters as in the experiment were used, while the kinetic and fixed bed parameters were again that of the fitting reported in Sec. 4.3.1.

Fig. 4.14 shows a comparison between experiments (a) and simulation (b). Immediately obvious are the much higher output concentrations in the simulation. Their levels indicate the $\text{FeO}/\text{Fe}_3\text{O}_4$ reaction zone breaking through the right side of the reactor, and the Fe/FeO zone breaking through the left side. This discussion, also performed in the experimental results, is illustrated and confirmed in Fig. 4.15a, a plot of the oxygen content in the reactor. The location of the reaction fronts in the experiment were approximately the same, but their extents were much larger, allowing for no length of constant oxygen content/pure FeO in between the reaction zones.

One obvious result from these simulations and prior analysis in [46] is the large amount of the fixed bed that is not used for any reaction. Given a fixed bed material, that is as reactive as the one simulated, a fixed bed about half the size would be able to achieve the same results. But this depends on the reaction rates – the fixed bed of the experiment was clearly not long

(a) Experimental results of Sec. 4.1.4
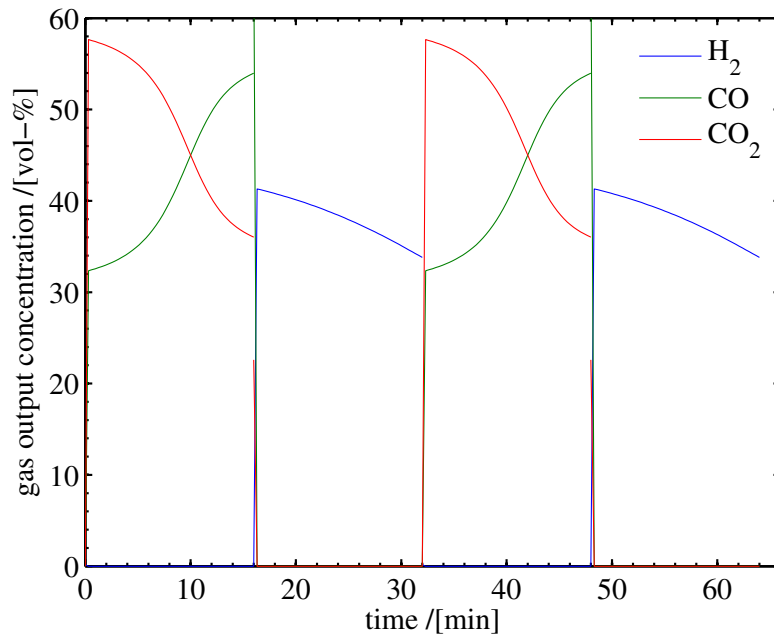
(b) Simulated results

Figure 4.14.: Comparison of experiment and simulation of a continuous cyclic operation in reverse flow operating mode. For experimental conditions see 4.1.4.

enough. The reactor part not immediately used for gas conversion can therefore be regarded as "spare length" for bed degradation.

Another idea previously discussed are the merits of increasingly shorter phase durations [45]. One advantage is the decreased stress put on the fixed bed by minimising the "amplitude" of the redox swings, the amount of oxygen extracted and reinserted into the fixed bed, and therefore a possibly slower degradation of the fixed bed material. This effect was not investigated in this work and awaits further experimental studies. Another advantage might be the ability to harness the high gas conversions at the start of a phase and immediately switch to the next phase to do the same there. When shortening the phase duration, the output concentrations settle in cyclic steady state around the temporal centre of the longer phase durations. This is illustrated in a short parameter study of phases of 16, 3 and 1 min duration in Figs. 4.14 and 4.15. In this case, the CO conversion increases only slightly from 36, 37 to 38 %. But this clearly depends on the shape of the profiles, which in turns depends on the kinetics, the location of the zones, the duration of the zones relative to each other.

4.3.4. Comparison to Equilibrium Model

The equilibrium model developed by Heidebrecht and Sundmacher [46] described the CWGSR solely through reaction front velocities averaged over one cycle. It is neither a spatially distributed, nor dynamic model and involves no reaction kinetics and is thus a simple model with a few algebraic equations, which lends itself for estimates of preferable operating conditions and limits of the CWGSR performance like fuel efficiency and H_2 output concentration and feed conditions.

One of the most important assumptions of the equilibrium model is the existence of a CWGSR operating regime, where its behaviour is dominated by moving reaction zones. This was already experimentally confirmed by the results reported in Sec. 4.1. The equilibrium model also assumes infinite reaction rates and reaction zones of negligible length. This contrasts with finite reaction rates, reaction zones of varying length, varying phase durations and gas volume hold up. How big the influence of these differences on the predicted performance of the reactor is, is subject of this section.

Dynamic simulation with the model proposed in Sec. 4.2 substitute experiments in this comparison. The test case is based on the feed concentrations given in the equilibrium models presentation [46], which are reprinted in Tab. 4.3. Fixed bed and kinetics data were used from Sec. 4.3.1 as in all previous comparisons. The reactor was operated at 750 °C. The
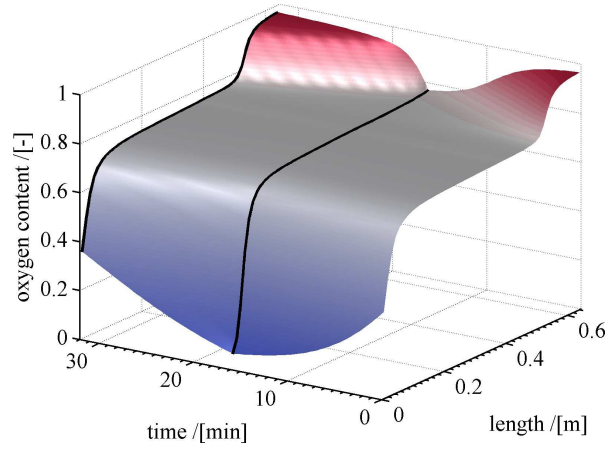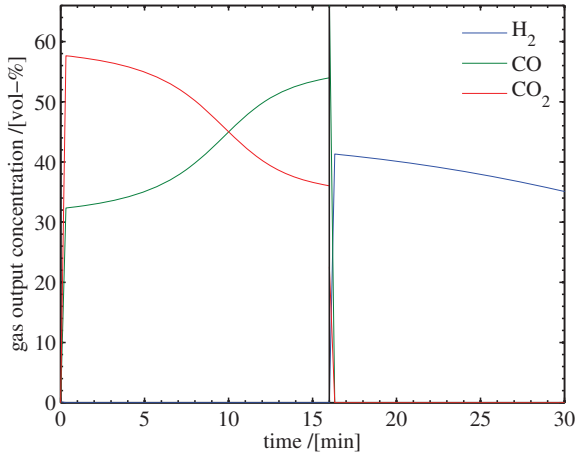
(a) Phase duration: 16 min each
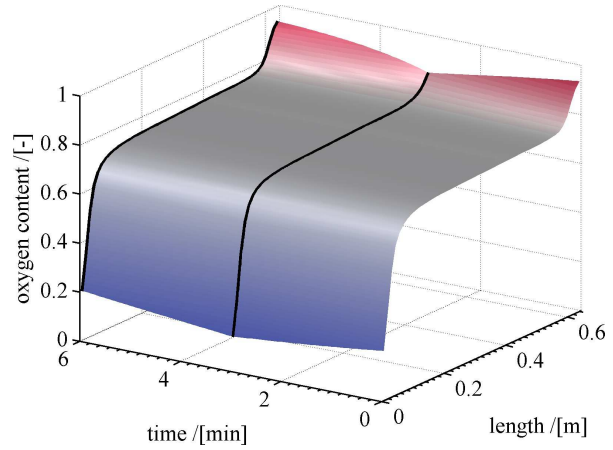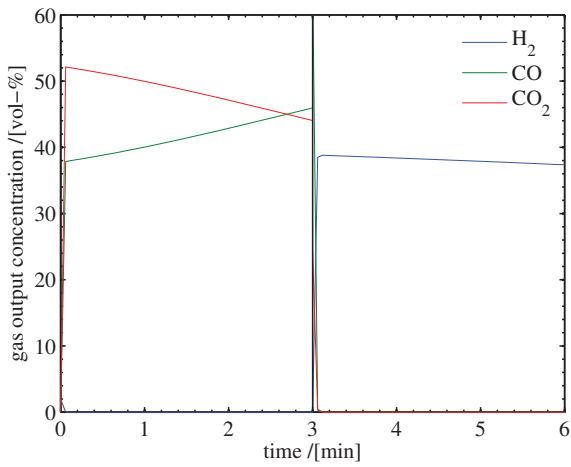
(b) Phase duration: 3 min each

(c) Phase duration: 1 min each

Figure 4.15.: The effect of shortening phase durations in the flow reversal mode.

Phase	x_{H_2}	x_{H_2O}	x_{CO}	x_{CO_2}	x_{N_2}	Y_H	Y_C	$y_{H_2O}^{feed}$	$y_{CO_2}^{feed}$	F /NL/min
I	0.65	0.11	0.17	0.04	0.03	0.76	0.21	0.14	0.19	1.35
II	0	1	0	0	0	1	0	1	0	1.35

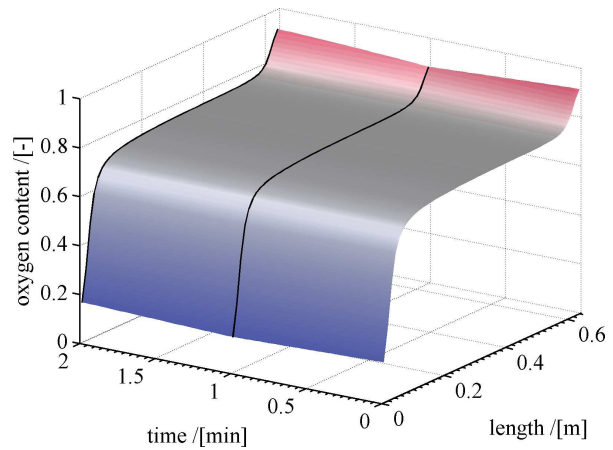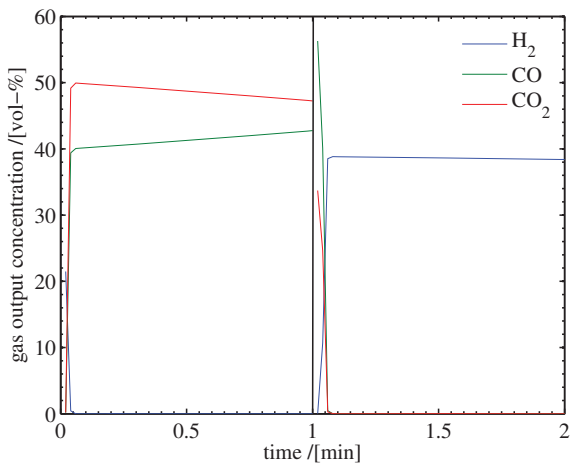Table 4.3.: Feed gas properties for the comparison between equilibrium and dynamic model. Phase I: Reduction; Phase II: Oxidation. From [46].

thermodynamic data from Tab. 2.2 were used. The latter is the reason for slight quantitative differences between the results of the equilibrium model presented here and results from the literature.

Two performance parameters, namely fuel efficiency and average H_2 output, are compared at varying relative phase durations. The fuel efficiency, η_{fuel}, is defined in Eq. 4.15 of [46] with the help of the average H_2 output concentration in the oxidation phase (phase II), $\bar{x}_{H_2}^{II,out}$. The relative duration of phase I (reduction), S^I, is defined in Eq. 4.16 and ranges from 0 to 1.

$$\eta_{fuel} = \frac{F^{II} \cdot \left(1 - S^I\right) \cdot \bar{x}_{H_2}^{II,out}}{F^I \cdot S^I \cdot \left(x_{H_2}^{I,feed} + x_{CO}^{I,feed}\right)} \tag{4.15}$$

$$S^I = \frac{t^I}{t^I + t^{II}} \tag{4.16}$$

The results of the equilibrium model are plotted as black lines in Fig. 4.16. The three operating regimes as described by the model and analysed in [46] are marked as well and are explained in the next paragraph. The results of the dynamic model are represented as red markers in the same figure. Each result at $S^I = 0.05, 0.20, 0.35, 0.50, 0.65, 0.80$ and 0.95 represents an approximate cyclic steady state (CSS) computed by the direct simulation of 100 to 300 cycles. The difference between the results of the two models are very small, yet plausible. The performance parameters of the dynamic model, subject to the identified reaction kinetics in addition to thermodynamic equilibria do not exceed the results from the equilibrium model. The minuteness of the difference is, however, surprising at first, given the differences between the outputs of a reaction front (shock) and a reaction zone. Other sources for the difference are non-symmetric reaction zones/kinetics, not having reached the true CSS yet and gas losses due to purging after phase switches. The effect of the latter is however, greatly underestimated in this simulation in comparison to experiments.
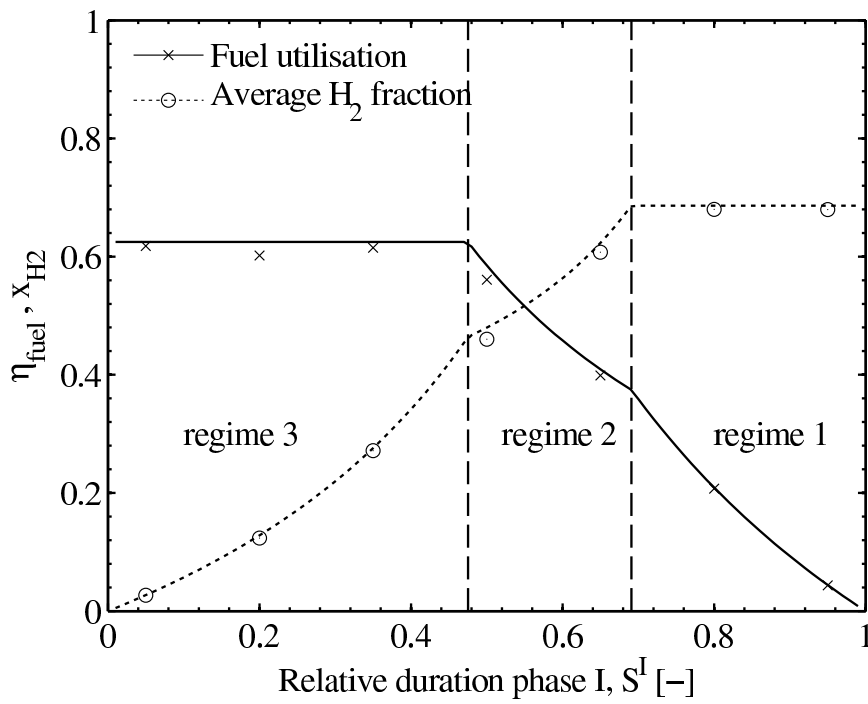
Figure 4.16.: Comparison of the equilibrium model in [46] (black lines) and approximate cyclic steady states computed by the dynamic model of this dissertation (data points).

Three exemplary CSS are shown in Fig. 4.17, which correspond to the three operating regimes predicted by the equilibrium model in Fig. 4.16. The operating regimes are characterised by the location of the reaction zones in the CWGSR, which directly influences the performance parameters as seen through the variation of S^I and explained in detail in [46]. The regimes emerge from the relative speeds of reaction zones, which depend on fixed bed capacity, feed concentrations, feed rate and relative phase duration. The latter two can be adjusted in a given application scenario to achieve a favourable operating point.

4.4. Summary

An experimental test stand was constructed, able to operate a tubular reactor of 1 m length in flow reversal mode at 750 °C. Reactor outlet gas concentrations of CO, CO_2 and H_2 were measured with an online gas analyser.

Three types of experiments were successfully conducted: (a) complete reductions of the fixed bed with H_2, (b) a complete CWGSR cycle with CO consumption and H_2 generation, and (c) short, continuous CWGSR cycles.

Breakthrough behaviour could be demonstrated for the CWGSR with two reaction zones discernable. The reaction zones move with different velocities through the reactor, depending on the amount of oxygen involved in the bed conversion and the rate educt/product transport in and out of the reactor, i. e. feed rate. The width of reaction zones depends on the reaction rates, or the Damköhler number, which decides whether the characteristic profile can evolve in the reactor.

The pelleting method produced physically stable results. The total theoretical amount of oxygen in the fixed bed was, at least initially, accessible by the gas phase. The rate of degradation (loss of reaction rate and oxygen availability), was however unpredictable, and is attributed to sintering of the pure iron oxide material.

The advantage of the flow reversal operating mode could not be confirmed experimentally. This can be attributed to heavy bed degradation, which in turn prevents the formation of distinct reaction zones in the reactor.

A dynamic model was formulated, that could be validated by the experimental data. It was an isothermal, 1-dimensional model based on mass balances for the gas and solid phase. Two numerical solution methods were implemented, of which the straightforward discretisation in space and implementation in Matlab turned out to be the more robust. The implementation

(a) $S^I = 0.2$, Regime 3: both reaction zones at the left side

(b) $S^I = 0.5$, Regime 2: reaction zones at the left and right side

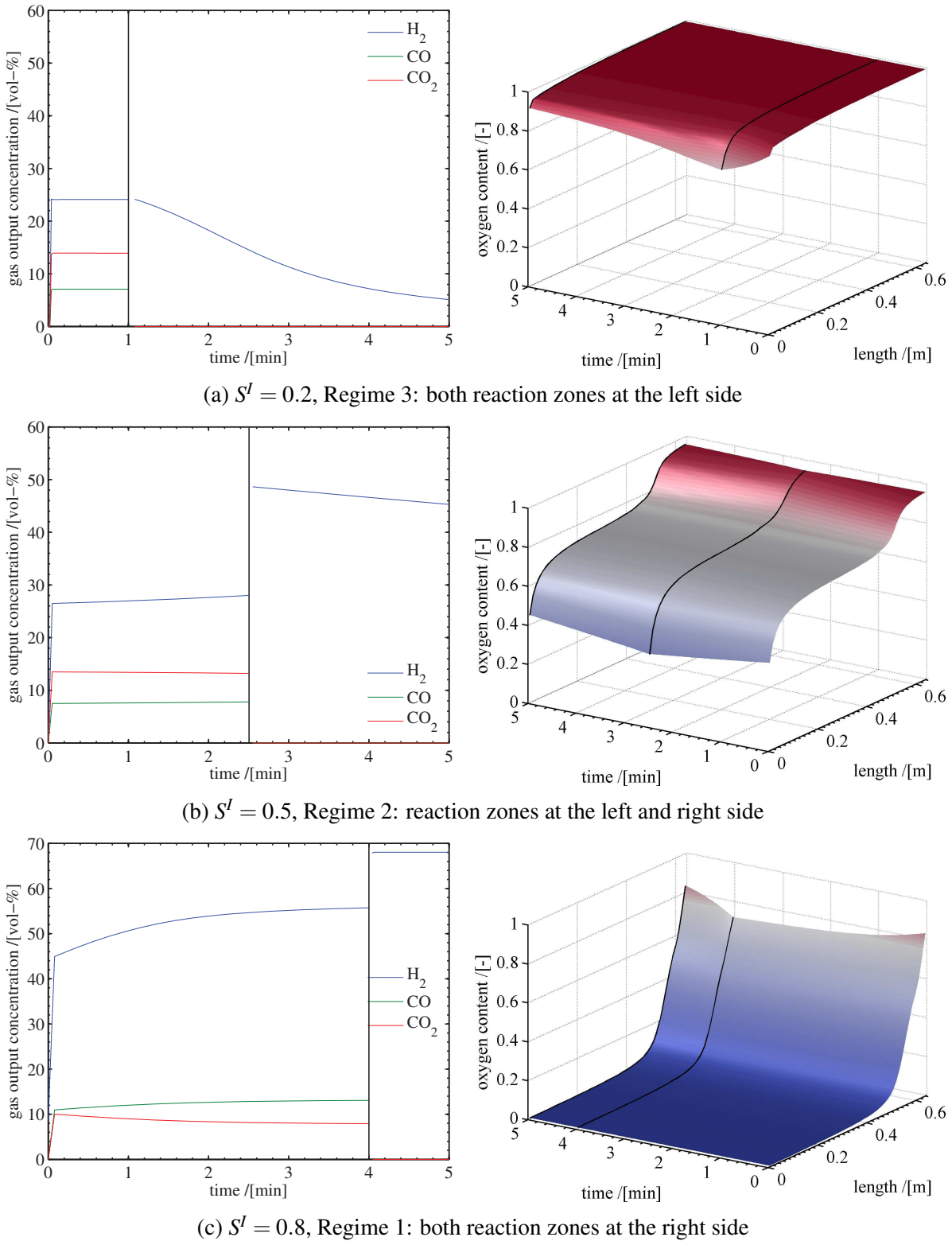(c) $S^I = 0.8$, Regime 1: both reaction zones at the right side

Figure 4.17.: The effect of shortening the cyclic steady states of the CWGSR at 750 °C and different relative phase durations fall into three different operating regimes.

in AMPL was too susceptible to the numerical problems induced by the special form of the kinetic expressions and the cyclic switching of the gas flow direction.

With the application of the a priori determined reaction rates of Chapter 2, the model could be fitted to experimental results with the help of two additional parameters: One for modifying the available oxygen content in the modelled fixed bed and one for all reaction rate constants. The fitted model could successfully reproduce the results of the second experiment, the complete CWGSR cycle. Comparing the simulation to the last experiments of continuous cycles was limited due to heavy bed degradation. However, the model was used to begin to explore the interconnections between design and operating parameters of the reactor.

The test stand is characterised and suitable for further experiments with the CWGSR. Preferably with a fixed bed of stabilised iron oxide material or of an intrinsically more stable material while exchanging oxygen, like perovskites [23,69]. A more stable steam supply could improve measurements significantly. Still missing is a direct experimental observation of the beneficial effects of the flow reversal mode.

The here proposed dynamic reactor model could be used for systematic parameter studies and rigorous optimisation on the CWGSR's design and operating parameters. In terms of optimisation problems, the model can be classified as a dynamic hybrid system with both controlled switching (e. g. flow reversal) and autonomous switching (e. g. kinetics). The implementation in AMPL is a promising start, but needs more work in solving numerical challenges. The straightforward addition of axial dispersion to the model should be done, when material degradation is under control.

The next step is the addition of temperature measurements in experiments as well as the addition of energy balances in the model. This will give more insight into the physical reactor and will open the CWGSR to investigations on recuperative heating and cooling of the gas phase as in a Matros reactor [64].

5. Conclusions

The first objective of this work was to conduct an experimental study on the reduction and oxidation reaction of Fe, FeO, Fe_3O_4 in CO/CO_2 and H_2/H_2O. The dependency on temperature, gas and solid composition was to be determined. The experimental findings were to be used to formulate kinetic expression for later use in a reactor model of the CWGSR.

Thermogravimetric analysis (TGA) was chosen as the experimental method. The weight of $400\,\mu m$ particles was continuously measured over the course of its reaction with a gas of constant composition and temperature. Gas composition and temperature were deliberately chosen to (a) ensure only one reaction step to take place, (b) encompass the full range of operating conditions likely to be encountered in a CWGSR (see Fig. 3.3) and (c) ensure a robust fitting of kinetic model parameters.

The classical TGA coupled with the ability to control the atmosphere in the sample chamber proved to be an excellent tool for measuring the rate of gas-solid phase reactions. The quality of the data w. r. t. to response time, noise and sample rate surpassed data gathered in later experiments by measuring the gas phase via nondisperse infrared sensors (NDIR) or thermal conductivity sensors (TCD) greatly.

The employed measurement technique hindered reaching the objective of a kinetic model fully backed by measurements, by not allowing the introduction of steam into the reaction, or in this case, weighing chamber. This forced all kinetic model parameters for reactions with H_2/H_2O to be extrapolated from the fully backed CO/CO_2 data and from reductions with pure H_2/N_2 gas. Although this reasoning and the obtained results are in line with the literature, it is the biggest shortcoming of the obtained results.

The parameter fitting procedure, which dictated the design of experiment parameter variation, was robust and achieved its goal. It can be argued that the approach was overly cautious and increased the number of experiments unnecessary as the range of experiment parameter could have been covered with less experiments.

The applicability of the identified kinetic model and its parameters to the CWGSR reactor model is arguably diminished by the fact, that different particle sizes were used in the fixed

5. Conclusions

bed reactor and above all, an iron oxide material without the stabilizing $Ce_{0.5}Zr_{0.5}O_2$. While these material choices, born from experimental difficulties, were not anticipated, the kinetic model with parameters from the TGA measurements did yield good results in the final reactor model with only slight modifications. This success raises the question for future work, how exact and faithful to reaction mechanisms a kinetic model for the CWGSR has to be, in order to model the reactor behaviour.

Future work could comprise of a more rigorous model discrimination, incorporate steam as an educt in the experimental setup and consider a more detailed oxidation model of iron, e. g. the oxidation range of wustite. Also, methods for the optimal design of experiments could be employed to greatly reduce the number of experiments and/or reduce the parameter confidence intervals. An interesting point of study is also the performance of the kinetic model in case multiple reaction occur simultaneously, which can also occur in the CWGSR.

The presented results directly benefits only the user of the same stabilized iron oxide material as used in this work. Users of similar iron oxide based materials or model based analysers can use the presented data as a basis, especially since a full model with all stepwise reduction and oxidations of iron / iron oxide is hard to find in the literature. The presented method is of interest to everybody with the goal to measure the rate of gas-solid reactions.

The second objective was the experimental analysis of the CWGSR. Reactor models have been published in the past and have been used to make predictions on the favourable operating mode. But these models were either of lower complexity and/or have not been backed up by experimental investigations.

A test stand was constructed, able to operate a tubular fixed bed reactor at $750\,°C$, supply $CO/CO_2/H_2/H_2O/N_2$ in a variety of mixtures, change flow direction during operation and measure the reactor outlet gas concentrations continuously. Experiments of increasing complexity were conducted to understand the reactor as well as the test plant.

Basic assumptions of previous models could be confirmed: Two distinct reaction zones do form in the fixed bed and their position/movement can be controlled by the CWGSR operating conditions. But the benefits of the in the literature predicted, favourable operating modes, based on the concept of flow reversal mode and short cycle durations, could not be validated experimentally. This failure could, however, not be attributed to the CWGSR itself, but to shortcomings in the experimental setup.

The construction, testing and operation of the test stand, as well as the preparation of the fixed bed was the most time and resource consuming part of this work. Iteration loops caused

by erroneous estimated flow ranges, test stand retrofits or fixed bed material problems caused the low number of data sets in this work. But time and effort needed for experimental studies are also the reason for the scarcity of published results and the lack of results similar to this work in the literature.

Future work can improve on many points of the experimental setup. Stability and reproducibility is of foremost concern, e. g. with regards to the fixed bed, the steam source or temperature measurements in the fixed bed. This will increase the ability to confirm model predicted, favourable operating modes of the reactor. With the background of this experimental study, a mostly, or even purely, experimentally driven analysis and optimisation of the CWGSR is deemed futile.

The third objective was to formulate a reactor model that can simulate the experiments of the CWGSR test stand and reproduce its results. Thus creating a validated model which can be used for further analysis of the CWGSR.

Based on mass balances of gas and solid phase and the reaction model from the first part of this work, a dynamic, one-dimensional, isothermal model was build and implemented in Matlab.

Experiments could be reproduced with good quality. The model is also consistent with previously published models and predicts the same favourable operating modes, while providing more information than the previously used shortcut models.

After exploring alternatives, the numerical solution of the model was done via a straightforward discretisation of the involved differential equations and a solution of the system, one time step after the other. While being robust, this method of solving the system is not suited for directly calculating cyclic steady states. In some cases, several hundred operating cycles have to be simulated to reach a cyclic steady state. Since the analysis and especially a numerical optimisation of the CWGSR will involve computing large numbers of cyclic steady states, better solutions methods have to be employed.

The next step for a model expansion would be the introduction of energy balances to reflect the influence of temperature effects on the reactor. Effects of heat accumulation in the reactor by recuperation have already been predicted. But experimental validation is lagging behind.

This work succeeded in proposing a new, validated model of the CWGSR. The model has a higher degree of detail than previously published models. It allows for better planning of future experiments and a more detailed, model based analysis of this reactor type.

102

A. Appendix: Estimation of Various Parameters

A.1. Weight Loss of Stabilised Iron Oxide

Effect of Iron Oxide Reduction on Sample Weight

A complete reduction of $FeO_{4/3}$ to Fe corresponds to the loss of $4/3$ mol O per mol of $FeO_{3/2}$. The stabilised material consists of 20 m% CeO_2ZrO_2. Therefore the anticipated weight loss of the oxygen storage material, based on its initial mass, i. e. its freshly synthesised state, is estimated by Eq. A.1. Similar calculations lead to the other expected weight losses given in Tab. A.1.

$$0.8 \frac{g_{FeO_{3/2}}}{g_{initial\,mass}} \cdot \frac{1}{90\,(g/mol)_{FeO_{3/2}}} \cdot \frac{4/3\,mol_{O\,loss}}{1\,mol_{Fe_2O_3}} \cdot 16 \frac{g_{O\,loss}}{mol_{O\,loss}} \approx 0.19 \frac{g_{O\,loss}}{g_{initial\,mass}} \qquad (A.1)$$

$[g_{O\,loss}/g_{initial\,mass}]$	Reduction to	Fe_3O_4	FeO	Fe
Reduction from	Fe_2O_3	0.024	0.071	0.213
	Fe_3O_4		0.047	0.190
	FeO			0.142

Table A.1.: Theoretical weight losses through reduction of stabilised iron oxide material in $g_{O\,loss}/g_{initial\,mass}$.

Effect of CeO$_2$ Reduction on Sample Weight

A possible reduction of 1 mol CeO_2 to $CeO_{3/2}$ corresponds to the loss of $1/2$ mol O per mol of the compound CeO_2ZrO_2. The stabilised material consists of 20 m% CeO_2ZrO_2. Therefore

the anticipated weight loss of the oxygen storage material, based on its inital mass, i. e. its freshly synthesised state, is:

$$0.2 \frac{g_{CeO_2ZrO_2}}{g_{initial\,mass}} \cdot \frac{1}{295\,(g/mol)_{CeO_2ZrO_2}} \cdot \frac{1/2\,mol_{O\,loss}}{1\,mol_{CeO_2ZrO_2}} \cdot 16 \frac{g_{O\,loss}}{mol_{O\,loss}} \approx 0.005 \frac{g_{O\,loss}}{g_{initial\,mass}} \quad \text{(A.2)}$$

A.2. Gas Residence Time in the Thermogravimetric Analysis (TGA) Chamber

The sample chamber is approximately $2\,cm$ in diameter and $8\,cm$ long. The flow rate is $120 \times 10^{-3}\,NL/min$. The residence time is therefore

$$\frac{\pi\,(2\,cm)^2 \cdot 8\,cm}{120 \times 10^{-3}\,NL/min \cdot \frac{1023\,K}{273\,K}} = \frac{100.5\,cm^3}{449.7\,cm^3\,min^{-1}} = 0.22\,min \quad \text{(A.3)}$$

A.3. Binary Diffusion Coefficients

Binary diffusion coefficients were estimated via a method and data given by Poling et al. [78] for 1000 K and 1 bar. Intermediate and final results are given in Tab. A.2.

		CO-N_2	CO_2-N_2	CO-CO_2	Eq. in [78]
Lennard-Jones length	σ_{AB}/Å	3.74	3.87	3.82	11-3.5
Diffusion collision integral	$\Sigma_{D_{AB}}$/-	0.72	0.76	0.78	11-3.6
Molecular weight	M_{AB}/g mol^{-1}	28	34	34	11-3.1
Diffusion coefficient	D_{AB}/10^{-4} m^2 s^{-1}	1.58	1.26	1.27	11-3.2

Table A.2.: Binary diffusion coefficient estimation [78].

An equation based on the "modified kinetic gas theory" proposed by Wesselingh and Krishna [101] support these values with $D_{CO_2-N_2} = 1.36 \times 10^{-4}\,m^2/s$.

The mean free path, calculated for the same conditions via Eq. A.4 is between 200 (CO_2) and 230 nm (CO).

$$\Lambda = \frac{k_B T}{\sqrt{2}\,\pi\,\sigma\,p} \qquad\qquad\qquad (A.4)$$

A.4. Changing Voidage Model (CVM): Molar Volume

The molar volumes of solid species assumed for the Changing Voidage Model (CVM) are listed in Tab. A.3.

	Molar mass / $\mathrm{g\,mol^{-1}}$	Density / $\mathrm{g\,cm^{-3}}$	Molar volume / $\mathrm{cm^3\,mol^{-1}}$
$FeO_{3/2}$	80	5.2	15.4
$FeO_{3/4}$	77	5.2	14.9
FeO	72	5.7	12.6
Fe	56	7.9	7.1

Table A.3.: Values used for the molar values of the CVM. Note: The synthesised material contains $80\,\mathrm{m\%}$ Fe_2O_3 and $20\,\mathrm{m\%}$ CeO_2ZrO_2.

Bibliography

[1] H. F. Abbas and W. M. A. W. Daud. Hydrogen production by methane decomposition: A review. *International Journal of Hydrogen Energy*, 35(3):1160–1190, 2010.

[2] L. S. Abbott. Process of and apparatus for producing hydrogen, 1920. US Patent 1,345,905.

[3] J. Adanez, L. F. de Diego, F. Garcia-Labiano, P. Gayan, A. Abad, and J. M. Palacios. Selection of oxygen carriers for chemical-looping combustion. *Energy & Fuels*, 18(2):371–377, 2004.

[4] M. Appl. Ammonia, 1. Introduction. In B. Elvers, editor, *Ullmann's Encyclopedia of Industrial Chemistry*, volume 3. John Wiley & Sons, Weinheim, 7th edition, 2011.

[5] Y. Bard. *Nonlinear Parameter Estimation*. Academic Press, New York, 1974.

[6] M. F. Bleeker, S. R. A. Kersten, and H. J. Veringa. Pure hydrogen from pyrolysis oil using the steam-iron process. *Catalysis Today*, 127(1-4):278–290, 2007.

[7] M. F. Bleeker, H. J. Veringa, and S. R. A. Kersten. Deactivation of iron oxide used in the steam-iron process to produce hydrogen. *Applied Catalysis A: General*, 357(1):5–17, 2009.

[8] L. v. Bogdandy and H.-J. Engell. *Die Reduktion der Eisenerze: Wissenschaftliche Grundlagen und technische Durchführung*. Springer, Berlin, 1967.

[9] J. Bolton. Solar photoproduction of hydrogen: A review. *Solar Energy*, 57(1):37–50, 1996.

[10] A. Bonalde, A. Henriquez, and M. Manrique. Kinetic analysis of the iron oxide reduction using hydrogen-carbon monoxide mixtures as reducing agent. *ISIJ International*, 45(9):1255–1260, 2005.

[11] L. Bromberg, D. Cohn, A. Rabinovich, and N. Alexeev. Plasma catalytic reforming of methane. *International Journal of Hydrogen Energy*, 24(12):1131–1137, 1999.

[12] R. E. Chao. Thermochemical water decomposion processes. *Industrial & Engineering Chemistry Product Research and Development*, 13(2):94–101, 1974.

[13] P. Chiesa, G. Lozza, A. Malandrino, M. Romano, and V. Piccolo. Three-reactors chemical looping process for hydrogen production. *International Journal of Hydrogen Energy*, 33(9):2233–2245, 2008.

[14] P. Cho, T. Mattisson, and A. Lyngfelt. Comparison of iron-, nickel-, copper- and manganese-based oxygen carriers for chemical-looping combustion. *Fuel*, 83(9):1215–1225, 2004.

[15] J. P. E. Cleeton, C. D. Bohn, C. R. Muller, J. S. Dennis, and S. A. Scott. Clean hydrogen production and electricity from coal via chemical looping: Identifying a suitable operating regime. *International Journal of Hydrogen Energy*, 34(1):1–12, 2009.

[16] R. Cortright, R. Davda, and J. Dumesic. Hydrogen from catalytic reforming of biomass-derived hydrocarbons in liquid water. *Nature*, 418(6901):964–967, 2002.

[17] R. Davda, J. Shabaker, G. Huber, R. Cortright, and J. Dumesic. A review of catalytic issues and process conditions for renewable hydrogen and alkanes by aqueous-phase reforming of oxygenated hydrocarbons over supported metal catalysts. *Applied Catalysis B – Environmental*, 56(1-2):171–186, 2005.

[18] L. F. de Diego, M. Ortiz, F. Garcia-Labiano, J. Adanez, A. Abad, and P. Gayan. Hydrogen production by chemical-looping reforming in a circulating fluidized bed reactor using Ni-based oxygen carriers. *Journal of Power Sources*, 192(1):27–34, 2009.

[19] A. S. Drud. CONOPT – A large-scale GRG code. *ORSA Journal on Computing*, 6(2):207–216216, 1994.

[20] P. Ekins. *Hydrogen Energy: Economic and Social Challenges*. Earthscan, 2010.

[21] B. A. Finlayson. *The Method of Weighted Residuals and Variational Principles: With Application in Fluid Mechanics, Heat and Mass Transfer*. Mathematics in Science and Engineering. Academic Press, New York, 1972.

[22] R. Fourer, D. M. Gay, and B. W. Kernighan. *AMPL: A Modeling Language for Mathematical Programming*. Thomson/Brooks/Cole, Pacific Grove, 2nd edition, 2003.

[23] R. V. Franca, A. Thursfield, and I. S. Metcalfe. $La_{0.6}Sr_{0.4}Co_{0.2}Fe_{0.8}O_{3-\delta}$ microtubular membranes for hydrogen production from water splitting. *Journal of Membrane Science*, 389:173–181, 2012.

[24] S. D. Fraser, M. Monsberger, and V. Hacker. A thermodynamic analysis of the reformer sponge iron cycle. *Journal of Power Sources*, 161(1):420–431, 2006.

[25] V. Galvita, T. Hempel, H. Lorenz, L. K. Rihko-Struckmann, and K. Sundmacher. Deactivation of modified iron oxide materials in the cyclic water gas shift process for CO-free hydrogen production. *Industrial & Engineering Chemistry Research*, 47(2):303–310, 2008.

[26] V. Galvita, L. K. Rihko-Struckmann, and K. Sundmacher. The CO adsorption on a Fe_2O_3-$Ce_{0.5}Zr_{0.5}O_2$ catalyst studied by TPD, isotope exchange and FTIR spectroscopy. *Journal of Molecular Catalysis A: Chemical*, 283(1-2):43–51, 2008.

[27] V. Galvita, T. Schröder, B. Munder, and K. Sundmacher. Production of hydrogen with low COx-content for PEM fuel cells by cyclic water gas shift reactor. *International Journal of Hydrogen Energy*, 33(4):1354–1360, 2008.

[28] V. Galvita and K. Sundmacher. Hydrogen production from methane by steam reforming in a periodically operated two-layer catalytic reactor. *Applied Catalysis A: General*, 289(2):121–127, 2005.

[29] V. Galvita and K. Sundmacher. Cyclic water gas shift reactor (CWGS) for carbon monoxide removal from hydrogen feed gas for PEM fuel cells. *Chemical Engineering Journal*, 134(1-3):168–174, 2007.

[30] V. Galvita and K. Sundmacher. Redox behavior and reduction mechanism of Fe_2O_3-$Ce_{0.5}Zr_{0.5}O_2$ as oxygen storage material. *Journal of Materials Science*, 42(22):9300–9307, 2007.

[31] C. Georgakis, C. W. Chang, and J. Szekely. Changing grain-size model for gas-solid reactions. *Chemical Engineering Science*, 34(8):1072–1075, 1979.

[32] B. Glöckler, G. Kolios, and G. Eigenberger. Analysis of a novel reverse-flow reactor concept for autothermal methane steam reforming. *Chemical Engineering Science*, 58(3-6):593–601, 2003.

[33] K. S. Go, S. R. Son, S. D. Kim, K. S. Kang, and C. S. Park. Hydrogen production from two-step steam methane reforming in a fluidized bed reactor. *International Journal of Hydrogen Energy*, 34(3):1301–1309, 2009.

[34] A. Gorbach, G. Eigenberger, and G. Kolios. General approach for the reduction of detailed models for fast cycling processes. *Industrial & Engineering Chemistry Research*, 44(8):2369–2381, 2005.

[35] C. Grimes, O. Varghese, and S. Ranjan. *Light, Water, Hydrogen: The Solar Generation of Hydrogen by Water Photoelectrolysis*. Fuel Cells and Hydrogen Energy. Springer, London, 2007.

[36] H. Gunardson. *Industrial Gases in Petrochemical Processing*. Taylor & Francis, 1997.

[37] P. Gupta, L. G. Velazquez-Vargas, and L. S. Fan. Syngas redox (SGR) process to produce hydrogen from coal derived syngas. *Energy & Fuels*, 21(5):2900–2908, 2007.

[38] R. Gupta. *Hydrogen Fuel: Production, Transport, and Storage*. Taylor & Francis, 2008.

[39] V. Hacker. A novel process for stationary hydrogen production: the reformer sponge iron cycle (RESC). *Journal of Power Sources*, 118(1-2):311–314, 2003.

[40] V. Hacker, G. Faleschini, H. Fuchs, R. Fankhauser, G. Simader, M. Ghaemi, B. Spreitz, and K. Friedrich. Usage of biomass gas for fuel cells by the SIR process. *Journal of Power Sources*, 71(1-2):226–230, 1998.

[41] V. Hacker, R. Fankhauser, G. Faleschini, H. Fuchs, K. Friedrich, M. Muhr, and K. Kordesch. Hydrogen production by steam-iron process. *Journal of Power Sources*, 86(1-2):531–535, 2000.

[42] V. Hacker, R. Vallant, and M. Thaler. Thermogravimetric investigations of modified iron ore pellets for hydrogen storage and purification: First charge and discharge cycle. *Industrial & Engineering Chemistry Research*, 46(26):8993–8999, 2007.

[43] B. Hartono, P. Heidebrecht, and K. Sundmacher. A mass integration concept for high temperature fuel cell plants. *International Journal of Hydrogen Energy*, 36(12):7240–7250, 2011.

[44] P. Heidebrecht, B. Hartono, C. Hertel, and K. Sundmacher. Biomass-based fuel cell power plants: Evaluation of novel reactors and process designs. *Industrial & Engineering Chemistry Research*, 49(21):10859–10875, 2010.

[45] P. Heidebrecht, C. Hertel, and K. Sundmacher. Conceptual analysis of a cyclic water gas shift reactor. *International Journal of Chemical Reactor Engineering*, 6:18, 2008.

[46] P. Heidebrecht and K. Sundmacher. Thermodynamic analysis of a cyclic water gas-shift reactor (CWGSR) for hydrogen production. *Chemical Engineering Science*, 64(23):5057–5065, 2009.

[47] C. Hertel. *Modellbasierte Analyse eines zyklischen Wassergas-Shift-Reaktors*. Otto-von-Guericke University, Faculty for Process and Systems Engineering, Chair for Process Systems Engineering, 2007. Diplomarbeit.

[48] C. Hertel, P. Heidebrecht, and K. Sundmacher. Experimental quantification and modelling of reaction zones in a cyclic watergas shift reactor. *International Journal of Hydrogen Energy*, 37(3):2195–2203, 2012.

[49] C. Higman and M. van der Burgt. *Gasification*. Elsevier Science, 2011.

[50] J. D. Holladay, J. Hu, D. L. King, and Y. Wang. An overview of hydrogen production technologies. *Catalysis Today*, 139(4):244–260, 2009.

[51] P. Häussinger, R. Lohmüller, and A. M. Watson. Hydrogen 6. Uses. In B. Elvers, editor, *Ullmann's Encyclopedia of Industrial Chemistry*, volume 18. John Wiley & Sons, Weinheim, 7th edition, 2011.

[52] A. A. Ismail and D. W. Bahnemann. Photochemical splitting of water for hydrogen production by photocatalysis: A review. *Solar Energy Materials and Solar Cells*, 128:85–101, 2014.

[53] H. Kindermann, M. Kornberger, J. Hierzer, J. O. Besenhard, and V. Hacker. First investigations of structural changes of the contact mass in the RESC process for hydrogen production. *Journal of Power Sources*, 145(2):697–701, 2005.

[54] A. Kudo. Recent progress in the development of visible light-driven powdered photocatalysts for water splitting. *Internationals Journal of Hydrogen Energy*, 32(14):2673–2678, 2007.

[55] S. Lee, J. Speight, and S. Loyalka. *Handbook of Alternative Fuel Technologies*. Taylor & Francis, 2nd edition, 2014.

[56] O. Levenspiel. *The Chemical Reactor Omnibook*. OSU Corvallis Book Stores, Corvallis, 1996.

[57] O. Levenspiel. *Chemical Reaction Engineering*. Wiley, New York, 3rd edition, 1999.

[58] P. J. Linstrom and P. J. Mallard. *NIST Chemistry WebBook*. National Institute of Standards and Technology, 2008. NIST Standard Reference Database Number 69.

[59] F. Logist, J. Lauwers, B. Trigaux, and J. F. V. Impe. Model based optimisation of a cyclic reactor for the production of hydrogen. In Pistikopoulos, Georgiadis, and Kokossis, editors, *21st European Symposium on Computer Aided Process Engineering*, volume 29 of *Computer Aided Chemical Engineering*, pages 457 – 461. Elsevier, 2011.

[60] E. Lorente, J. A. Peña, and J. Herguido. Kinetic study of the redox process for separating and storing hydrogen: Oxidation stage and ageing of solid. *International Journal of Hydrogen Energy*, 33(2):615–626, 2008.

[61] E. Lorente, J. A. Peña, and J. Herguido. Separation and storage of hydrogen by steam-iron process: Effect of added metals upon hydrogen release and solid stability. *Journal of Power Sources*, 192(1):224–229, 2009.

[62] R. Luque and J. Speight. *Gasification for Synthetic Fuel Production: Fundamentals, Processes and Applications*. Elsevier Science, 2014.

[63] J. Maier. *Physical chemistry of ionic materials: Ions and electrons in solids*. Wiley, Hoboken, 2004.

[64] Y. S. Matros, G. A. Bunimovich, and A. S. Noskov. The decontamination of gases by unsteady-state catalytic method. Theory and practice. *Catalysis Today*, 17:261–274, 1993.

[65] A. Messerschmitt. Process of producing hydrogen, 1910. US Patent 971,206.

[66] A. Messerschmitt. Verfahren zur Erzeugung von Wasserstoff durch abwechselnde Oxydation und Reduktion von Eisen in von aussen beheizten, in den Heizräumen angeordneten Zersetzern, 1911. German Patent 266,863.

[67] I. J. Moon, C. H. Rhee, and D. J. Min. Reduction of hematite compacts by H_2-CO gas mixtures. *Steel Research*, 69(8):302–306, 1998.

[68] N. Muradov. Hydrogen via methane decomposition: An application for decarbonization of fossil fuels. *International Journal of Hydrogen Energy*, 26(11):1165–1175, 2001.

[69] A. Murugan, A. Thursfield, and I. S. Metcalfe. A chemical looping process for hydrogen production using iron-containing perovskites. *Energy & Environmental Science*, 4(11):4639–4649, 2011.

[70] G. Naterer, I. Dincer, and C. Zamfirescu. *Hydrogen Production from Nuclear Energy*. Springer, London, 2013.

[71] R. M. Navarro, M. A. Peña, and J. L. G. Fierro. Hydrogen production reactions from carbon feedstocks: Fossils fuels and biomass. *Chemical Reviews*, 107(10), 2007.

[72] U. Onken, A. Behr, F. Fetting, J. Falbe, and W. Keim. *Chemische Prozeßkunde: Lehrbuch der Technischen Chemie*. Wiley, 2009.

[73] C. E. Parsons. Process of making substantially pure hydrogen, 1928. US Patent 1,658,939.

[74] A. A. Peterson, F. Vogel, R. P. Lachance, M. Froeling, M. J. Antal, Jr., and J. W. Tester. Thermochemical biofuel production in hydrothermal media: A review of sub- and supercritical water technologies. *Energy & Environmental Science*, 1(1):32–65, 2008.

[75] G. Petitpas, J.-D. Rollier, A. Darmon, J. Gonzalez-Aguilar, R. Metkemeijer, and L. Fulcheri. A comparative study of non-thermal plasma assisted reforming technologies. *International Journal of Hydrogen Energy*, 32(14):2848–2867, 2007.

[76] A. Pineau, N. Kanari, and I. Gaballah. Kinetics of reduction of iron oxides by H_2 – Part I: Low temperature reduction of hematite. *Thermochimica Acta*, 447(1):89–100, 2006.

[77] A. Pineau, N. Kanari, and I. Gaballah. Kinetics of reduction of iron oxides by H_2 – Part II: Low temperature reduction of magnetite. *Thermochimica Acta*, 456(2):75–88, 2007.

[78] B. E. Poling, J. M. Prausnitz, and J. P. O'Connell. *The Properties of Gases and Liquids*. McGraw-Hill, New York, 5th edition, 2001.

[79] P. V. Ranade and D. P. Harrison. Grain model applied to porous solids with varying structural-properties. *Chemical Engineering Science*, 34(3):427–432, 1979.

[80] D. Rand, R. Dell, and R. S. of Chemistry (Great Britain). *Hydrogen Energy: Challenges and Prospects*. RSC energy series. Royal Society of Chemistry, 2008.

[81] J. B. Rawlings and J. G. Ekerdt. *Chemical Reactor Analysis and Design Fundamentals*. Nob Hill Publishing, Madison, 1st edition, 2002.

[82] C. Sattler. Thermochemical Cycles. In D. Stolten, editor, *Hydrogen and Fuel Cells*, chapter 9, pages 189–206. Wiley-VCH, Weinheim, 2010.

[83] L. O. Schunk and A. Steinfeld. Kinetics of the thermal dissociation of ZnO exposed to concentrated solar irradiation using a solar-driven thermogravimeter in the 1800-2100 K range. *AIChE Journal*, 55(6):1497–1504, 2009.

[84] H. Seiler and G. Emig. Reduction-oxidation cycles in a fixed-bed reactor with periodic flow reversal. *Chemical Engineering & Technology*, 22(6):479–484, 1999.

[85] A. Sim, N. W. Cant, and D. L. Trimm. Ceria-zirconia stabilised tungsten oxides for the production of hydrogen by the methane-water redox cycle. *International Journal of Hydrogen Energy*, 35(17):8953–8961, 2010.

[86] R. Sime, J. Kuehni, L. D'Souza, E. Elizondo, and S. Biollaz. The redox process for producing hydrogen from woody biomass. *International Journal of Hydrogen Energy*, 28(5):491–498, 2003.

[87] C. Simon. *Alternative Energy: Political, Economic, and Social Feasibility*. Rowman & Littlefield Publishers, 2007.

[88] K. Skutil and M. Taniewski. Some technological aspects of methane aromatization (direct and via oxidative coupling). *Fuel Processing Tecehnology*, 87(6):511–521, 2006.

[89] T. Smolinka, S. Rau, and C. Hebling. Polymer Electrolyte Membrane (PEM) Water Electrolysis. In D. Stolten, editor, *Hydrogen and Fuel Cells*, chapter 13, pages 271–288. Wiley-VCH, Weinheim, 2010.

[90] J. Speight. *The Chemistry and Technology of Petroleum, Fourth Edition*. Taylor & Francis, 4th edition, 2006.

[91] D. Stolten and D. Krieg. Alkaline Electrolysis – Introduction and Overview. In D. Stolten, editor, *Hydrogen and Fuel Cells*, chapter 12, pages 243–267. Wiley-VCH, Weinheim, 2010.

[92] K. Svoboda, G. Slowinski, J. Rogut, and D. Baxter. Thermodynamic possibilities and constraints for pure hydrogen production by iron based chemical looping process at lower temperatures. *Energy Conversion and Management*, 48(12):3063–3073, 2007.

[93] J. Szekely and J. W. Evans. A structural model for gas-solid reactions with a moving boundary. *Chemical Engineering Science*, 25(6):1091–1107, 1970.

[94] J. Szekely and J. W. Evans. Studies in gas-solid reactions: Part I. A structural model for the reaction of porous oxides with a reducing gas. *Metallurgical Transactions*, 2(6):1691–1698, 1971.

[95] J. Szekely, J. W. Evans, and H. Y. Sohn. *Gas-Solid Reactions*. Academic Press, New York, 1976.

[96] Y. Takenaka, Y. Kimura, K. Narita, and D. Kaneko. Mathematical model of direct reduction shaft furnace and its application to actual operations of a model plant. *Computers & Chemical Engineering*, 10(1):67–75, 1986.

[97] M. Thaler and V. Hacker. Storage and separation of hydrogen with the metal steam process. *International Journal of Hydrogen Energy*, 37(3):2800 – 2806, 2012.

[98] M. Thaler, V. Hacker, A. Anilkumar, J. Albering, J. O. Besenhard, H. Schrottner, and M. Schmied. Investigations of cycle behaviour of the contact mass in the RESC process for hydrogen production. *International Journal of Hydrogen Energy*, 31(14):2025–2031, 2006.

[99] Q. T. Tsay, W. H. Ray, and J. Szekely. The modeling of hematite reduction with hydrogen plus carbon monoxide mixtures. *AIChE Journal*, 22(6):1064–1079, 1976.

[100] M. S. Valipour, M. Y. M. Hashemi, and Y. Saboohi. Mathematical modeling of the reaction in an iron ore pellet using a mixture of hydrogen, water vapor, carbon monoxide and carbon dioxide: An isothermal study. *Advanced Powder Technology*, 17(3):277–295, 2006.

[101] J. A. Wesselingh and R. Krishna. *Mass Transfer in Multicomponent Mixtures*. Delft University Press, Delft, 1st edition, 2000.

[102] V. Wiedmeyer. *Implementierung des Modells eines zyklischen Wassergas-Shift-Reaktors in der Modellierungsumgebung AMPL*. Otto-von-Guericke University, Faculty for Electrical Engineering and Information Technology, 2011. Bachelor Thesis.

[103] K. Winnacker and L. Küchler. *Chemische Technik: Prozesse und Produkte*, volume 6a: Metalle, page 214pp. WILEY-VCH, 5th edition, 2006.

[104] B. W. Wojciechowski and N. M. Rice. *Experimental Methods in Kinetic Studies*. Elsevier, Amsterdam, rev. edition, 2003.

[105] J. Wolf and J. Yan. Parametric study of chemical looping combustion for tri-generation of hydrogen, heat, and electrical power with CO_2 capture. *International Journal of Energy Research*, 29(8):739–753, 2005.

[106] Y. Xu and L. Lin. Recent advances in methane dehydro-aromatization over transition metal ion-modified zeolite catalysts under non-oxidative conditions. *Applied Catalysis A– General*, 188(1-2):53–67, 1999.

[107] J. B. Yang, N. S. Cai, and Z. S. Li. Hydrogen production from the steam-iron process with direct reduction of iron oxide by chemical looping combustion of coal char. *Energy & Fuels*, 22(4):2570–2579, 2008.

[108] A. York, T. Xiao, and M. Green. Brief overview of the partial oxidation of methane to synthesis gas. *Topics in Catalysis*, 22(3-4):345–358, 2003.

[109] Q. Zafar, T. Mattisson, and B. Gevert. Integrated hydrogen and power production with CO_2 capture using chemical-looping reforming-redox reactivity of particles of CuO, Mn_2O_3, NiO, and Fe_2O_3 using SiO_2 as a support. *Industrial & Engineering Chemistry Research*, 44(10):3485–3496, 2005.

[110] M. Zahid, J. Schefold, and A. Brisse. High Temperature Water Electrolysis Using Planar Solid Oxide Fuel Cell Technology: A Review. In D. Stolten, editor, *Hydrogen and Fuel Cells*, chapter 11, pages 227–241. Wiley-VCH, Weinheim, 2010.

[111] A. Züttel, A. Borgschulte, and L. Schlapbach. *Hydrogen as a Future Energy Carrier*. Wiley, 2011.

Declaration

This dissertation contains material that has previously been published elsewhere:

1. C. Hertel, P. Heidebrecht, and K. Sundmacher.
   Experimental Quantification and Modelling of Reaction Zones in a Cyclic Watergas Shift Reactor.
   International Journal of Hydrogen Energy, 37(3):2195–2203, 2012.

The following publications are co-authored by the author of this thesis. They are referenced, but no material is presented as part of this dissertation.

2. P. Heidebrecht, C. Hertel, and K. Sundmacher.
   Conceptual Analysis of a Cyclic Water Gas Shift Reactor.
   International Journal of Chemical Reactor Engineering, 6:18, 2008.

3. P. Heidebrecht, B. Hartono, C. Hertel, and K. Sundmacher.
   Biomass-based Fuel Cell Power Plants: Evaluation of Novel Reactors and Process Designs.
   Industrial & Engineering Chemistry Research, 49(21):10859–10875, 2010.

Statement of authorship

1. The author developed the methodology, designed and set up the experiments, carried out measurements, evaluated the experimental results. The author set up the mathematical model, carried out the simulations and evaluated the results. The author wrote the manuscript.

2. The author developed the methodology together with Peter Heidebrecht, carried out the simulations and evaluated the results.

3. The author set up some of the models and simulation code. The author implemented the pinch analysis.

Student theses

The following student theses were prepared at the Chair for Process Systems Engineering, Otto-von-Guericke University Magdeburg, under the supervision of the author of the present doctoral thesis:

1. Elina Gedicke.
   Charakterisierung eines ZWGSR-Versuchsstandes.
   Studienarbeit, 2010.

2. Viktoria Wiedmeyer.
   Implementierung des Modells eines Zyklischen Wassergas-Shift-Reaktors in der Modellierungsumgebung AMPL.
   Bachelor Thesis, 2011.